Een driedimensionale differentiële oppervlakte-admittantie-operator
voor de breedbandmodellering van verlieshebbende geleiders

A 3-D Differential Surface Admittance Operator
for the Broadband Modeling of Lossy Conductors

Martijn Huynen

Promotoren: prof. dr. ir. D. Vande Ginste, em. prof. dr. ir. D. De Zutter
Proefschrift ingediend tot het behalen van de graad van
Doctor in de ingenieurswetenschappen: elektrotechniek

UNIVERSITEIT
GENT

Vakgroep Informatietechnologie
Voorzitter: prof. dr. ir. B. Dhoedt
Faculteit Ingenieurswetenschappen en Architectuur
Academiejaar 2018 - 2019

ISBN 978-94-6355-220-2
NUR 959, 928
Wettelijk depot: D/2019/10.500/28

A 3-D Differential Surface Admittance Operator for the Broadband Modeling of Lossy Conductors

Martijn Huynen

Dissertation submitted to obtain the academic degree of
Doctor of Eletrical Engineering

Publicly defended at Ghent University on April 18, 2019

Supervisor:

prof. dr. ir. D. Vande Ginste
Electromagnetics group
Department of Information Technology
Faculty of Engineering and Architecture
Ghent University
Technologiepark-Zwijnaarde 126
B-9052 Ghent, Belgium
http://emweb.intec.ugent.be

Supervisor:

em. prof. dr. ir. D. De Zutter
Electromagnetics group
Department of Information Technology
Faculty of Engineering and Architecture
Ghent University
Technologiepark-Zwijnaarde 126
B-9052 Ghent, Belgium
http://emweb.intec.ugent.be

Members of the examining board:

prof. dr. ir. F. De Turck (chairman)	Ghent University, Belgium
prof. dr. ir. H. Rogier (secretary)	Ghent University, Belgium
prof. dr. ir. D. Vande Ginste (supervisor)	Ghent University, Belgium
em. prof. dr. ir. D. De Zutter (supervisor)	Ghent University, Belgium
prof. dr. ir. V. Okhmatovski	University of Manitoba, Canada
dr. ir. E. Beyne	imec, Belgium
prof. dr. ir. T. Dhaene	Ghent University, Belgium

FACULTY OF ENGINEERING AND ARCHITECTURE

GHENT UNIVERSITY

Dankwoord

Als u deze woorden leest, komen er zo direct enkele mogelijke redenen bij mij naar boven waarom: u wilt graag (om een of andere reden) meer te weten komen over het beest genaamd de oppervlakte-admittantie-operator, u heeft moeite met de slaap te vatten en heeft nood aan wat droge kost of — en dit is ongetwijfeld de grootste groep lezers — u bent nieuwsgierig of u vermeld wordt in dit dankwoord. Aan de eerste groep richt ik deze korte, doch krachtige boodschap: "Veel succes en *lasciate ogni speranza, voi ch'entrate*". De tweede groep raad ik Sectie 5.4 en Hoofdstuk 6 aan; veel formules, weinig prentjes, kortom perfect om bij in slaap te dommelen. Voor mensen uit de laatste groep hoop ik de hooggespannen verwachtingen te kunnen inlossen. Het is namelijk zo dat vooraan op dit boekje dan wel mijn naam prijkt, maar de inhoud van dit werk zo onmogelijk tot stand zijn kunnen komen zonder de input en steun van een hele hoop mensen. Groot of klein, direct of indirect, actief of passief, ik apprecieer ieders hulp en inbreng van harte. Daarom verzoek ik u dan ook vriendelijk om geen belang te hechten aan enige volgorde van vernoeming of lengte van dank in de volgende tekst. Ik doe ook mijn uiterste best om hier niemand te vergeten vermelden maar mocht dit toch voorvallen, mea maxima culpa.

Vooreerst wil ik graag een enorm welgemeende dank u wel richten aan mijn beide promotoren, Dries en Daniël. Hun inbreng, visie, kennis en feedback hebben er niet enkel voor gezorgd dat ik aan dit werk ben kunnen beginnen maar des te meer dat hier voor u effectief een afgewerkt proefschrift ligt en dat ik dit dankwoord kan schrijven. Hun ideeën en steun hebben me door de bij momenten diepe dalen van dit doctoraat geleid, elk op hun eigen manier maar steeds samen als een goed geoliede machine. Ik heb ook enorm genoten van onze (al dan niet trans-Atlantische) gesprekken over elektromagnetische en alle andere onderwerpen. Ook wil ik het derde lid van het triumviraat van onze groep, d.i. Hendrik, bedanken voor de fijne discussies en de uurtjes gesleten in de opleidingscommissie.

Een computationeel onderzoek heeft ook zo zijn nadelen. Achter ons scherm gekluisterd, code schrijvend, is de link met de praktische realiteit soms ver te zoeken. Daarom ben ik imec zeer dankbaar en in het bijzonder Eric Beynes groep om naar het einde van dit onderzoek toe die connectie te voorzien. Bedankt dus ook aan Geert Van der Plas en Xiao Sun om een interessante case voor te stellen en samen met ons te onderzoeken. Dit lijkt me ook het perfect moment om een aantal mensen te vermelden die op een meer indirecte manier hun steentje hebben bijgedragen. Tijdens onze tijd in het Technicum leidde Isabelle ons allemaal moeiteloos door de woelige wateren die zo kenmerkend zijn voor de administratie aan de UGent, waarvoor mijn welgemeende complimenten. Na onze verhuis naar de iGenttoren, werden we in deze bijgestaan door het team van Martine, Davinia

en Bernadette. Een dikke merci ook aan Sabrina. Jouw dagelijks gevecht tegen de bierkaai is enorm bewonderenswaardig, zeker omdat je telkens weer het beste van jezelf geeft.

Collega's komen en gaan maar ook al is de samenstelling van deze groep enorm veranderd door de jaren heen, de behulpzaamheid en de toffe sfeer zijn moeiteloos doorgegeven van generatie op generatie. Bij de minste vraag/twijfel/brainfart staat er wel altijd iemand klaar om een handje toe te steken of samen een probleem op te lossen. Ook bij de begeleiding van studenten tijdens thesissen en projecten is er een enorme drive om dit samen tot een goed einde te brengen ondanks het soms angstaanjagende aantal studenten. Gelukkig zijn er de zeer uiteenlopende en boeiende gesprekken tijdens de middag in de "softmeetingroom", raadsels, ik-heb-een-vraag-punt-be-sessies enzovoort voor de nodige afleidingen. Ook buiten de uren wordt deze toffe sfeer uitgedragen tijdens ribbetjesfestijnen of kartraces, (soms verhitte) gezelschapsspelen of games. Daarom een dikke merci aan Arne, Arnout, Dieter, Dries B., Dries V.B., Duygu, Gert-Jan G., Gert-Jan S., Giorgos, Hossein, Igor, Irven, Kamil, Laura, Luigi, Marco, Michiel, Mykola, Nick, Niels, Olivier, Paolo, Patrick, Pieter, Quinten, Robbe, Sam A., Sam L., Seppe, Simon, Steven, Thomas A., Thomas C., Thomas D., Yves en Zdravko.

Het begin van mijn avontuur in de EM-groep werd echt gevormd tijdens mijn masterthesis waarin ik werd bijgestaan door Gert-Jan. Niet alleen bleek hij een begenadigd onderzoeker te zijn met een unieke mix aan theoretisch inzicht en praktische kennis/vaardigheden, hij was vooral heel behulpzaam en spitsvondig en dus de ideale begeleider, collega en uiteindelijk vriend. Bedankt om me de krochten van LaTeX en TikZ te leren ontdekken, bedankt voor je advies over van alles en nog wat en de fijne gesprekken. Ik bewonder bovendien enorm je doorzettingsvermogen en toekomstvisie.

Enkele mensen hebben op hetzelfde moment als mij hun doctoraat aangevangen in onze groep. Bedankt Arne voor je enorme inzet en kennis maar toch ook vooral voor je no-nonsense attitude. Merci Dries voor de leuke discussies, je joie-de-vivre en de Kempische toets in dit verre Oost-Vlaanderen. Irven, ik bewonder je enorm voor je drive en je soms toch wel zotte projecten. Bedankt ook voor de fijne momenten tijdens de Spaanse lessen. Je bent een uitzonderlijk persoon, Niels, en dit bedoel ik op de meest positieve manier mogelijk. Jouw interesse in de elektromagnetische geschiedenis en straffe verhalen zorgden altijd voor de nodige animo. Merci Olivier voor de interessante babbels en je nuchterheid. Bedankt Steven om te proberen me de details van Sobolev-ruimtes bij te brengen en onze filmdiscussies (*The eagles* zijn geen plot hole!).

Fandom mixups, logical fallacies, waanzinnige (maar niet gedroomde!) song inceptions ... zijn allemaal zaken die we hebben afgeleerd onder de heerschappij van onze chef, Simon. Initieel aarzelend maar later volledig opgaand in zijn rol als bureauverantwoordelijke, leidt Simon al bijna drie jaar bureau 210.006 met ijzeren hand. Maar genoeg gezeverd: bedankt Simon voor alle hulp met computergerelateerde zaken, van Python en Linux tot orde scheppen in de chaos van het

thesislokaal. Merci ook voor de leuke en grappige momenten zowel buiten als binnen jouw domein. Als mijn MoM-buddy, Michiel, staan we zij aan zij in de strijd tegen die heidenen met hun fancy, bewegende figuren. Pfff, show-offs! Bedankt om altijd klaar te staan voor mijn vragen en twijfels of een klankbord te zijn als ik met iets zat. Ik waardeer ook enorm dat je zo vaak onze gastheer/initiatiefnemer bent voor een toffe gezelschapsspelenavond. Kortom, je bent een geweldige collega én mens ook al wil je dat zelf niet altijd volledig geloven.

A big thank you to Paolo as well. I really appreciate our time together in our office in the Technicum (and at SPI). I enjoyed your company and our conversations, in particular, our language-related talks, which have provided me with a lot of insight in both Italian and Dutch. I really liked the time we shared in our new office after the move, however brief it may have been, Zdravko, Marco and Giorgos. Thank you for the nice laughs and the stares. My gratitude extends to Hossein as well, who brought a particular energy and atmosphere to our room that I really learned to appreciate. Thank you, Duygu, for brighting up our somber moods with your kindness. Kamil, your drive and perseverance are unparalleled as well as your eagerness to help each and everyone of us. You deserve the fullfillment of all your dreams and ambitions. Bedankt Gert-Jan, om zowel als mijn rechter- als linkerbuur op tijd en stond met de nodige gevatte en droge opmerking uit te hoek te komen. Merci Thomas voor je opgewekte persoonlijkheid en merci om tegelijkertijd de stem van redelijkheid en die van de zotte ideeën in deze bureau te zijn; een verrassende maar welgekomen mix. Bedankt ook aan Quinten en Thomas D., onze hoogsteigen sons of Maxwell, om de nodige coolfactor te brengen in dit nerdlandschap en voor jullie grappen en grollen. Merci Sam voor de constructieve babbels en de passie die je overbrengt over je interesses. Nick, bedankt voor je technische skills en je smakelijke verhalen en beschrijvingen. De nieuwste generatie doctoraatsstudenten, zijnde Dries, Igor, Laura, Pieter en Seppe, wens ik het allerbeste toe. In het bijzonder gaat mijn sympathie uit naar Dries, die zich heeft laten ompraten om op dit eigenste onderwerp verder te werken. Probeer niet overal cilinders in te zien, dat wordt na een tijdje nogal vervelend.

Van een toevallige ontmoeting in de gangen van het Technicum na een flard Spaans gehoord te hebben tot een wekelijkse taallunch: gracias por todo, Gemma. Me encanta nuestra conversaciones y comidas. Gracias por enseñarme como preparar una verdadera tortilla de patatas y gracias para ayudarme practicar español. Espero que encuentres la luz del sol figurativa en Bélgica sombría y mucha éxito en leer los libros neerlandés.

Erica is bijna eigenhandig de oorzaak van mijn verbeterde conditie t.o.v. het begin van mijn doctoraat door mij te overtuigen 's morgens voor dag en dauw een uur het zwembad in te duiken. Bedankt om er voor me te zijn als ik het nodig heb en voor de fijne gesprekken. Merci Arend voor de zeer uiteenlopende babbels en absurde discussies. Net omdat we elkaar misschien de laatste tijd niet meer zo veel hebben gezien, Pieter, koester ik onze samenkomsten en nostalgische uitweidingen des te meer.

's Avonds heb ik de laatste tweeënhalf jaar mijn uren dikwijls opgevuld met taken van de specifieke lerarenopleiding. Ik zou moeiteloos een boek kunnen vullen de dikte van dit doctoraat met wat ik heb geleerd en vooral niet geleerd heb tijdens deze opleiding. Ik zou zelfs graag kunnen zeggen dat dit een grove overdrijving is, maar helaas. Vraag gerust aan de collega's, vrienden en familie of gewoonweg iedereen die ik te pakken kreeg hoeveel ik over deze lessen heb gezaagd. Maar we zullen het maar beschaafd houden. Onder het motto gedeelde smart is halve smart wil ik hier dan ook uitdrukkelijk de medecursisten van deze opleiding in de bloemetjes zetten. Samen hebben we, strompelend en vloekend, de eindmeet gehaald en ik ben ervan overtuigd dat jullie allemaal stuk voor stuk uitstekende leerkrachten kunnen en zullen zijn. Bedankt en dikke proficiat aan Julita, Ramses, Cedric, Evi, Michiel, Steven en alle andere.

In de loop der jaren heb ik heel wat fijne eetgelegenheden mogen leren kennen in Gent samen met Leen, Jeroen en Cedric. Hopelijk kunnen we deze traditie nog lang in ere houden. Ook onze andere activiteiten met onder andere onze vlotte ontsnapping uit de escape room zullen me altijd bijblijven. Bedankt Leen voor je gepassioneerde verhalen en je ontwapenende (glim)lach. Merci Cedric om me mee in het SLO-verhaal te nemen. Het was een helse tocht maar ik heb er absoluut geen spijt en dit is grotendeels aan jouw steun te danken. Tussen je sarcastische opmerkingen na (en op een onbewaakt moment, tijdens) de lessen over pedagogische utopieën zitten een aantal pareltjes die ik nooit zal vergeten. In het algemeen ben ik je gigantisch dankbaar voor je vriendschap, onze luchtige en minder luchtige gesprekken, je overgave bij alles wat je onderneemt en je hulp bij van alles en nog wat.

Mijn Gents avontuur heeft vanzelfsprekend zijn roots in Turnhout, waar ik het genoegen heb deel uit te maken van een hechte vriendengroep. Bedankt Kenneth en Nikki, Niels en Dorien en Tom en Laura voor de ontelbare aantal leuke avonden en dagen. Of het nu restaurants uitproberen of gewoon iets gaan drinken is, dan wel een film meepikken of een gezelschapsspel spelen is, met jullie is het altijd fijn vertoeven. Moge we nog vele malen oudjaar met elkaar doorbrengen! Specifiek ook merci aan mijn oudste en beste vriend Niels. Het begin van onze vriendschap is, zelfs voor onszelf, dan wel in de mist ter tijden verloren gegaan maar ik ben enorm blij dat we elkaar toch op een gegeven moment hebben leren kennen en dat die klik heeft plaatsgevonden. Samen hebben we vele avonturen, groot en klein, meegemaakt met als culminatie de vijf jaren die we deelden op kot waar we vele vuren (of ijspegels) hebben doorstaan. Bedankt voor al die rijkgevulde jaren. Merci Senne voor je inkijk in het ingenieursleven in het Hoge en iets minder Hoge Noorden.

Ondanks het feit dat — of misschien net doordat — mijn familie langs beide kanten eerder klein is, zijn we een hechte groep. Bedankt voor de leuke familiefeesten, bijeenkomsten en andere activiteiten doorheen de jaren. Merci, oma, om ons op te vangen tijdens vakanties en ons dan te verwennen met allerlei zelfgemaakte lekkernijen. Ook bedankt om me al die jaren voor en na de muziekschool gebruik te

laten maken van je piano om last-minute begeleidingspraktijkhuiswerk te maken. Sophie, ik heb enorm genoten van onze Amerikaanse roadtrip vorig jaar maar ik ben je ook vooral heel dankbaar voor je luisterend oor. Het is een enorme geruststelling om te weten dat er, ook in Gent, altijd een plaats is waar ik terecht kan met alles in je warme nest samen met Abou Dar. Uiteraard een dikke merci aan mijn zus, Lies. Jouw creativiteit en praktische ingesteldheid blijven me keer op keer verbazen. Het maakt me bovendien enorm trots als grote broer om je jouw eigen vleugels te zien uitslaan samen met Jonas en er altijd voor te blijven gaan.

Natuurlijk is dit dankwoord niet compleet zonder een woordje gericht aan mijn ouders. Zonder jullie onvoorwaardelijke steun en niet-aflatende hulp zou ik nooit van mijn leven tot dit punt geraakt zijn. Bedankt om jullie interesse te blijven tonen ook al werd het stilaan allemaal een ver-van-jullie-bedshow. Om in de — toch wel overdreven — stijl te blijven van de nieuwjaarsbrieven van weleer beloof ik, als jullie kapoen, altijd mijn best te blijven doen.

Gent, april 2019
Martijn Huynen

"I like the cover," he said. "Don't Panic.
It's the first helpful or intelligible thing anybody's said to me all day."

DOUGLAS ADAMS

Contents

Samenvatting

De ongebreidelde verspreiding van elektronische apparaten in een groeiend aantal toepassingen wordt voortgestuwd door inspanningen om tegemoet te komen aan de explosieve vraag naar (draadloze) connectiviteit in onze technologiegerichte globale maatschappij. Deze toepassingen variëren van de vertrouwde computers en smartphones, over smartwatches en virtual reality tot zelfrijdende auto's en slimme steden. Deze verscheidenheid en groeiende complexiteit brengen een heleboel nieuwe technologieën en trends met zich mee om het hoofd te bieden aan de bijhorende uitdagingen. De overgang van berichten met een lage bandbreedte naar breedbandige communicatiekanalen op alomtegenwoordige mobiele toestellen heeft bijvoorbeeld geleid tot 5G, de opkomende standaard voor bliksemsnel mobiel internet. Hiermee samenhangend is er de internet der dingen (r)evolutie, waarbij *doorsnee* elektronische apparaten zoals computers of tablets verbonden worden via het internet met *slimme* versies van alledaagse toestellen zoals thermostaten, weegschalen, enz., wat leidt tot een huis vol moderne functionaliteit. Deze trend om communicatiemogelijkheden in te bouwen in allerlei apparaten beperkt zich niet tot een enkele woning, maar vindt zijn toepassingen in onder andere winkels, ziekenhuizen en de transportsector.

De opkomende technologieën en ontwikkelingen veranderen niet alleen communicatieprotocollen en -systemen; hun impact reikt volledig tot op het hardwareniveau. De integratie van elektronica in een brede waaier aan toestellen en materialen, de stijgende bitsnelheden en de niet-aflatende drang tot miniaturisatie, brengen steeds complexere en innovatievere geïntegreerde circuits en printplaten met zich mee. Helaas heeft elke medaille een keerzijde. Moeilijkheden en complicaties kunnen de kop opsteken in talloze domeinen, maar als we focussen op elektromagnetische compatibiliteit en signaal- en vermogensintegriteit, worden moderne circuits meer en meer geconfronteerd met fenomenen zoals daar zijn signaalverzwakking, distorsie, dispersie, overspraak, enz. Al deze effecten kunnen een nadelige invloed hebben op de juiste werking van het desgevallende systeem. Om een duur en tijdrovend herontwerp te vermijden op het einde van het productieproces is het van cruciaal belang dat ontwerpers potentiële problemen zo snel mogelijk opsporen. Om tegemoet te komen aan deze eis moeten de applicaties voor computergestuurd ontwerp voortdurend evolueren om accuraat en relevant te kunnen blijven.

Simulatieprogramma's hebben over de jaren heen een opvallende evolutie doorgemaakt. Circuitsimulators, die de wetten van Kirchhoff toepassen, zijn het startpunt en standaard hulpmiddel voor vele ontwerpers. Ze kennen echter nogal sterke beperkingen daar ze de golfverschijnselen van de elektromagnetische velden niet in rekening brengen. Zodoende zijn ze enkel inzetbaar zolang de dimensies van het

circuit in kwestie beduidend kleiner zijn dan de relevante golflengte. Met de huidige kloksnelheden en datadebieten wordt deze voorwaarde heel vaak geschonden en is het onvermijdelijk om over te schakelen op elektromagnetische simulatiesoftware, die de wetten van Maxwell hanteren, om de traditionele programma's bij te staan of zelfs te vervangen. Elektromagnetische simulators bestaan in allerlei vormen en maten en steunen op een of meerdere wiskundige technieken om Maxwells stelsel van partiële differentiaalvergelijkingen op te lossen. Tweedimensionale (2D) oplossingsmethodes waarbij structuren met een invariante dwarsdoorsnede, bijvoorbeeld transmissielijnen, worden doorgerekend, werden eerst ontwikkeld. Door deze 2D technieken aan te wenden om het zogenaamde binnenprobleem op te lossen en het buitenprobleem over te laten aan een driedimensionale (3D) techniek verhoogt men de accuraatheid. Dit dicht bovendien ook de kloof naar volledig 3D oplossingsmethodes.

Ongeacht de specifieke 3D simulator en zijn onderliggende werkingsprincipes, is een van de meest uitdagende elektromagnetische fenomenen om nauwkeurig te modelleren het *skineffect*. In goede geleiders nemen de elektromagnetische velden exponentieel af in het volume en dit effect wordt prominenter naarmate de frequentie stijgt waardoor de velden steeds sterker worden beperkt tot het oppervlak. Voor volumetrische technieken veroorzaken dergelijke materialen een ongeremde groei in het aantal onbekenden. Oppervlaktemethodes worstelen dan weer met een nauwkeurige numerieke integratie van de greense functie in het geleidende medium. Gezien de alomtegenwoordigheid van geleiders in schakelingen en antennes, en het feit dat dit fenomeen de onderliggende oorzaak is van vele signaalintegriteitsproblemen, is het uiterst belangrijk dat efficiënte en nauwkeurige modellen voor deze materialen worden ontwikkeld. In dit proefschrift presenteren we een nieuwe techniek voor het breedbandmodelleren van goede geleiders zonder te vertrouwen op benaderingen.

De voorgestelde differentiële oppervlakte-admittantie-operator introduceert een breedbandige, *globale* en exacte betrekking tussen het tangentiële elektrische en magnetische veld op het randoppervlak van een volume; dit in tegenstelling tot de populaire oppervlakte-impedantievoorwaarde, die een *lokale*, benaderende voorwaarde oplegt, enkel geldig voor geleiders wiens skineffect sterk ontwikkeld is en dit in een beperkt frequentiebereik. In Hoofdstuk 3 wordt een uitdrukking voor de driedimensionale differentiële oppervlakte-admittantie-operator voor niet-magnetische, homogene materialen opgesteld die integralen met de greense functie in geleidende media omzeilt. In plaats daarvan vertrouwt de operator op de eigenfuncties van een caviteit met perfect elektrisch geleidende wanden met dezelfde vorm als het bestudeerde object. Hoewel deze operator opgesteld kan worden voor eender welke vorm, zorgt de afhankelijkheid van de eigenfuncties ervoor dat hij het eenvoudigst kan worden afgeleid voor lichamen wiens eigenfuncties analytisch berekenbaar zijn.

De 3D differentiële oppervlakte-admittantie-operator wordt in Hoofdstuk 4 toegepast op verstrooiings- en antenneconfiguraties. Hiervoor worden de eigenfuncties

van een cilinder bepaald en aangewend om de differentiële operator op te bouwen. Deze wordt vervolgens gediscretiseerd met een specifieke verzameling basisfuncties, namelijk gekromde dakfuncties. Deze functies zijn speciaal afgestemd voor gebruik op de mantel van een cilinder aangezien ze diens gekromde aard bewaren. Een overeenstemmende momentenmethode wordt naderhand toegepast op de elektrischeveldintegraalvergelijking met diezelfde basisfuncties, waardoor een volledige randintegraalvergelijkingsformulering voor cilinders wordt bekomen. Vervolgens wordt de aanbevolen techniek benut om verstrooiing aan verschillende materialen te bestuderen en om antenne-eigenschappen voor veranderende geleidbaarheden te evalueren, hetgeen de nauwkeurigheid van de methode aantoont in vergelijking met bestaande softwarepakketten.

Een tweede domein waar de differentiële oppervlakte-admittantie-operator wordt toegepast, omvat de karakterisering van (elektronische) interconnecties. Twee verschillende randintegraalvergelijkinsformuleringen worden gespecificeerd die de 3D differentiële oppervlakte-admittantie-operator inlijven om het binnenprobleem van geleiders aan te pakken. De eerste maakt gebruik van een circuitinterpretatie die kan worden opgelost met de vertrouwde circuitsimulators om de weerstand en inductantie van interconnecties te bepalen. De tweede methode leidt tot een reeks matrixvergelijkingen die een volledige elektromagnetische karakterisering mogelijk maken. De differentiële oppervlakte-admittantie-operator zelf wordt opgesteld op twee manieren. Gebaseerd op de eigenfuncties van de balk, discretiseert de eerste methode de operator rechtstreeks met lokale basisfuncties. De alternatieve aanpak past volledigedomainbasisfuncties toe als tussenstap. Dit resulteert in een meer nauwkeurige en krachtige gediscretiseerde operator, in het bijzonder voor geleiders. Uiteindelijk worden de voorgestelde methodes vergeleken in termen van nauwkeurigheid en doeltreffendheid. Bovendien worden ze toegepast op een groot aantal voorbeelden. Door te vergelijken met een aantal academische technieken, commercieel beschikbare softwarepakketten en meetresultaten, wordt de validiteit en bruikbaarheid van de gepresenteerde methodes aangetoond.

De beperking tot niet-magnetische materialen voor de 3D differentiële oppervlakte-admittantie-operator wordt opgeheven voor de balk in Hoofdstuk 6. Een nieuwe admittantie-operator wordt voorgesteld, rechtstreeks bepaald als het verschil tussen twee Poincaré-Steklov-operators. Dit wordt bereikt door de configuratie van beide operators te beschouwen als de superpositie van zes perfect elektrische geleidende golfgeleiders met een gemetalliseerd uiteinde waardoor materialen met zowel een elektrisch als magnetisch contrast in rekening gebracht kunnen worden.

In het afsluitende hoofdstuk worden de voornaamste conclusies van dit proefschrift neergepend, gevolgd door een beknopte beschrijving van mogelijke verbeteringen en/of uitbreidingen van het beschreven werk. Deze toekomstmogelijkheden kunnen leiden tot een performante elektromagnetische simulator die hopelijk zijn steentje kan bijdragen aan het vormen van de wereld van morgen.

Summary

The proliferation of electronic devices in an ever increasing range of applications has been driven by efforts to cater to the population's exploding demand for (wireless) connectivity in our technology-oriented global society. These applications range from the familiar computers and smartphones, over smartwatches and virtual reality to self-driving cars and smart cities. This diversity and growing complexity has spawned many new technologies and trends to face the accompanying challenges. The move from low-bandwidth messages to high-bandwidth communication channels on ubiquitous mobile devices has led, for example, to 5G, the upcoming standard for ultra-fast mobile internet. Tied in with this, is the Internet of Things (r)evolution, where *standard* electronic devices such as computers or tablets are connected over the internet with *smart* variants of everyday objects such as thermostats, scales, etc., creating a fully interconnected home. This trend of integrating connectivity capabilities in all sorts of devices is not confined to a single house, but finds applications in stores, hospitals and the transportation industry, among others.

The emerging technologies and trends do not only alter communication protocols and systems, but their impact reaches all the way down to the hardware level as well. The integration of electronics in a wide variety of appliances and materials, the rising bit rates and the unrelenting urge for miniaturization, have all brought about progressively more innovative and complex integrated circuits and printed circuits boards. However, these solutions come at a cost. Issues/roadblocks can arise in a myriad of domains, but focusing specifically on the electromagnetic compatibility and signal and power integrity, modern circuitry is increasingly faced with phenomena such as signal attenuation, distortion, dispersion, crosstalk, etc. All these effects can have an adverse influence on the correct operation of the systems in question. For the sake of avoiding costly redesign at the end of the production process, it is therefore crucial for designers to detect potential problems as soon as possible. To accommodate this need, computer-aided design (CAD) tools have to continue evolving to stay accurate and relevant.

Simulation tools have indeed seen a remarkable progression throughout the years. Circuit solvers, which apply Kirchhoff's laws, are the starting point and go-to solvers for many designers. Unfortunately, they are only valid insofar the wave nature of the fields does not play up, i.e., as long as the circuit is electrically small. With current clock speeds, these conditions are often no longer met and electromagnetic (EM) solvers that tackle Maxwell's equations are required to complement/replace circuit simulators. EM solvers come in all shapes and sizes and they are based on one or more mathematical techniques to numerically solve Maxwell's set of partial differential equations. Two-dimensional (2-D) solvers were developed first, ana-

lyzing structures with a fixed cross-section, e.g., computing transmission line parameters. Embedding these 2-D solvers that solve the interior problem into three-dimensional (3-D) formulations for dealing with the exterior problem improves the accuracy and bridges the gap to full 3-D solvers.

Regardless of the specific 3-D solver and its core working principle, one of the more challenging electromagnetic phenomena to model accurately is the skin effect. In good conductors, the electromagnetic fields decay exponentially in their bulk and this effect strengthens with rising frequencies, increasingly constraining the fields to the surface. For volumetric methods, these materials cause a rampant increase in the number of unknowns while boundary-based methods struggle with the accurate numerical integration of the Green's function in the conductive medium. Given the pervasive presence of good conductors in circuits and antennas, and the fact that this phenomenon is the underlying root of many signal integrity problems, it is imperative that efficient and accurate models are developed for these types of materials. In this dissertation, we present a novel technique for the broadband modeling of good conductors without relying on approximations.

The proposed differential surface admittance operator introduces a broadband, *global* and exact relationship between the tangential electric and magnetic field on the boundary surface of a volume; this in contrast to the popular surface impedance condition, which implements a *local*, approximate condition, only valid for conductors with a strongly developed skin effect in a limited frequency range. In Chapter 3, an expression for the 3-D differential surface admittance operator for nonmagnetic, homogeneous materials is constructed that avoids integrals involving the Green's function of the (conductive) medium. Instead, it relies on the eigenfunctions of a perfect electric conductor cavity with the same shape as the object under study. Although this operator can be constructed for any volume, its reliance on the eigenfunctions implies that it is most easily obtained for shapes with analytically calculable eigenfunctions.

The 3-D differential surface admittance operator is applied to scattering and antenna configurations in Chapter 4. For this, the eigenfunctions of a cylinder are calculated and employed to construct the differential operator, which is subsequently discretized using a particular set of basis functions, i.e., curved rooftop functions. These rooftops are specially tailored to use on the mantle of a cylinder, preserving its curved nature. Accordingly, a congruent Method of Moments discretization of the electric field integral equation with the same set of functions is constructed, yielding a comprehensive boundary integral equation formulation for cylinders. Afterwards, the advocated technique is utilized to study scattering at various materials and to evaluate antenna characteristics for varying conductivity values, demonstrating its accuracy by comparison with existing simulation software packages.

Another application domain where the differential surface admittance operator is deployed, comprises the characterization of interconnects. Two different boundary integral equation formulations are specified that incorporate the 3-D differential

surface admittance operator to deal with the interior problem of conductors. The first one leverages a circuit interpretation that can be solved by traditional circuit solvers to compute the resistance and inductance of interconnects, while the second leads to a set of matrix equations that enable a full-wave characterization. The differential surface admittance operator itself is constructed in two ways. Based on the eigenfunctions of a cuboid, the first realization directly discretizes the operator with standard local basis functions. The alternative approach applies entire domain basis functions on the faces of the cuboid as an intermediate step. This results in a more accurate and powerful discretized operator, especially for good conductors. In the end, the proposed methods are compared in terms of accuracy and efficiency, and are employed to characterize a plethora of examples and applications. Comparison with a number of academic techniques, commercial tools and measurement results testifies to the validity and appositeness of the advocated methods.

The restriction to nonmagnetic materials for the 3-D differential surface admittance operator is alleviated in Chapter 6 for cuboids. A novel admittance operator is proposed, directly constructed as the difference of two Poincaré-Steklov operators. This is achieved by deeming the configuration for each operator as the superposition of six perfect electric conductor waveguides with a metallized end, allowing for materials with both an electric and magnetic contrast.

In the final chapter, the main conclusions to this dissertation are formulated accompanied by a brief description of some possible improvements and/or extensions on the presented work. These future avenues could lead to a full-blown EM CAD tool, that can hopefully play its part in shaping the world of tomorrow.

List of Abbreviations

2-D	two-dimensional
3-D	three-dimensional
ABC	absorbing boundary condition
ANSYS	Analysis Systems
BEM	boundary element method
BIE	boundary integral equation
CAD	computer-aided design
CEM	computational electromagnetics
CST	Computer Simulation Technology
DC	direct current
DtN	Dirichlet-to-Neumann
EFIE	electric field integral equation
EM	electromagnetic
EMC	electromagnetic compatibility
FDM	finite difference method
FDTD	finite-difference time-domain
FEM	finite element method
FIT	finite integration technique
GO	geometrical optics
HFSS	High Frequency Simulation Software
IC	integrated circuit
ILS	instrument landing system
IoT	internet of things
ITO	indium tin oxide
MLFMM	multilevel fast multipole method
MoM	Method of Moments
MPIE	mixed potential integral equation
MRI	magnetic resonance imaging
MWS	Microwave Studio
NEC	Numerical Electromagnetics Code
NFC	near-field communication
PCB	printed circuit board
PEC	perfect electric conductor / perfect electrically conducting
PEEC	partial element equivalent circuit
PI	power integrity
PMCHWT	Poggio-Miller-Chan-Harrington-Wu-Tsai
PML	perfectly matched layer
p.u.l.	per unit of length
QED	quantum electrodynamics

RCS	radar cross-section
RFID	radio-frequency identification
rms	root mean square
RWG	Rao-Wilton-Glisson
SI	signal integrity
TE	transverse electric
TM	transverse magnetic
UTD	uniform theory of diffraction
VIE	volume integral equation

List of Symbols

In the following list x and $\mathbf{x}$ are used as placeholder for scalar and vectors, respectively, except when referring to the x-coordinate, which is clearly stated in such cases.

j	the imaginary unit
x^*	complex conjugate
$\mathrm{Re}[x]$	real part of x
$\mathrm{Im}[x]$	imaginary part of x
$\mathbf{x}$	vector (in the frequency domain)
$\bar{\mathbf{x}}$	vector (in the time domain)
$\overline{\overline{X}}$	matrix
$\hat{\mathbf{x}}$	unit vector
$\hat{\mathbf{x}}, \hat{\mathbf{y}}, \hat{\mathbf{z}}$	unit vectors along the three Cartesian axes, i.e, x, y and z
$\hat{\boldsymbol{\rho}}, \hat{\boldsymbol{\phi}}, \hat{\mathbf{z}}$	unit vectors along the three cylindrical axes, i.e, ρ, ϕ and z
$\hat{\mathbf{r}}, \hat{\boldsymbol{\theta}}, \hat{\boldsymbol{\phi}}$	unit vectors along the three spherical axes, i.e, r, θ and ϕ
$\boldsymbol{\rho}$	point in 2-D space
$\mathbf{r}$	point in 3-D space
R	Euclidean distance between two points $\mathbf{r}$ and $\mathbf{r}'$
$\mathcal{V}$	(un)bounded volume
$\mathcal{S}$	boundary surface
$\hat{\mathbf{n}}$	normal vector to a surface $\mathcal{S}$
$\mathbf{x}^t$	Tangential components of $\mathbf{x}$ with respect to $\mathcal{S}$
f	frequency
ω	angular frequency ($\omega = 2\pi f$)
ϵ	permittivity of a medium
ϵ_0	permittivity of vacuum ($8.854\,187\,817\ldots 10^{-12}\,\mathrm{F/m}$)[1]
ϵ_r	relative permittivity of a medium ($\epsilon = \epsilon_r \epsilon_0$)
μ	permeability of a medium
μ_0	permeability of vacuum ($4\pi 10^{-7}\,\mathrm{H/m}$)[1]
μ_r	relative permeability of a medium ($\mu = \mu_r \mu_0$)
σ	electrical conductivity of a medium
c	speed of light in a medium
c_0	speed of light in vacuum ($299\,792\,458\,\mathrm{m/s}$)[1]

[1] At the time of writing, the values of c_0, μ_0 and ϵ_0 are exact. However, with the impending redefinition of SI base units (coming into force in May 2019) only the speed of light in vacuum will remain exact and ϵ_0 and μ_0 will be subject to experimental error.

Z_c	wave impedance or characteristic impedance ($Z_c = \sqrt{\mu/\epsilon}$)
k	wavenumber in a medium ($k = \omega\sqrt{\epsilon\mu}$)
η	contrast parameter ($(k^2 - k_0^2)/j\omega\mu_0$)
δ	skin depth ($\delta = \sqrt{2/\omega\mu\sigma}$)
$\mathbf{e}$	electric field
$\mathbf{h}$	magnetic field
$\mathbf{b}$	magnetic induction
$\mathbf{d}$	electric induction
$\mathbf{j}$	electrical current density
ρ	electrical charge density
$\mathbf{a}$	vector potential
ϕ	scalar potential
$\mathbf{j}_s$	electrical surface current density
ρ_s	electrical surface charge density
$\mathbf{m}_s$	magnetic surface current density
δ_{ij}	Kronecker delta (1 if $i = j$, 0 if $i \neq j$)
ε_i	Neumann factor (1 if $i = 0$, 2 if $i \neq 0$)
σ_i	sign factor (0 if $i = 0$, 1 if $i \neq 0$)
$\delta(x)$	Dirac delta (generalized) function
$G(R)$	Green's function
$\mathbf{f}(\mathbf{r})$	basis function
$\mathbf{t}(\mathbf{r})$	test function
$J_n(x)$	Bessel function of the first kind of order n
$J_n'(x)$	derivative of the Bessel function of the first kind of order n
x_{mn}	m-th zero of $J_n(x)$
y_{mn}	m-th zero of $J_n'(x)$
ν	triple index
$\mathbf{f}_\nu$	irrotational electric eigenfunctions
$\mathbf{e}_\nu$	solenoidal electric eigenfunctions
$\mathbf{g}_\nu$	irrotational magnetic eigenfunctions
$\mathbf{h}_\nu$	solenoidal magnetic eigenfunctions
$\mathcal{T}$	electric field integral equation (EFIE) operator
$\mathcal{P}$	Poincaré-Steklov operator
$\mathcal{Y}$	differential surface admittance operator

List of Publications

Articles in international journals

- M. Huynen, M. Gossye, D. De Zutter, and D. Vande Ginste, "A 3-D differential surface admittance operator for lossy dipole antenna analysis", *IEEE Antennas Wireless Propag. Lett.*, vol. 16, pp. 1052–1055, 2017.
- M. Gossye, M. Huynen, D. Vande Ginste, D. De Zutter, and H. Rogier, "A Calderón preconditioner for high dielectric contrast media", *IEEE Trans. Antennas Propag.*, vol. 66, no. 2, pp. 808–818, Feb. 2018.
- M. Huynen, D. De Zutter, and D. Vande Ginste, "Rigorous full-wave resistance and inductance computation of 3-D interconnects", *IEEE Microw. Wireless Compon. Lett.*, vol. 28, no. 6, pp. 455–457, Jun. 2018.

Articles in conference proceedings

- M. Huynen, D. De Zutter, and D. Vande Ginste, "Boundary integral equation study of the influence of finite conductivity on antenna radiation using a 3-D differential surface admittance operator", in *2017 International Applied Computational Electromagnetics Society Symposium - Italy (ACES)*, vol. 2, Mar. 2017, pp. 1–2.
- M. Huynen, D. De Zutter, and D. Vande Ginste, "A fully 3-D BIE evaluation of the resistance and inductance of on-board and on-chip interconnects", in *2018 IEEE 22nd Workshop on Signal and Power Integrity (SPI)*, May 2018, pp. 1–4.
- M. Huynen, D. De Zutter, and D. Vande Ginste, "Broadband full-wave BIE impedance characterization of 3-D interconnects", in *2018 IEEE 27th Conference on Electrical Performance of Electronic Packaging and Systems (EPEPS)*, Oct. 2018, pp. 241–243.

Articles submitted to international journals

- M. Huynen, X. Sun, G. Van der Plas, E. Beyne, D. De Zutter, and D. Vande Ginste, "Entire domain basis function expansion of the differential surface admittance for efficient broadband characterization of lossy interconnects", *IEEE Trans. Microw. Theory Techn.*, submitted for publication.

Scientific awards

- Best Student Paper Award for the paper entitled "Boundary Integral Equation Study of the Influence of Finite Conductivity on Antenna Radiation Using a 3-D Differential Surface Admittance Operator," presented at the International Applied Computational Electromagnetics Society (ACES) Symposium, Florence, Italy, March 2017.
- imec master's dissertation award for the best master thesis in engineering for the work entitled "EMC-Aware Design of a Low-Cost Receiver Circuit under Injection Locking and Pulling", 2014.

A 3-D Differential Surface Admittance Operator for the Broadband Modeling of Lossy Conductors

1 Introduction

"But this is one corner of one country, in one continent, on one planet that's a corner of a galaxy, that's a corner of a universe that is forever growing and shrinking and creating and destroying and never remaining the same for a single millisecond. And there is so much — so much to see."

Eleventh Doctor, *Doctor Who*

1.1 Context

In recent years, an unprecedented expansion in communication systems and technologies has been fueled by the world's insatiable hunger and craving for information and global connectivity. In this day and age we take it for granted that we essentially have the world at our fingertips. With the click of a button or a *swipe* across the screen, we gain access to the world's shared knowledge and get into contact with people from around the world while mere decades ago, we still thought "digital watches are a pretty neat idea"[1].

The seemingly unbounded growth of electronic devices has brought along a myriad of contemporary trends and technologies that in turn lead to new challenges and solutions. Video on demand in combination with the ubiquitous use of mobile devices, for example, has led to the advent of 5G, the next generation of mobile communication networks. This new emerging standard has to deal not only with the ever increasing number of users and applications, but with the shift from low-bandwidth text- and/or speech-based messages to high-demand image/video-based communication as well. Examples of this new paradigm can be found in

[1] *The Hitchhiker's Guide to the Galaxy*, Douglas Adams

various domains, ranging from social media applications such as Instagram and FaceTime, to services such as telemedicine, teleconferencing, etc.

Another evolution that is gaining ground at breakneck speed is the inclusion of connectivity functionality in nontraditional devices, leading to the so-called internet of things (IoT). One would be surprised how many appliances are manufactured nowadays in a *smart* variety: thermostats, doorbells, refrigerators, coffee machines, ... leading to a home where everything is interconnected. Outside our homes, wireless technologies include radio-frequency identification (RFID) or near-field communication (NFC) with applications including contactless payment, shoplifting protection, interactive patient tags, ... Another area where the integration of electronics has taken off, is the transportation industry. Not only are modern vehicles jam-packed with user-oriented modules, e.g., multimedia consoles, satellite navigation, etc., a bunch of sensors and controllers safeguard the operation of the car and the safety of its passengers as well. With the onset of smart cars and/or self-driving cars, this integrated functionality will only increase further as the autonomy develops and inter vehicular information exchange advances through wireless communication networks.

The proliferation of these emerging technologies and trends does not only reshape communication systems and protocols, but it has repercussions on the hardware level as well in order to accommodate for the changing demands of the applications. The continuing push for miniaturization and the rising clock frequencies combined with the integration of circuitry in a wide range of devices and appliances, have led to increasingly intricate and innovative printed circuit boards (PCBs) and integrated circuits (ICs). Unfortunately, in one way or the other these solutions come at a cost. Examples of important challenges/concerns that designers face include manufacturability, process inaccuracies, mechanical instabilities, inhomogeneous heat distribution, signal integrity (SI) and power integrity (PI) degradation and electromagnetic compatibility (EMC) issues. Focusing on the electromagnetic problems, EMC and SI/PI cover a large group of effects such as distortion, ringing, dispersion, signal attenuation, skin effect and crosstalk that can have detrimental consequences on the proper operation of electronic systems. Designers use a variety of computer-aided design (CAD) tools in an attempt to assess and mitigate these problems as early as possible in the design cycle to avoid large costs later down the line. Therefore, it is of the utmost importance that the tools themselves evolve to remain reliable and accurate, keeping up to speed with new topologies and technologies.

1.2 Motivation

The tools utilized by electronics designers are in the first place the traditional circuit solvers. Applying Kirchhoff's laws, these flexible and versatile programs can characterize very large structures in a short amount of time. However, the underlying laws are only valid as long as the structure is electrically small, i.e., its

dimensions have to be much smaller than the wavelength at the highest operating frequency. At modern clock frequencies (around 3 GHz and higher), the free-space wavelength drops below 100 mm, implying that is no longer justified to consider ICs and certainly PCBs as electrically small. As such, circuit solvers no longer suffice to accurately predict the behavior of such structures, even with extensions such as transmission line theory. Hence, design engineers are increasingly dependent on electromagnetic (EM) solvers that do take the wave nature of the signals and fields into account by numerically solving Maxwell's equations.

Just like the structures they model, electromagnetic solvers have evolved over the years. For antenna applications, the early techniques modeled conductive, thin-wire structures, such as cylindrical wires [1] or dipole antennas [2], by means of a postulated current distribution. Interconnects, on the other hand, were modeled initially as pure two-dimensional (2-D) structures having a fixed cross-section with an initial focus on waveguides [3]–[5] that later expanded towards conductors [6]–[11]. As the structures shrunk further, the finite length was dealt with by combining 2-D techniques to solve the interior problem, taking the finite conductivity into account, with three-dimensional (3-D) methods to solve the exterior problem, leading to an overall more efficient solution [12]–[17]. This did not, however, negate the need for a full-blown 3-D solver, which has as such been researched extensively in a wide variety of applications [18]–[21].

One of the more challenging wave effects to model accurately is the skin effect, the phenomenon that the fields get progressively more confined to the surface of (good) conductors with rising frequencies. This effect is the underlying root of many SI problems such as dispersion, attenuation, the proximity effect, ... and as conductors are omnipresent in antennas and interconnects, adequate modeling of these materials is of paramount importance. Regardless of the employed computational electromagnetics (CEM) method, broadband modeling of the skin effect and related phenomena remains an open problem; low- and high-frequency limits and approximations are well-known and have widespread use, but in the intermediate frequency range accurate descriptions are notoriously challenging. In this dissertation, we propose a new approach to tackle this problem with specific interest in accuracy over a wide frequency range without relying on approximations.

1.3 Computational electromagnetics

In CEM, there is no panacea, no cure-all, no "solver to rule them all", neither in 2-D nor in 3-D. If this were indeed the case, research into numerical techniques would have come to an end in the past and this is clearly not the case. On the contrary, throughout the years, various methods have been developed, each specialized for certain types of configurations/problems. The goal of this section is to present a brief overview of the fundamentals of the three most commonly used families of methods, viz., finite element, finite difference and integral equation methods. Specific focus is directed to the latter category as all methods presented in this

dissertation are integral equation based. This list is by no means exhaustive; there are several other well-known techniques such as geometrical optics (GO) and uniform theory of diffraction (UTD) [22], not even mentioning hybrid methods that combine two or more types of solvers in an effort to get the best of both worlds.

1.3.1 Finite element methods

The finite element method (FEM) [23], [24] is used extensively in electromagnetics as well as in other engineering and physics domains such as structural mechanics and transport phenomena [25]. This technique meshes the entire volume of the problem under consideration, typically with triangles and/or tetrahedral elements but other shapes are employed as well. The unknown quantities are then expanded in basis functions that are defined locally on the mesh elements. To discretize a partial differential equation, it is weighted with test functions, often the same as the basis functions, i.e., *Galerkin* testing, so that the solution will satisfy the equation in the *weak* sense. This approach effectively transforms the continuous problem into a matrix equation with a large but sparse matrix at its core. The FEM is very apt at modeling intricate geometries and complex materials due to the flexibility of its unstructured mesh and the localized approximation of the sought-after quantities. However, its volumetric discretization results in a large number of unknowns leading to poor scaling and a high computational cost, especially in the case of good conductors where a very fine discretization is required to correctly capture the rapidly decaying fields in the material. Moreover, in order to approximate unbounded volumes, absorbing boundary conditions (ABCs) have to be employed to avoid reflections at the edge of the simulation domain. Additionally, as the FEM is usually applied in the frequency domain in EM (although time-domain formulations exist as well [26]), nonlinear effects cannot be taken into account.

1.3.2 Finite difference methods

Finite differences are predominantly applied in the time domain, leading to the finite-difference time-domain (FDTD) method [27], [28]. At its core, the FDTD method tackles Maxwell's equations by approximating derivatives by finite differences and discretizing the field quantities on a staggered, structured grid. Unknowns are updated in a leapfrog manner while the time advances in discrete steps until the desired time length is obtained. The FDTD method is conceptually the simplest of the three main CEM methods and since it does not need to store a system matrix, it scales better than the others. The volumetric grid also allows for the simulation of complex materials but, just like the FEM, ABCs or perfectly-matched layers (PMLs), are required to truncate the domain in case of unbounded domains. Moreover, the structured nature of the grid hinders the inclusion of more complex geometries. Various off-shoots of the FDTD have been developed to overcome this restriction, e.g., the finite integration technique (FIT) [29]. Being a

time domain method, the FDTD technique does allow for nonlinear media but on the other hand, dispersive materials prove to be more difficult. By performing a single simulation, broadband frequency results can by obtained in one fell swoop as long as the stability is guaranteed. Although this stability behavior is well understood, the required time step can become unreasonably small if a fine spatial resolution is required, such as is the case in the modeling of good conductors. For a well-documented overview of the state-of-the-art in overcoming such problems, the reader is referred to [30] and the references therein.

1.3.3 Integral equation methods

Integral equation methods solve Maxwell's equation by first determining the response of an impulse source placed in the background medium, i.e., the Green's function. Afterwards, through superposition, the response of any source is computed by convolution of the Green's function and the sources. The main advantage of this approach is that the unboundedness of the background medium is perfectly taken into account without relying on ABCs. As such, only objects not part of the background medium have to be meshed. The Achilles' heel of integral equation methods is the calculation of the Green's function, which can only be calculated analytically for a handful of simple configurations, fortunately including the essential homogeneous background medium. Computation of layered medium Green's functions, on the other hand, proves to be far more cumbersome and time-consuming [31]. Integral equations are usually formulated in the frequency domain but have been developed for the time domain as well [32].

Volume integral equation methods

The volume integral equation (VIE) method [33], [34] can be used to model inhomogeneous materials with very similar discretization strategies as the FEM but without the need for approximations to truncate the simulation domain because of the Green's function. However, there is a *quid pro quo*: in contrast to the FEM, the system matrix will be dense making the solution of the matrix equation much more inefficient than the sparse matrix of the FEM. Nonetheless, VIE based methods are being employed to model interconnects [16], [35]. This category includes the popular partial element equivalent circuit (PEEC) method [12], [36], which transforms the integral equation into an equivalent circuit enabling integration into conventional circuit solvers with subsequent integration capabilities of sources, discrete elements, etc. However, this does not circumvent the dense matrix problem; many elements in the formulation are coupled and this can result in large solution times as circuit solvers are not optimized for such intertwined, *dense* circuits. Note that due to the volumetric mesh, VIE methods face the same problem as the FEM when it comes to good conductors as the number of required mesh elements explodes with the decreasing skin effect.

Boundary integral equation methods

If the objects under consideration are filled with piecewise homogeneous materials, it suffices to only determine the unknowns on the boundaries, reducing the VIE to a boundary integral equation (BIE). Subsequent discretization leads to a boundary element method (BEM), also known as the Method of Moments (MoM) in electromagnetics [37]. As only the surface has to be meshed, the number of unknowns is tangibly lower than the related volumetric method, especially for conductors where this reduction in unknowns can be considerable, while keeping the advantages of the Green's function. The system matrix evolving from the BIE-MoM is dense, leading to a high computational cost for calculating its elements and solving the matrix system. In free-space scattering applications, the multilevel fast multipole method (MLFMM) [19] is leveraged to expedite the computations. Applying a similar strategy for PCB or IC structures, which comprise a layered background medium, is far more cumbersome (see [38] and the references therein).

A very general BIE method to simulate any homogeneous material is the Poggio-Miller-Chan-Harrington-Wu-Tsai (PMCHWT) technique [21]. Still, standard BIE methods are poorly suited for the modeling of good conductors as the numerical computation of MoM integrals involving the Green's function in a material with a strongly developed skin effect is an enormous challenge, almost nullifying the advantages of the BEM. Even if one employs computationally expensive techniques to bypass this complication [39], [40], the PMCHWT still has difficulty coping with the high dielectric contrast, instigating the need for the employment of (Calderón) preconditioners and/or specific basis functions to guarantee accurate solutions [41].

Differential surface admittance operator

Various fixes/approximations have been formulated over the years to overcome the difficulty in modeling materials in the skin effect regime. One of the most popular methods is the surface impedance concept [42], an approximation valid for conductors with a strongly developed skin effect in a geometry with moderate radius of curvature [43]. This *local* relationship enforced on the boundary of the object, relates the tangential electric and magnetic field, thus avoiding a direct solution of the interior problem. Despite various extensions [15], [44], [45], this method is not able to perform truly broadband simulations given its inherent assumptions.

The differential surface admittance operator introduces an exact, *global* relationship between the tangential electric and magnetic field on the boundary surface, valid over the entire frequency range. First introduced for 2-D based on a Dirichlet-to-Neumann (DtN) operator in [10], this operator can be constructed without computing integrals involving the Green's function in the lossy medium. It relies on the eigenfunctions of a perfect electric conductor (PEC) cavity with the same shape as the object under study. As such, it is most easily constructed for canonical shapes whose eigenfunctions can be calculated analytically or via an efficient algorithm,

viz., rectangles [10], circles [10], [46], tubes [47] and triangles [48]. It has been successfully applied to scattering problems [49] and to a variety of different interconnect cases [11], [50]–[52]. In [53], the authors present an extension of the 2-D differential surface admittance operator to arbitrary cross-sections. However, this approach reintroduces integrals involving the Green's function in the conductive medium and as such the need for a very fine (interior) mesh and the difficulty of the numerical integration should resurface. Yet, the authors claim that a simple quadrature rule and a modest number of pulse basis functions suffice to accurately calculate the operator. Additionally, in comparison with the results from [10], they state that the original method, which relies on the eigenfunctions, requires a finer discretization and more eigenmodes, contradicting the analysis in [10].

The same authors have integrated the 2-D differential surface admittance operator with a 3-D integral equation to model interconnects [14], [54]. This approach models the variation of the current in the 2-D cross-section but assumes the longitudinal current in each block to be constant, which proves to be detrimental to the accuracy of modeling corners/bends and thus for full 3-D interconnects. Recently, in [55], [56] an extension of this method to layered media was proposed, but this technique seems to be based on a mathematically questionable simplification of the occurring Sommerfeld integrals.

1.4 Outline

The goal of this work is to develop a fully 3-D differential surface admittance operator for the modeling of arbitrary homogeneous materials with a particular focus on lossy conductors, given their ubiquitousness in antenna and interconnect applications. The operator should be easily integrated in a BIE method to accurately and efficiently solve the problem at hand. In this way the technique can be utilized to characterize relevant scattering and interconnect problems.

In Chapter 2, we provide the fundamentals of EM theory used throughout this work. The theoretical concepts of the BEM in electromagnetics are discussed in this chapter as well. The general idea of the 3-D differential surface admittance operator is presented in Chapter 3. Moreover, two different derivations lead to an expression of the operator based on the eigenfunctions of the volume. In Chapter 4, we apply the differential surface admittance operator to cylinders and integrate it into a MoM framework. For this, we first propose a set of basis functions specifically designed for the mantle of circular cylinders. The approach to deal with the corresponding singular integrals is explained as well. Afterwards, the eigenfunctions of the cylinder are constructed and utilized to create the discretized differential surface admittance operator. The combination of this operator and the BIE is then employed to study scattering problems and characterize antenna performance for varying conductor conductivity values. The study of interconnects is tackled in Chapter 5. Thereto, two different BEMs are formulated that incorporate the differential surface admittance operator to model the lossy materials accurately. The

differential surface admittance operator is then derived for cuboids in two ways. The second approach applies entire domain basis functions in order to come to a more efficient and accurate computation of the operator. Its appositeness and validity are shown via various examples and applications through thorough comparison with several academic and commercial solvers. In the next chapter, i.e., Chapter 6, the differential surface admittance operator for cuboids is derived in an alternative way that enables both magnetic and dielectric contrast. This dissertation finishes with a formulation of the conclusions and avenues for future work in Chapter 7.

References

[1] E. Cassedy and J. Fainberg, "Back scattering cross sections of cylindrical wires of finite conductivity", *IRE Trans. Antennas Propag.*, vol. 8, no. 1, pp. 1–7, Jan. 1960.

[2] R. King, C. Harrison, and E. Aronson, "The imperfectly conducting cylindrical transmitting antenna: Numerical results", *IEEE Trans. Antennas Propag.*, vol. 14, no. 5, pp. 535–542, Sep. 1966.

[3] J. Collins and P. Daly, "Calculations for guided electromagnetic waves using finite-difference methods", *Journal of Electronics and Control*, vol. 14, no. 4, pp. 361–380, 1963.

[4] P. Arlett, A. Bahrani, and O. Zienkiewicz, "Application of finite elements to the solution of Helmholtz's equation", *Proc. Inst. Electr. Eng.*, vol. 115, no. 12, p. 1762, Dec. 1968.

[5] G. Costache, "Finite element method applied to skin-effect problems in strip transmission lines", *IEEE Trans. Microw. Theory Techn.*, vol. 35, no. 11, pp. 1009–1013, Nov. 1987.

[6] B. Popović and Z. Popović, "Method of determining power-frequency current distribution in cylindrical conductors", *Proc. Inst. Electr. Eng.*, vol. 119, no. 5, p. 569, May 1972.

[7] W. T. Weeks, L. L.-H. Wu, M. F. McAllister, and A. Singh, "Resistive and inductive skin effect in rectangular conductors", *IBM J. Res. Dev.*, vol. 23, no. 6, pp. 652–660, Nov. 1979.

[8] R.-B. Wu and J.-C. Yang, "Boundary integral equation formulation of skin effect problems in multiconductor transmission lines", *IEEE Trans. Magn.*, vol. 25, no. 4, pp. 3013–3015, Jul. 1989.

[9] M. Tsuk and J. Kong, "A hybrid method for the calculation of the resistance and inductance of transmission lines with arbitrary cross sections", *IEEE Trans. Microw. Theory Techn.*, vol. 39, no. 8, pp. 1338–1347, Aug. 1991.

[10] D. De Zutter and L. Knockaert, "Skin effect modeling based on a differential surface admittance operator", *IEEE Trans. Microw. Theory Techn.*, vol. 53, no. 8, pp. 2526–2538, Aug. 2005.

[11] T. Demeester and D. De Zutter, "Quasi-TM transmission line parameters of coupled lossy lines based on the Dirichlet to Neumann boundary operator", *IEEE Trans. Microw. Theory Techn.*, vol. 56, no. 7, pp. 1649–1660, Jul. 2008.

[12] A. Ruehli, "Equivalent circuit models for three-dimensional multiconductor systems", *IEEE Trans. Microw. Theory Techn.*, vol. 22, no. 3, pp. 216–221, Mar. 1974.

[13] K. Coperich, A. Ruehli, and A. Cangellaris, "Enhanced skin effect for partial-element equivalent-circuit (PEEC) models", *IEEE Trans. Microw. Theory Techn.*, vol. 48, no. 9, pp. 1435–1442, Sep. 2000.

[14] U. R. Patel, S. V. Hum, and P. Triverio, "A magneto-quasi-static surface formulation to calculate the impedance of 3D interconnects with arbitrary cross-section", in *2017 IEEE 21st Workshop on Signal and Power Integrity (SPI)*, May 2017, pp. 1–4.

[15] Y. Zhao and J. Mao, "Equivalent surface impedance-based mixed potential integral equation accelerated by optimized $\mathcal{H}$-matrix for 3-D interconnects", *IEEE Trans. Microw. Theory Techn.*, vol. 66, no. 1, pp. 22–34, Jan. 2018.

[16] M. Al-Qedra, J. Aronsson, and V. Okhmatovski, "A novel skin-effect based surface impedance formulation for broadband modeling of 3-D interconnects with electric field integral equation", *IEEE Trans. Microw. Theory Techn.*, vol. 58, no. 12, pp. 3872–3881, Dec. 2010.

[17] S. Zheng, A. Menshov, and V. Okhmatovski, "New single-source surface integral equation for magneto-quasi-static characterization of transmission lines situated in multilayered media", *IEEE Trans. Microw. Theory Techn.*, vol. 64, no. 12, pp. 4341–4351, Dec. 2016.

[18] J. Volakis, A. Chatterjee, and L. Kempel, *Finite Element Method Electromagnetics: Antennas, Microwave Circuits, and Scattering Applications*, ser. IEEE Press Series on Electromagnetic Wave Theory. Wiley, 1998.

[19] W. C. Chew, J.-M. Jin, E. Michielssen, and J. Song, *Fast and Efficient Algorithms in Computational Electromagnetics*. Artech House, 2001.

[20] J. Jin, *Theory and Computation of Electromagnetic Fields*. Wiley, 2011.

[21] A. Poggio and E. Miller, "Integral equation solutions of three-dimensional scattering problems", in *Computer Techniques for Electromagnetics*. Pergamon, 1973, ch. 4, pp. 159–264.

[22] G. Karagounis, "Hybridization of fast multipole techniques and geometrical optics for the modeling of large electromagnetic problems", PhD thesis, Ghent University, Nov. 2013.

[23] P. Silvester and R. Ferrari, *Finite Elements for Electrical Engineers*. Cambridge University Press, 1996.

[24] J. Jin, *The Finite Element Method in Electromagnetics*. Cambridge University Press, 2014.

[25] O. Zienkiewicz and R. Taylor, *The Finite Element Method: The basis*. Butterworth-Heinemann, 2000.

[26] F. L. Teixeira, "Time-domain finite-difference and finite-element methods for Maxwell equations in complex media", *IEEE Trans. Antennas Propag.*, vol. 56, no. 8, pp. 2150–2166, Aug. 2008.

[27] A. Taflove and S. Hagness, *Computational Electrodynamics: The Finite-difference Time-domain Method*. Artech House, 2005.

[28] T. Rylander, P. Ingelström, and A. Bondeson, *Computational Electromagnetics*, ser. Texts in Applied Mathematics. Springer New York, 2012.

[29] M Clemens and T. Weil, "Discrete electromagnetism with the finite integration technique", *Prog. Electromagn. Res.*, vol. 32, no. 1, pp. 65–87, Jan. 2001.

[30] A. Van Londersele, "Novel finite-difference time-domain techniques to model multiscale electromagnetic problems", PhD thesis, Ghent University, Jun. 2018.

[31] C.-T. Tai, *Dyadic Green Functions In Electromagnetic Theory*. IEEE Press, 1994.

[32] Y. Beghein, "Advanced discretization and preconditioning techniques for electromagnetic boundary integral equations", PhD thesis, Ghent University, Nov. 2015.

[33] W. Chew, M. Tong, and B. Hu, *Integral Equation Methods for Electromagnetic and Elastic Waves*. Morgan & Claypool Publishers, 2009.

[34] X. Sheng and W. Song, *Essentials of Computational Electromagnetics*. Wiley, 2012.

[35] S. Omar and D. Jiao, "A new volume integral formulation for broadband 3-D circuit extraction in inhomogeneous materials with and without external electromagnetic fields", *IEEE Trans. Microw. Theory Techn.*, vol. 61, no. 12, pp. 4302–4312, Dec. 2013.

[36] P. Nitsch, F. Gronwald, and P. Wollenberg, *Radiating Nonuniform Transmission-Line Systems and the Partial Element Equivalent Circuit Method*. Wiley, 2009.

[37] R. F. Harrington, *Field Computation by Moment Methods*. Wiley-IEEE Press, May 1993.

[38] D. Vande Ginste, "Perfectly matched layer based fast multipole methods for planar microwave structures", PhD thesis, Ghent University, Mar. 2005.

[39] S. Chakraborty and V. Jandhyala, "Evaluation of Green's function integrals in conducting media", *IEEE Trans. Antennas Propag.*, vol. 52, no. 12, pp. 3357–3363, Dec. 2004.

[40] J. Peeters, I. Bogaert, and D. De Zutter, "Calculation of MoM interaction integrals in highly conductive media", *IEEE Trans. Antennas Propag.*, vol. 60, no. 2, pp. 930–940, Feb. 2012.

[41] M. Gossye, M. Huynen, D. Vande Ginste, D. De Zutter, and H. Rogier, "A Calderón preconditioner for high dielectric contrast media", *IEEE Trans. Antennas Propag.*, vol. 66, no. 2, pp. 808–818, Feb. 2018.

[42] T. Senior and J. Volakis, *Approximate Boundary Conditions in Electromagnetics*, ser. Electromagnetics and Radar Series. Institution of Electrical Engineers, 1995.

[43] D.-S. Wang, "Limits and validity of the impedance boundary condition on penetrable surfaces", *IEEE Trans. Antennas Propag.*, vol. 35, no. 4, pp. 453–457, Apr. 1987.

[44] Z. G. Qian, W. C. Chew, and R. Suaya, "Generalized impedance boundary condition for conductor modeling in surface integral equation", *IEEE Trans. Microw. Theory Techn.*, vol. 55, no. 11, pp. 2354–2364, Nov. 2007.

[45] L. Di Rienzo, S. Yuferev, and N. Ida, "Computation of the impedance matrix of multiconductor transmission lines using high-order surface impedance boundary conditions", *IEEE Trans. Electromagn. Compat.*, vol. 50, no. 4, pp. 974–984, Nov. 2008.

[46] U. R. Patel, B. Gustavsen, and P. Triverio, "An equivalent surface current approach for the computation of the series impedance of power cables with inclusion of skin and proximity effects", *IEEE Trans. Power Del.*, vol. 28, no. 4, pp. 2474–2482, Oct. 2013.

[47] ——, "Proximity-aware calculation of cable series impedance for systems of solid and hollow conductors", *IEEE Trans. Power Del.*, vol. 29, no. 5, pp. 2101–2109, Oct. 2014.

[48] T. Demeester and D. De Zutter, "Construction of the Dirichlet to Neumann boundary operator for triangles and applications in the analysis of polygonal conductors", *IEEE Trans. Microw. Theory Techn.*, vol. 58, no. 1, pp. 116–127, Jan. 2010.

[49] H. Rogier, D. De Zutter, and L. Knockaert, "Two-dimensional transverse magnetic scattering using an exact surface admittance operator", *Radio Science*, vol. 42, no. 3, Jun. 2007.

[50] T. Demeester and D. De Zutter, "Internal impedance of composite conductors with arbitrary cross section", *IEEE Trans. Electromagn. Compat.*, vol. 51, no. 1, pp. 101–107, Feb. 2009.

[51] D. Vande Ginste, D. De Zutter, D. Deschrijver, T. Dhaene, P. Manfredi, and F. Canavero, "Stochastic modeling-based variability analysis of on-chip interconnects", *IEEE Trans. Compon. Packag. Manuf. Technol.*, vol. 2, no. 7, pp. 1182–1192, Jul. 2012.

[52] M. Chernobryvko, D. Vande Ginste, and D. De Zutter, "A two-step perturbation technique for nonuniform single and differential lines", *IEEE Trans. Microw. Theory Techn.*, vol. 61, no. 5, pp. 1758–1767, May 2013.

[53] U. R. Patel and P. Triverio, "Skin effect modeling in conductors of arbitrary shape through a surface admittance operator and the contour integral method", *IEEE Trans. Microw. Theory Techn.*, vol. 64, no. 9, pp. 2708–2717, Sep. 2016.

[54] U. R. Patel, S. Sharma, S. Yang, S. V. Hum, and P. Triverio, "Full-wave electromagnetic characterization of 3D interconnects using a surface integral formulation", in *2017 IEEE 26th Conf. Electr. Perform. Electron. Packag. Syst.*, Oct. 2017, pp. 1–3.

[55] S. Sharma, U. R. Patel, and P. Triverio, "Accelerated electromagnetic analysis of interconnects in layered media using a near-field series expansion of the Green's function", in *2018 IEEE 27th Conf. Electr. Perform. Electron. Packag. Syst.*, 2018, pp. 185–187.

[56] S. Sharma, U. R. Patel, S. V. Hum, and P. Triverio, "A complete surface integral method for broadband modeling of 3D interconnects in stratified media", *arXiv preprint arXiv:1810.04030*, pp. 1–12, 2018.

2

The Boundary Integral Equation Method for Electromagnetics

"From a long view of the history of mankind — seen from, say, ten thousand years from now — there can be little doubt that the most significant event of the 19th century will be judged as Maxwell's discovery of the laws of electrodynamics."

Richard Feynman

2.1 Maxwell's equations

Electric and magnetic manifestations have been on the mind of people for as long as recorded history exists. For the longest time, they were designated to be mysterious phenomena, often thought to be supernatural and/or superstitious. The advent of modern science sparked a renewed interest in the search for the origin of these two natural phenomena. Despite countless experiments and tremendous leaps in human understanding, however, electricity and magnetism remained two separate fields until the Danish scientist Ørsted brought to light the deflection of a compass needle by an electric current at the start of the 19th century. This jump-started the field of electromagnetism, which was explored by many famous scientist including Gauss, Ampère, Weber, Henry, Faraday just to name a few; all of whom have a scientific unit named after them.

In 1861, all this groundbreaking work was distilled into twenty equations by the Scotsman James Clerk Maxwell in his work *On Physical Lines of Force* [1], definitively unifying electricity and magnetism. This collection of equations, derived through mechanical reasoning on an equivalent material model of *molecular vortices*, was reduced to a set of four equations by Oliver Heaviside twenty years later.

Hence, the vector form of the equations, which we use up to this day, saw the light of day. Meanwhile, in 1865, in *A Dynamical Theory of the Electromagnetic Field* [2], Maxwell proved that his equations supported undulations of oscillating electric and magnetic fields and that they propagate through vacuum at the speed of light, inadvertently showing that light itself is an electromagnetic phenomenon. Experimental evidence and practical applications in the form of transmission lines followed swiftly before the turn of the century.

Maxwell's equations have proven to be remarkably general especially given the progress in physics since their conception. First it was shown that, following the *annus mirabilis* 1905, Maxwell's equations are compatible with Einstein's theory of special relativity and that the speed of light in free space is, in fact, the highest speed attainable in any frame of reference. Only with the advent of quantum electrodynamics (QED) did it become clear that the classical equations break down at extremely small distances (at photon level). Nevertheless, since their advent over a century ago, Maxwell's equations have been one of the driving forces for our modern world, (in)directly leading to a plethora of inventions such as radio, the Internet, magnetic resonance imaging (MRI), cell phones, ...

2.1.1 Frequency domain

In this work, we will work exclusively in the frequency domain. This implies that all physical quantities (such as fields, currents, etc.) $\bar{\mathbf{x}}(\mathbf{r},t)$ will be represented by their complex phasor $\mathbf{x}(\mathbf{r},\omega)$ with $\omega = 2\pi f$ the angular frequency. Both representations are linked through $\bar{\mathbf{x}}(\mathbf{r},t) = \mathrm{Re}\left[\mathbf{x}(\mathbf{r},\omega)\,e^{j\omega t}\right]$, a convention used throughout this work. Without further ado, we now present Maxwell's equations in the frequency domain:

$$\nabla \times \mathbf{e}(\mathbf{r},\omega) = -j\omega\mathbf{b}(\mathbf{r},\omega) \tag{2.1}$$

$$\nabla \times \mathbf{h}(\mathbf{r},\omega) = j\omega\mathbf{d}(\mathbf{r},\omega) + \mathbf{j}(\mathbf{r},\omega) \tag{2.2}$$

$$\nabla \cdot \mathbf{b}(\mathbf{r},\omega) = 0 \tag{2.3}$$

$$\nabla \cdot \mathbf{d}(\mathbf{r},\omega) = \rho(\mathbf{r},\omega). \tag{2.4}$$

The first two equations, the so-called curl equations, describe the relation between the electric field $\mathbf{e}$ (in V/m) and the magnetic field $\mathbf{h}$ (in A/m) on the one hand, and the magnetic induction $\mathbf{b}$ (in Wb/m^2) and electric induction $\mathbf{d}$ (in C/m^2) on the other hand, together with the (electrical) current density $\mathbf{j}$ (in A/m^2). In the frequency domain, the divergence equations (2.3) and (2.4) can be derived of the curl equations (2.1) and (2.2), respectively, by taking the divergence of both sides and, for the latter, using the law of charge conservation:

$$\nabla \cdot \mathbf{j}(\mathbf{r},\omega) + j\omega\rho(\mathbf{r},\omega) = 0, \tag{2.5}$$

with ρ the electrical charge density (in C/m^3). Conversely, (2.5) can be derived from (2.2) and (2.4).

This set of four (or five if you like) equations contains too many unknowns to results in a system with a unique solution, especially given the innate redundancy alluded to above. Therefore, additional equations are required to get a closed set of equations. These relations are enforced by the materials involved and are called the constitutive equations:

$$\mathbf{d}(\mathbf{r},\omega) = \epsilon(\mathbf{r},\omega)\,\mathbf{e}(\mathbf{r},\omega) \tag{2.6}$$

$$\mathbf{b}(\mathbf{r},\omega) = \mu(\mathbf{r},\omega)\,\mathbf{h}(\mathbf{r},\omega), \tag{2.7}$$

where ϵ and μ are the permittivity and permeability of the medium, respectively. Note that these relations are macroscopic simplifications of the complex, microscopic reality. In particular, (2.6)–(2.7) describe local, linear, isotropic, but possibly dispersive and inhomogeneous materials. Although more comprehensive relations can be employed to describe, amongst others, crystals and ferromagnetic materials, in this dissertation the considered media are piecewise homogeneous, implying that permittivity and permeability are location independent, other than a discrete number of jumps. This leads to the following definition of the propagation speed, wavenumber and wave impedance

$$c(\omega) = 1/\sqrt{\epsilon(\omega)\,\mu(\omega)} \tag{2.8}$$

$$k(\omega) = \omega\sqrt{\epsilon(\omega)\,\mu(\omega)} \tag{2.9}$$

$$Z_c(\omega) = \sqrt{\mu(\omega)/\epsilon(\omega)}. \tag{2.10}$$

This leaves the $\mathbf{j}$ term in (2.2) to be dealt with. Several contributions can make up the total current density. One of those is the conduction current in a conductor, defined as $\mathbf{j}_c = \sigma\mathbf{e}$. Throughout this dissertation, the conductivity σ is allowed for by merging it with the (possibly already) complex permittivity to obtain a generalized permittivity

$$\tilde{\epsilon} = \epsilon + \frac{\sigma}{j\omega}, \tag{2.11}$$

where the tilde is customarily assumed and hence, suppressed, in the rest of this work. The remaining contributions to $\mathbf{j}$ are usually external, assumed to be known, and often denoted as $\mathbf{j}_e$. By means of (2.5), the same applies to the charge density ρ_e.

A perfect electric conductor (PEC) is a hypothetical material for which the electrical conductivity is infinite. Despite not existing in nature, conductors are regularly replaced by PECs in calculations/simulations to simplify matters as the approximation is reasonable at high frequencies.

Good (but non-perfect) conductors are defined as materials for which $\sigma \gg \omega\epsilon$ and are often characterized by a different metric, i.e., the skin depth, defined as

$$\delta = \sqrt{2/\omega\mu\sigma}. \tag{2.12}$$

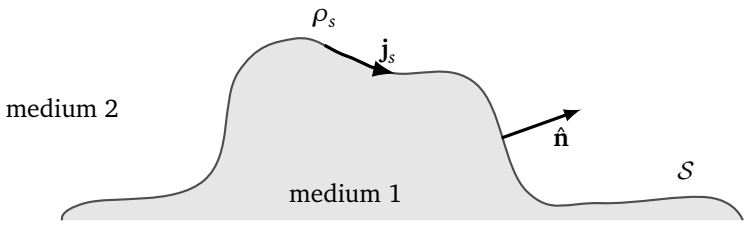

Figure 2.1: Relevant illustration for the definition of (2.15)–(2.18).

This is the distance over which a wave propagating through the material sees its amplitude decreased by a factor e. The skin depth crops up in the approximate expressions of the wavenumber and wave impedance of this class of materials:

$$k = \omega\sqrt{\epsilon\mu} \approx (1-j)/\delta \tag{2.13}$$

$$Z_c \approx (1+j)/\sigma\delta. \tag{2.14}$$

2.1.2 Boundary conditions

At the boundaries of different media, Maxwell's equations (2.1)–(2.4) have to be complemented with boundary conditions that describe the possible jumps of the field quantities and their derivatives. Given the conventions depicted in Fig. 2.1, these conditions on the surface $\mathcal{S}$ are

$$\hat{\mathbf{n}} \times (\mathbf{e}_2 - \mathbf{e}_1) = \mathbf{0} \tag{2.15}$$

$$\hat{\mathbf{n}} \times (\mathbf{h}_2 - \mathbf{h}_1) = \mathbf{j}_s \tag{2.16}$$

$$\hat{\mathbf{n}} \cdot (\mathbf{b}_2 - \mathbf{b}_1) = \mathbf{0} \tag{2.17}$$

$$\hat{\mathbf{n}} \cdot (\mathbf{d}_2 - \mathbf{d}_1) = \rho_s, \tag{2.18}$$

with $\mathbf{j}_s$ the surface current density (in A/m), ρ_s the surface charge density (in C/m^2) and $\hat{\mathbf{n}}$ the unit normal vector pointing from medium 1 into medium 2. These boundary equations are valid if one of the media is a PEC as well, albeit that all field quantities inside the medium vanish as no fields are supported in the bulk of a PEC.

2.1.3 Wave equation

Substituting the constitutive equations (2.6)–(2.7) into the curl equations (2.1)–(2.2), results in a pair of coupled first order differential equations. Taking the curl of (2.1) and substituting (2.2) into the result, leaves only the electric field quantity, described by a second-order differential equations [3]:

$$\nabla^2\mathbf{e} + k^2\mathbf{e} = j\omega\mu\mathbf{j}_e + \nabla\rho_e/\epsilon. \tag{2.19}$$

This partial differential equation has taken the form of a (vector) Helmholtz equation, unequivocally exhibiting the wave character of the electric field. A similar procedure yields the same type of differential equation for the magnetic field,

$$\nabla^2\mathbf{h} + k^2\mathbf{h} = -\nabla \times \mathbf{j}_e. \tag{2.20}$$

2.1.4 Electromagnetic potentials

Solving (2.19) can prove to be cumbersome due to the $\nabla\rho_e$ term in the right-hand side as this tends to lead to hypersingular integrals. Therefore, it turns out to be advantageous to express the unknown field quantities in terms of electromagnetic potentials first and use these to obtain a set of equations that is easier to solve. To this end, $\mathbf{e}$ and $\mathbf{h}$ will be decomposed according to Helmholtz's theorem.

Eq. (2.3) states that $\mathbf{b}$ is solenoidal and implies that it can be fully described as the curl of a vector potential $\mathbf{a}$:

$$\mathbf{b} = \nabla \times \mathbf{a}. \tag{2.21}$$

Substituting this relation into (2.1), reveals that $\mathbf{e} + j\omega\mathbf{a}$ is irrotational and can thus be characterized by the gradient of a scalar potential ϕ, yielding

$$\mathbf{e} = -j\omega\mathbf{a} - \nabla\phi. \tag{2.22}$$

As this set of potentials $\mathbf{a}$ and ϕ is not uniquely defined, an extra condition can be enforced to exploit this degree of freedom. Various possibilities exist but here the Lorenz gauge [4] will be employed, which for an isotropic, homogeneous medium is defined as:

$$\nabla \cdot \mathbf{a} + j\omega\epsilon\mu\phi = 0. \tag{2.23}$$

Substituting (2.21)–(2.22) into Maxwell's equation and applying (2.23), results in the following wave equations for the potentials:

$$\nabla^2\mathbf{a} + k^2\mathbf{a} = -\mu\mathbf{j}_e \tag{2.24}$$

$$\nabla^2\phi + k^2\phi = -\rho_e/\epsilon. \tag{2.25}$$

After solving these (easier) wave equations, the fields can be reconstructed through (2.21)–(2.22).

2.1.5 Green's function

A universal solution to the scalar and/or vector Helmholtz equation does not exist for an arbitrary source. However, given the linearity of the system, a solution can be constructed through superposition of *simpler* source terms. A general approach,

Figure 2.2: Image theory applied to the calculation of the Green's function in a half-space.

analogous to the impulse response in system theory, is to solve the Helmholtz equation for a single source point [5]:

$$\nabla^2 G(r) + k^2 G(r) = -\delta(r), \tag{2.26}$$

with $\delta(r)$ the Dirac delta function. The solution to this equation is called the *Green's function*. In order to obtain a unique solution that physically represents an outgoing wave, the function is subjected to the Sommerfeld radiation condition [6], which in three-dimensional (3-D) space is defined as

$$\lim_{r\to\infty} r\left(\frac{\partial G}{\partial r} + jkG\right) = 0. \tag{2.27}$$

In a 3-D homogeneous background medium this results in the following Green's function

$$G(r) = \frac{e^{-jkr}}{4\pi r}. \tag{2.28}$$

In interconnect modeling, the so-called (quasi-)static approximation is often employed as the electrical length of the connections is very small. In such cases, an approximation of the Green's function is utilized: $G(r) = 1/4\pi r$.

In case there is an infinite PEC plane present, the Green's function in the half-space above the PEC plane can still be expressed analytically through image theory (see Fig. 2.2) as

$$G_{\text{half}}\left(\mathbf{r}|\mathbf{r}'\right) = G\left(|\mathbf{r}-\mathbf{r}'|\right) \pm G\left(|\mathbf{r}-\mathbf{r}''|\right) = \frac{e^{-jkR}}{4\pi R} \pm \frac{e^{-jkR'}}{4\pi R'}, \tag{2.29}$$

with $\mathbf{r}''$ the mirror image of $\mathbf{r}'$, $R = |\mathbf{r}-\mathbf{r}'|$ and $R' = |\mathbf{r}-\mathbf{r}''|$. The minus sign must be chosen for the field components that are zero on the PEC plane. The plus sign pertains to field components whose normal derivatives vanish on the PEC plane. For other background media, such as the very prevalent layered or stratified medium, the expressions for the Green's function become much less straightforward [7], [8] and usually involves computationally expensive numerical integration and/or slowly convergent series.

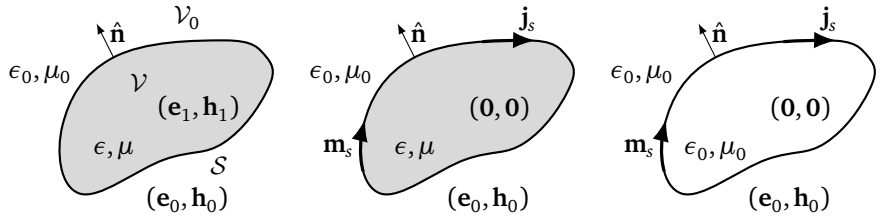

(a) Original situation. (b) Love's equivalence theorem. (c) Equivalent situation.

Figure 2.3: Illustration of the equivalence theorem.

2.1.6 Equivalence principle

To avoid convoluted and complex Green's function calculations, the equivalence theorem is widely utilized to transform a given situation into an equivalent, ideally easier to solve problem [3], [9]. Several different flavors of the equivalence principle exist, but only one will be elucidated here, viz., Love's theorem [10].

Consider the situation shown in Fig. 2.3(a). A volume $\mathcal{V}$ with boundary surface $\mathcal{S}$ and filled with a material (ϵ, μ) is embedded in a background medium $\mathcal{V}_0$, characterized by (ϵ_0, μ_0) (not necessarily free space). The fields inside $\mathcal{V}$ are denoted as $(\mathbf{e}_1, \mathbf{h}_1)$ while outside, they are given as $(\mathbf{e}_0, \mathbf{h}_0)$. Love's equivalence theorem states that the fields inside the volume can be made to vanish while leaving the outside field distributions untouched by introducing an electric $\mathbf{j}_s$ and magnetic $\mathbf{m}_s$ surface current density on $\mathcal{S}$ (shown in Fig. 2.3(b)). Applying boundary conditions (2.15)–(2.18) in both Fig. 2.3(a) and Fig. 2.3(b) yields, by comparison, the following expressions for the equivalent surface current densities:

$$\mathbf{j}_s = \hat{\mathbf{n}} \times \mathbf{h}_0 = \hat{\mathbf{n}} \times \mathbf{h}_1 \tag{2.30}$$

$$\mathbf{m}_s = -\hat{\mathbf{n}} \times \mathbf{e}_0 = -\hat{\mathbf{n}} \times \mathbf{e}_1, \tag{2.31}$$

with the tangential fields taken on $\mathcal{S}$ [1]. Without any fields inside $\mathcal{V}$, any changes to the material parameters will not influence $(\mathbf{e}_0, \mathbf{h}_0)$. The inside material can thus, for example, be replaced by the background medium to obtain the equivalent configuration of Fig. 2.3(c). Since the material discontinuity has been replaced by the equivalent surface currents, it is (generally) easier to find a suitable Green's function (in this case the free space Green's function (2.28)).

[1] Note that for the description of Love's equivalence theorem, we tacitly added magnetic current and charge densities to the right-hand side of (2.1) and (2.3), respectively, as well as magnetic surface current and surface charge densities to (2.15) and (2.17), respectively. Although the existence of such physical quantities has not been proven, they allow for elegant formulations and solution to a number of problems of great practical interest.

2.1.7 Eigenfunctions

In Section 2.1.5, the Helmholtz equation was solved for a fundamental excitation. Interestingly, the homogeneous variants of the wave equations (2.19)–(2.20), i.e., without any sources, exhibit nonzero solutions under certain boundary conditions. These so-called *eigenfuctions* will be discussed here for the specific case of a (singly bounded and simply connected) volume $\mathcal{V}$ with a PEC boundary surface $\mathcal{S}$. The discussion largely follows [5], [11][2].

The electric field eigenvectors fall apart into two separate sets: irrotational and solenoidal/divergenceless functions. The first set is defined as $\mathbf{f}_\nu = \nabla\phi_\nu$ with ϕ_ν subjected to

$$\nabla^2\phi_\nu + \lambda_\nu^2\phi_\nu = 0 \qquad \text{in } \mathcal{V} \tag{2.32}$$
$$\phi_\nu = 0 \qquad \text{on } \mathcal{S}, \tag{2.33}$$

with ν a triple index. The solenoidal eigenmodes $\mathbf{e}_\nu$ satisfy

$$\nabla\times\nabla\times\mathbf{e}_\nu - k_\nu^2\mathbf{e}_\nu = \mathbf{0} \qquad \text{in } \mathcal{V} \tag{2.34}$$
$$\hat{\mathbf{n}}\times\mathbf{e}_\nu = \mathbf{0} \qquad \text{on } \mathcal{S}. \tag{2.35}$$

The eigenvectors for the magnetic field can be split into two sets as well. The irrotational vectors are $\mathbf{g}_\nu = \nabla\psi_\nu$ where ψ_ν satisfies

$$\nabla^2\psi_\nu + \mu_\nu^2\psi_\nu = 0 \qquad \text{in } \mathcal{V} \tag{2.36}$$
$$\hat{\mathbf{n}}\cdot\nabla\psi_\nu = 0 \qquad \text{on } \mathcal{S}. \tag{2.37}$$

The solenoidal eigenmodes $\mathbf{h}_\nu$, on the other hand, comply with

$$\nabla\times\nabla\times\mathbf{h}_\nu - k_\nu^2\mathbf{h}_\nu = \mathbf{0} \qquad \text{in } \mathcal{V} \tag{2.38}$$
$$\hat{\mathbf{n}}\times\nabla\times\mathbf{h}_\nu = \mathbf{0} \qquad \text{on } \mathcal{S}. \tag{2.39}$$

Remark that the wavenumber/eigenvalue of the solenoidal eigenfunctions for both fields are the same for every value of ν. This is a consequence of the fact that $\nabla\times\mathbf{h}_\nu$ is a potential electric eigenvector and vice versa. Moreover, the eigenvectors can be normalized such that

$$k_\nu\mathbf{e}_\nu = \nabla\times\mathbf{h}_\nu \qquad \text{and} \qquad k_\nu\mathbf{h}_\nu = \nabla\times\mathbf{e}_\nu. \tag{2.40}$$

The wavenumbers of the eigenmodes, i.e., $k_\nu, \lambda_\nu, \mu_\nu$, are always real. The eigenmodes themselves can be chosen to be real as well, but through linear combinations can also be represented in some cases as complex functions.

[2]Note that other notations and conventions are used as well. One such example are Hansen's vector wave functions **L**, **M** and **N**, which reduce to the functions presented here when constrained to the same boundary conditions [12].

These two sets of eigenmodes are complete and thus suffice to construct all conceivable valid field distributions inside the cavity. Care has to be taken for special volumes (non singly bounded or non simply connected) such as two concentric spheres or a cylindrical shell as these require an additional eigenmode to fully capture the static behavior [11].

2.2 The boundary integral equation method

Boundary integral equations (BIEs), of which a high-level overview was presented in Section 1.3.3, will be used throughout this work to tackle computational electromagnetics (CEM) problems. In this section, the boundary element method (BEM) will be introduced for PEC objects. Moreover, the discretization procedure to transform the (continuous) integral equation into a (discrete) matrix equation will be discussed along with strategies to deal with the numerical evaluation of singular integrals.

2.2.1 Mixed potential integral equation

Consider once more the situation of Fig. 2.3(a), but specifically with the material inside $\mathcal{V}$ being a PEC. This implies two main changes from the general case. First of all, no fields are supported in its bulk, so $(\mathbf{e}_1, \mathbf{h}_1)$ vanish. Furthermore, an electric surface current density $\mathbf{j}_s$ on $\mathcal{S}$ will be induced by the fields in $\mathcal{V}_0$ to enforce the corresponding boundary conditions on $\mathcal{S}$. Careful comparison to Fig. 2.3(b) reveals that both situations are the same except for the absence of the magnetic current density $\mathbf{m}_s$, which is not supported by the PEC. It is thus as if Love's theorem is automatically applied by the PEC. Consequently, the PEC can simply be removed and replaced by the induced $\mathbf{j}_s$ without altering the outside environment, leading to a geometry as shown in Fig. 2.3(c).

Let us now split up the total electric (and magnetic) field $\mathbf{e}_0$ into two contributions: $\mathbf{e}_{\text{inc}}$, the incident field generated by sources inside $\mathcal{V}_0$ as if the PEC was never there in the first place, and $\mathbf{e}_{\text{sc}}$, the scattered field excited by $\mathbf{j}_s$ in absence of the sources. The incident field is assumed to be the source term for the posed problem and so is known upfront. The scattered field, on the other hand, is generated by the surface current density and can thus be found by solving (2.19). Yet, as detailed in Section 2.1.4, it is advantageous to express $\mathbf{e}_{\text{sc}}$ in terms of potentials, leading to the following expression for the scattered field, through superposition:

$$\mathbf{e}_{\text{sc}} = -j\omega\mu_0 \int_{\mathcal{S}} G\left(|\mathbf{r}-\mathbf{r}'|\right) \mathbf{j}_s\left(\mathbf{r}'\right) \mathrm{d}\mathbf{r}' + \frac{1}{j\omega\epsilon_0} \nabla \int_{\mathcal{S}} G\left(|\mathbf{r}-\mathbf{r}'|\right) \nabla' \cdot \mathbf{j}_s\left(\mathbf{r}'\right) \mathrm{d}\mathbf{r}', \quad (2.41)$$

where (2.5) was employed to relate $\mathbf{j}_s$ and ρ_s. The first term is the contribution to the electric field by the vector potential $\mathbf{a}$, while the second term corresponds to the scalar potential ϕ, hence the name mixed potential integral equation (MPIE).

At this point, the boundary condition on the tangential electric field (2.15) is applied on $\mathcal{S}$, i.e.,

$$\hat{\mathbf{n}} \times \mathbf{e}_0 = \hat{\mathbf{n}} \times (\mathbf{e}_{\text{inc}} + \mathbf{e}_{\text{sc}}) = 0. \tag{2.42}$$

Inserting (2.41) leads to the electric field integral equation (EFIE)

$$\begin{aligned} \hat{\mathbf{n}} \times \mathbf{e}_{\text{inc}} = -Z_c \mathcal{T} \mathbf{j}_s = j\omega\mu_0 \hat{\mathbf{n}} \times \int_{\mathcal{S}} G\left(|\mathbf{r}-\mathbf{r}'|\right) \mathbf{j}_s\left(\mathbf{r}'\right) \mathrm{d}\mathbf{r}' \\ -\frac{1}{j\omega\epsilon_0} \hat{\mathbf{n}} \times \nabla \int_{\mathcal{S}} G\left(|\mathbf{r}-\mathbf{r}'|\right) \nabla' \cdot \mathbf{j}_s\left(\mathbf{r}'\right) \mathrm{d}\mathbf{r}', \end{aligned} \tag{2.43}$$

with $\mathcal{T}$ the EFIE operator.

2.2.2 Method of Moments

Solving (2.43) analytically only succeeds in a handful of very simple geometries, e.g., an infinite (PEC) plane, an infinite cylinder or a sphere. For arbitrary surfaces numerical approximations are necessary to find an expression for $\mathbf{j}_s$. The most widely used method to tackle this problem is the BEM, which is often called Method of Moments (MoM) in the field of electromagnetics [13]. The general idea of the MoM is to approximate the boundaries by a surface mesh consisting of simple shapes. Subsequently, the unknown quantities (for the EFIE the surface current density $\mathbf{j}_s$) are expanded into elementary functions, defined over the mesh. By testing the result, the integral equation is transformed into a matrix equation, which is then solved using an appropriate matrix solver.

The surface mesh is usually constructed out of triangles (see for example Fig. 2.4). Delaunay triangulation forms the basis for meshing algorithms as it provides a set of regular triangles, i.e., without very sharp corners. However, for constrained two-dimensional (2-D) problems and non-flat surfaces, Delaunay triangulation does not guarantee a (unique) solution and heuristics have to be applied [14], [15]. Other shapes are sometimes used as well. Rectangles, or more generally quadrilaterals, are employed to reduce the number of unknowns but are overall less suited for general mesh programs as they are less flexible than triangular meshes. Curvilinear elements can be used for a more efficient representation of curved objects and shapes.

With every edge e_j in the surface mesh, a basis function is associated. For the omnipresent triangular meshes, the most widespread basis functions $\mathbf{f}_j(\mathbf{r})$ are the so-called Rao-Wilton-Glisson (RWG) functions [16] defined on pairs of adjacent triangles (see Fig. 2.5(a)):

$$\mathbf{f}_j(\mathbf{r}) = \begin{cases} \left(\mathbf{r}-\mathbf{r}_j^+\right)/2A_j^+, & \text{if } \mathbf{r} \in \mathrm{T}_j^+ \\ \left(\mathbf{r}_j^- - \mathbf{r}\right)/2A_j^-, & \text{if } \mathbf{r} \in \mathrm{T}_j^- \\ 0, & \text{elsewhere} \end{cases} \tag{2.44}$$

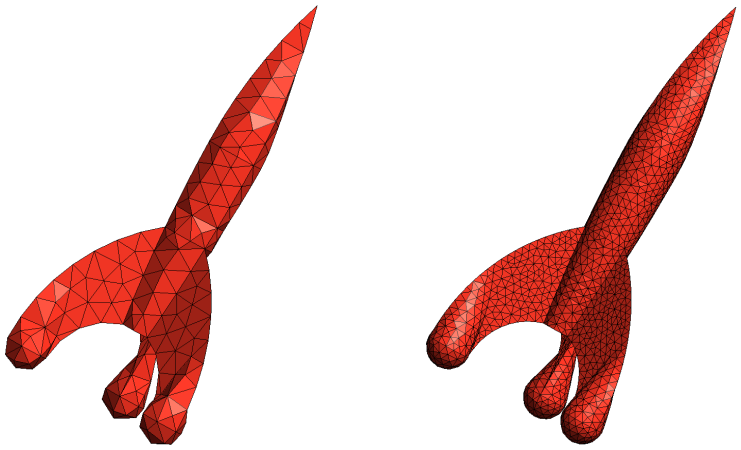

(a) Coarse surface mesh. (b) Fine surface mesh.

Figure 2.4: Illustration of a triangular surface mesh of a rocket, generated with gmsh [14].

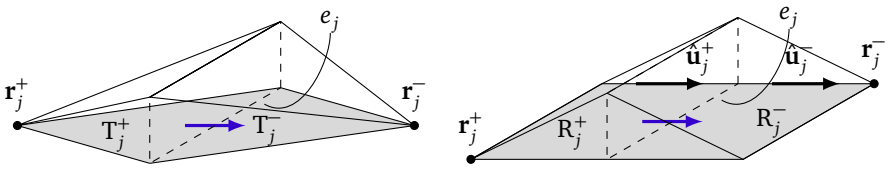

(a) RWG basis function $\mathbf{f}_j(\mathbf{r})$ defined over triangles T_j^+ and T_j^+. (b) Rooftop basis function $\mathbf{f}_j(\mathbf{r})$ defined over rectangles R_j^+ and R_j^+.

Figure 2.5: Basis functions defined over a pair of adjacent faces with common edge e_j.

with $A_j^\pm$ the area of the respective triangles $\mathrm{T}_j^\pm$ and $\mathbf{r}_j^\pm$ the *anchor* point of the RWG, i.e., the vertex opposite of the common edge e_j. An RWG function represents a current flowing from one triangle to another, perpendicularly to their common edge and tangential to the other edges.

The equivalent function on adjacent rectangles are the rooftop functions, shown in Fig. 2.5(b), generally defined as

$$\mathbf{f}_j(\mathbf{r}) = \begin{cases} \left[(\mathbf{r}-\mathbf{r}_j^+)\cdot\mathbf{u}_j^+\right]\hat{\mathbf{u}}_j^+/A_j^+, & \text{if } \mathbf{r}\in\mathrm{R}_j^+ \\ \left[(\mathbf{r}_j^- -\mathbf{r})\cdot\mathbf{u}_j^-\right]\hat{\mathbf{u}}_j^-/A_j^-, & \text{if } \mathbf{r}\in\mathrm{R}_j^- \\ 0, & \text{elsewhere} \end{cases} \tag{2.45}$$

with $A_j^\pm$ the area of the respective rectangles $\mathrm{R}_j^\pm$.

On other surface meshes, similar, linear functions can be defined. Additionally,

higher-order basis functions, which expand upon, e.g., the RWG functions, can also be constructed [17], [18], but they have not such a widespread use in the BEM, in contrast to volumetric methods such as the finite element method (FEM).

Regardless of the chosen set of functions, the next step constitutes the approximation of $\mathbf{j}_s$ on $\mathcal{S}$ in terms of these local basis functions

$$\mathbf{j}_s = \sum_{j=1}^{N} I_j \mathbf{f}_j(\mathbf{r}), \tag{2.46}$$

with N the number of edges and thus employed basis functions. This expansion is inserted in (2.43). In order to fully transform the resulting equation into a matrix equation, both sides of the EFIE are weighted utilizing a suitable inner product and an appropriate set of test functions $\mathbf{t}(\mathbf{r})$. A very common approach uses the (rotated version of the) same functions as the basis of the expansion, i.e., $\mathbf{t} = \hat{\mathbf{n}} \times \mathbf{f}$ and is called the *Galerkin* technique. The inner product is defined as

$$\langle \mathbf{a}(\mathbf{r}), \mathbf{b}(\mathbf{r}) \rangle = \int_{\mathcal{S}} \mathbf{a}(\mathbf{r}) \cdot \mathbf{b}(\mathbf{r}) \, \mathrm{d}S \tag{2.47}$$

with $\mathcal{S}$ the common support of the functions involved. This procedure transforms the EFIE into

$$\int_{\mathcal{S}_i} \mathbf{f}_i(\mathbf{r}) \cdot \mathbf{e}^t_{\mathrm{inc}}(\mathbf{r}) \, \mathrm{d}S = \sum_{j=1}^{N} I_j \left[j\omega\mu_0 \int_{\mathcal{S}_i} \int_{\mathcal{S}_j} G\left(|\mathbf{r}-\mathbf{r}'|\right) \mathbf{f}_i(\mathbf{r}) \cdot \mathbf{f}_j\left(\mathbf{r}'\right) \mathrm{d}S' \, \mathrm{d}S \right. \tag{2.48}$$
$$\left. - \frac{1}{j\omega\epsilon_0} \int_{\mathcal{S}_i} \mathbf{f}_i(\mathbf{r}) \cdot \nabla \int_{\mathcal{S}_j} G\left(|\mathbf{r}-\mathbf{r}'|\right) \nabla' \cdot \mathbf{f}_j\left(\mathbf{r}'\right) \mathrm{d}S' \, \mathrm{d}S \right],$$

with the superscript t denoting tangential to the surface and $\mathcal{S}_i$ the support of function $\mathbf{f}_i$. Remark that the divergence of the presented basis functions is well-defined and evaluates to a constant value on either of its support faces. This type of basis functions is therefore called divergence-conforming. The gradient of the inner integral in the second term on the right-hand side can be transferred to the testing function $\mathbf{f}_i$ through the appropriate vector properties and Gauss' theorem to yield

$$\int_{\mathcal{S}_i} \mathbf{f}_i(\mathbf{r}) \cdot \mathbf{e}^t_{\mathrm{inc}}(\mathbf{r}) \, \mathrm{d}S = \sum_{j=1}^{N} I_j \left[j\omega\mu_0 \int_{\mathcal{S}_i} \int_{\mathcal{S}_j} G\left(|\mathbf{r}-\mathbf{r}'|\right) \mathbf{f}_i(\mathbf{r}) \cdot \mathbf{f}_j\left(\mathbf{r}'\right) \mathrm{d}S' \, \mathrm{d}S \right. \tag{2.49}$$
$$\left. + \frac{1}{j\omega\epsilon_0} \int_{\mathcal{S}_i} \int_{\mathcal{S}_j} G\left(|\mathbf{r}-\mathbf{r}'|\right) \nabla \cdot \mathbf{f}_i(\mathbf{r}) \nabla' \cdot \mathbf{f}_j\left(\mathbf{r}'\right) \mathrm{d}S' \, \mathrm{d}S \right].$$

In compact notation this discretized EFIE reads

$$\mathbf{P} = \overline{\overline{Z}}\,\mathbf{I}, \tag{2.50}$$

with the elements of the vectors $\mathbf{P}$, $\mathbf{I}$ and the matrix $\overline{\overline{Z}}$ given by

$$\mathbf{p}_i = \int_{\mathcal{S}_i} \mathbf{f}_i(\mathbf{r}) \cdot \mathbf{e}^t_{\text{inc}}(\mathbf{r})\, \mathrm{d}S \tag{2.51}$$

$$\mathbf{I}_j = I_j \tag{2.52}$$

$$\begin{aligned} \overline{\overline{Z}}_{ij} = \quad & j\omega\mu_0 \int_{\mathcal{S}_i}\int_{\mathcal{S}_j} G\left(|\mathbf{r}-\mathbf{r}'|\right) \mathbf{f}_i(\mathbf{r}) \cdot \mathbf{f}_j\left(\mathbf{r}'\right) \mathrm{d}S'\, \mathrm{d}S \\ & + \frac{1}{j\omega\epsilon_0} \int_{\mathcal{S}_i}\int_{\mathcal{S}_j} G\left(|\mathbf{r}-\mathbf{r}'|\right) \nabla\cdot\mathbf{f}_i(\mathbf{r})\, \nabla'\cdot\mathbf{f}_j\left(\mathbf{r}'\right) \mathrm{d}S'\, \mathrm{d}S \end{aligned} \quad . \tag{2.53}$$

This matrix equation can be solved either directly or iteratively. The resulting coefficients $\mathbf{I}_j$ can then be employed to reconstruct $\mathbf{j}_s$ and to calculate the scattered fields anywhere through (2.41). Notwithstanding the local nature of the basis functions, the matrix $\overline{\overline{Z}}$ is not sparse; on the contrary, it will be dense. This is a result of the Green's function in the integrals required to calculate the matrix elements, which has a global reach.

2.2.3 Singular integrals

The elements of the interaction matrix, as defined in (2.53), involve two surface integrals over pairs of faces. Unfortunately, no analytical formulas exist for their evaluation and one has to turn to numerical integration techniques such as, e.g., Gaussian quadrature [19] to solve the four-dimensional integrals. At this point, however, an additional problem rears its head. The integrand of both contributions becomes singular when the supports $\mathcal{S}_i$ and $\mathcal{S}_j$ overlap or touch. Generally speaking, two approaches to tackle this inconvenience are in use. Singularity extraction splits the integrand into a singular and non-singular part. The first integral is then calculated analytically while the remaining, regularized term is evaluated numerically using any appropriate technique [20]–[24]. The second type of technique introduces a substitution of variables in the inner double integral over one face to obtain a Jacobian that cancels out the singularity. The resulting set of integrals is non-singular and can be solved by conventional methods [25]–[29].

References

[1] J. C. Maxwell, "On physical lines of force", *Philos. Mag.*, vol. 90, Feb. 1861.

[2] ——, "A dynamical theory of the electromagnetic field", *Philos. Trans. R. Soc. London*, vol. 155, no. 1, pp. 459–512, Jan. 1865.

[3] C. Balanis, *Advanced Engineering Electromagnetics, 2nd Edition*. Wiley, 2012.

[4] J. G. Van Bladel, "Lorenz or Lorentz?", *IEEE Antennas Propag. Mag.*, vol. 33, no. 2, pp. 69–69, Apr. 1991.

[5] ——, *Electromagnetic Fields*. John Wiley & Sons, Inc., May 2007.

[6] A. Sommerfeld, *Partial Differential Equations in Physics*. Academic Press, 1949.

[7] C.-T. Tai, *Dyadic Green Functions In Electromagnetic Theory*. IEEE Press, 1994.

[8] A. Alparslan, M. Aksun, and K. Michalski, "Closed-form Green's functions in planar layered media for all ranges and materials", *IEEE Trans. Microw. Theory Techn.*, vol. 58, no. 3, pp. 602–613, Mar. 2010.

[9] R. F. Harrington, *Time-Harmonic Electromagnetic Fields*. Wiley-IEEE Press, Sep. 2001.

[10] A. E. H. Love, "The integration of the equations of propagation of electric waves", *Philos. Trans. Royal Soc. A*, vol. 197, no. 287-299, pp. 1–45, Jan. 1901.

[11] K. Kurokawa, "The expansions of electromagnetic fields in cavities", *IRE Trans. Microw. Theory Tech.*, vol. 6, no. 2, pp. 178–187, Apr. 1958.

[12] T. B. A. Senior, "A note on Hansen's vector wave functions", *Can. J. Phys.*, vol. 38, no. 12, pp. 1702–1705, Dec. 1960.

[13] R. F. Harrington, *Field Computation by Moment Methods*. Wiley-IEEE Press, May 1993.

[14] C. Geuzaine and J.-F. Remacle, "Gmsh: A 3-D finite element mesh generator with built-in pre- and post-processing facilities", *Int. J. Numer. Methods Eng.*, vol. 79, no. 11, pp. 1309–1331, Sep. 2009.

[15] P.-O. Persson and G. Strang, "A simple mesh generator in MATLAB", *SIAM Rev.*, vol. 46, no. 2, pp. 329–345, Jan. 2004.

[16] S. Rao, D. Wilton, and A. Glisson, "Electromagnetic scattering by surfaces of arbitrary shape", *IEEE Trans. Antennas Propag.*, vol. 30, no. 3, pp. 409–418, May 1982.

[17] M. Djordjević and B. Notaroš, "Double higher order Method of Moments for surface integral equation modeling of metallic and dielectric antennas and scatterers", *IEEE Trans. Antennas Propag.*, vol. 52, no. 8, pp. 2118–2129, Aug. 2004.

[18] W. Ding and G. Wang, "Treatment of singular integrals on generalized curvilinear parametric quadrilaterals in higher order method of moments", *IEEE Antennas Wireless Propag. Lett.*, vol. 8, no. 2, pp. 1310–1313, Dec. 2009.

[19] M. Abramowitz and I. A. Stegun, *Handbook of Mathematical Functions: With Formulas, Graphs, and Mathematical Tables*. National Bureau of Standards, 1964.

[20] D. R. Wilton, S. Rao, A. Glisson, D. Schaubert, O. Al-Bundak, and C. Butler, "Potential integrals for uniform and linear source distributions on polygonal and polyhedral domains", *IEEE Trans. Antennas Propag.*, vol. 32, no. 3, pp. 276–281, Mar. 1984.

[21] R. D. Graglia, "On the numerical integration of the linear shape functions times the 3-D Green's function or its gradient on a plane triangle", *IEEE Trans. Antennas Propag.*, vol. 41, no. 10, pp. 1448–1455, 1993.

[22] P. Arcioni, M. Bressan, and L. Perregrini, "On the evaluation of the double surface integrals arising in the application of the boundary integral method to 3-D problems", *IEEE Trans. Microw. Theory Techn.*, vol. 45, no. 3, pp. 436–439, Mar. 1997.

[23] P. Ylä-Oijala and M. Taskinen, "Calculation of CFIE impedance matrix elements with RWG and n x RWG functions", *IEEE Trans. Antennas Propag.*, vol. 51, no. 8, pp. 1837–1846, Aug. 2003.

[24] I. Hänninen, M. Taskinen, and J. Sarvas, "Singularity subtraction integral formulae for surface integral equations with RWG, rooftop and hybrid basis functions", *Prog. Electromagn. Res.*, vol. 63, pp. 243–278, 2006.

[25] M. G. Duffy, "Quadrature over a pyramid or cube of integrands with a singularity at a vertex", *SIAM J. Numer. Anal.*, vol. 19, no. 6, pp. 1260–1262, Dec. 1982.

[26] L. Rossi and P. J. Cullen, "On the fully numerical evaluation of the linear-shape function times the 3-D Green's function on a plane triangle", *IEEE Trans. Microw. Theory Techn.*, vol. 47, no. 4, pp. 398–402, 1999.

[27] M. Khayat and D. R. Wilton, "Numerical evaluation of singular and near-singular potential integrals", *IEEE Trans. Antennas Propag.*, vol. 53, no. 10, pp. 3180–3190, Oct. 2005.

[28] A. G. Polimeridis, F. Vipiana, J. R. Mosig, and D. R. Wilton, "DIRECTFN: Fully numerical algorithms for high precision computation of singular integrals in Galerkin SIE methods", *IEEE Trans. Antennas Propag.*, vol. 61, no. 6, pp. 3112–3122, Jun. 2013.

[29] A. A. Tambova, M. S. Litsarev, G. Guryev, and A. G. Polimeridis, “On the generalization of DIRECTFN for singular integrals over quadrilateral patches”, *IEEE Trans. Antennas Propag.*, vol. 66, no. 1, pp. 304–314, Jan. 2018.

3

The Differential Surface Admittance Operator

"Call it magic, call it true."

Coldplay

★ ★ ★

In this chapter, we introduce the general concept of the differential surface admittance operator in 3-D space and a specific formulation of this operator based on the eigenmodes of the volume under consideration. First, in Section 3.1, we introduce a variant of the electromagnetic equivalence theorem which only involves a single electrical equivalent current. In Section 3.2, for the case of a nonmagnetic material, we determine an expression for this unknown surface current density based on the eigenmodes of a cavity with the same shape as the volume under consideration. An alternative derivation of the same formula is proposed in Section 3.3. This reasoning is based on the general theory of resonators.

3.1 Introduction

In the previous chapter, more specifically in Section 2.1.6, we introduced the equivalence principle through Love's theorem. By imposing both an electrical and magnetic surface current density on the boundary surface $\mathcal{S}$, the fields inside (or outside) the bounded volume $\mathcal{V}$ were made to vanish. This condition is, however, quite strict. If one is only interested in preserving the outside field distributions

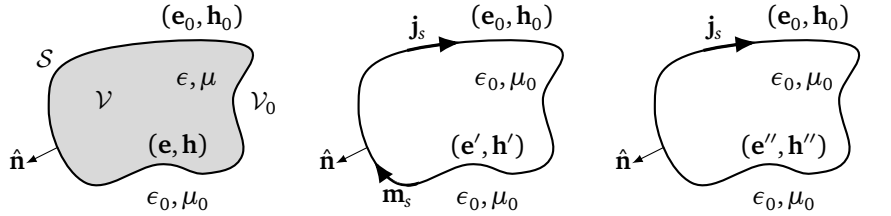

(a) Original situation. (b) General equivalence theorem. (c) Single source equivalent.

Figure 3.1: Illustration of the single source equivalence theorem.

and replacing the material by the background material, an arbitrary field distribution can be allowed inside $\mathcal{V}$ [1]. This additional degree of freedom can then be utilized to eliminate one of the surface current densities [2].

The general equivalence theorem is demonstrated in Fig. 3.1(a) and Fig. 3.1(b). To guarantee the conservation of the outside field quantities $(\mathbf{e}_0, \mathbf{h}_0)$, the two surface current densities take the following form

$$\mathbf{j}_s = \hat{\mathbf{n}} \times \left(\mathbf{h} - \mathbf{h}'\right) \tag{3.1}$$

$$\mathbf{m}_s = -\hat{\mathbf{n}} \times \left(\mathbf{e} - \mathbf{e}'\right). \tag{3.2}$$

With $(\mathbf{e}', \mathbf{h}') = (\mathbf{0}, \mathbf{0})$, i.e., Love's equivalence theorem, and taking the boundary conditions (2.15)–(2.16) for Fig. 3.1(a) into account, (3.1)–(3.2) indeed reduces to (2.30)–(2.31). However, when considering the situation in Fig. 3.1(b) and choosing $\mathbf{m}_s$ to vanish, we get the case shown in Fig. 3.1(c). For this single source equivalent, the following conditions apply

$$\mathbf{j}_s = \hat{\mathbf{n}} \times \left(\mathbf{h} - \mathbf{h}''\right) \tag{3.3}$$

$$\hat{\mathbf{n}} \times \mathbf{e} = \hat{\mathbf{n}} \times \mathbf{e}''. \tag{3.4}$$

With the (rotated) tangential electric field $\hat{\mathbf{n}} \times \mathbf{e}''$ fully defined on $\mathcal{S}$, the uniqueness theorem is satisfied [3] and the fields $(\mathbf{e}'', \mathbf{h}'')$ are unique inside $\mathcal{V}$. Nonetheless, they do not carry any physical meaning or useful information about the original fields $(\mathbf{e}, \mathbf{h})$ inside the volume. As such, these fields are in a sense fictitious and not employed to infer any characteristics from the original situation in post-processing steps.

The equivalent electrical surface current density $\mathbf{j}_s$ is unknown at this point. To find a relation between this quantity and the fields outside $\mathcal{V}$, we introduce the Poincaré-Steklov or admittance operator $\mathcal{P}$ [4]. This operator maps the tangential electric field on $\mathcal{S}$ to the (rotated) tangential magnetic field on $\mathcal{S}$. For Fig. 3.1(a), this gives

$$\hat{\mathbf{n}} \times \mathbf{h} = \mathcal{P}\mathbf{e}^t, \tag{3.5}$$

while for the case depicted in Fig. 3.1(c), we get

$$\hat{\mathbf{n}} \times \mathbf{h}'' = \mathcal{P}'' \mathbf{e}^t. \tag{3.6}$$

In the definition of (3.6), we have employed (3.4) to replace $\mathbf{e}''$ by $\mathbf{e}$ on $\mathcal{S}$. By subtracting the expressions of both operators and invoking (3.3) and (2.15) in the original situation, we obtain the following result for $\mathbf{j}_s$:

$$\mathbf{j}_s = \left(\mathcal{P} - \mathcal{P}''\right) \mathbf{e}_0^t = \mathcal{Y}\, \mathbf{e}_0^t, \tag{3.7}$$

with $\mathcal{Y}$ the differential surface admittance operator, which defines the equivalent electrical surface current density in terms of the tangential electric field on $\mathcal{S}$. This relation will generally be global; $\mathbf{j}_s$ in one point $\mathbf{r}$ on $\mathcal{S}$ will depend on $\mathbf{e}_0^t$ everywhere on the boundary surface of $\mathcal{V}$.

3.2 Nonmagnetic differential surface admittance operator

In this section we derive an expression for $\mathcal{Y}$ in case of a nonmagnetic material or less strict, for a material with the same permeability as the background material, i.e., $\mu = \mu_0$. Furthermore, we require that no sources are present inside $\mathcal{V}$. The expression is based on the eigenmodes of a PEC cavity with the same shape as $\mathcal{V}$.

The electric fields inside $\mathcal{V}$ in both Fig. 3.1(a) and Fig. 3.1(c) now satisfy the sourceless Helmholtz equation:

$$\nabla \times \nabla \times \mathbf{e} - k^2 \mathbf{e} = 0, \tag{3.8}$$

$$\nabla \times \nabla \times \mathbf{e}'' - k_0^2 \mathbf{e}'' = 0. \tag{3.9}$$

Subtracting (3.9) from (3.8) and defining $\boldsymbol{\mathcal{E}}$ as $\mathbf{e} - \mathbf{e}''$ shows that

$$\nabla \times \nabla \times \boldsymbol{\mathcal{E}} - k_0^2 \boldsymbol{\mathcal{E}} = (k^2 - k_0^2)\mathbf{e}, \tag{3.10}$$

while $\hat{\mathbf{n}} \times \boldsymbol{\mathcal{E}} = 0$ on $\mathcal{S}$. These relations imply that $\boldsymbol{\mathcal{E}}$ can be expanded in the electric solenoidal eigenvectors [5] as defined in (2.34)–(2.35)

$$\boldsymbol{\mathcal{E}} = \sum_{\nu} a_\nu \mathbf{e}_\nu. \tag{3.11}$$

An important property of these eigenmodes is their orthogonality. Consequently,

$$\int_{\mathcal{V}} \mathbf{e}_\nu \cdot \mathbf{e}_\tau^* \, \mathrm{d}V = \mathcal{N}_\nu^2 \, \delta_{\nu\tau}, \tag{3.12}$$

with $\delta_{\nu\tau}$ the Kronecker delta and $\mathcal{N}_\nu^2$ a normalization factor. The star * denotes the complex conjugate. This orthogonality can be proven in a couple of simple steps,

employing the proper Green's theorem and (2.34)–(2.35):

$$\begin{aligned}
(k_\nu^2-k_\tau^2)\int_{\mathcal{V}}\mathbf{e}_\nu\cdot\mathbf{e}_\tau^*\,\mathrm{d}V &= \int_{\mathcal{V}}(k_\nu^2\mathbf{e}_\nu)\cdot\mathbf{e}_\tau^*-\mathbf{e}_\nu\cdot(k_\tau^2\mathbf{e}_\tau)^*\,\mathrm{d}V\\
&= \int_{\mathcal{V}}(\nabla\times\nabla\times\mathbf{e}_\nu)\cdot\mathbf{e}_\tau^*-\mathbf{e}_\nu\cdot(\nabla\times\nabla\times\mathbf{e}_\tau^*)\,\mathrm{d}V\\
&= \int_{\mathcal{V}}(\nabla\times\mathbf{e}_\nu)\cdot(\nabla\times\mathbf{e}_\tau^*)\,\mathrm{d}V-\int_{\mathcal{S}}\left(\mathbf{e}_\tau^*\times(\nabla\times\mathbf{e}_\nu)\right)\cdot\hat{\mathbf{n}}\,\mathrm{d}S\\
&\quad-\int_{\mathcal{V}}(\nabla\times\mathbf{e}_\tau^*)\cdot(\nabla\times\mathbf{e}_\nu)\,\mathrm{d}V+\int_{\mathcal{S}}\left(\mathbf{e}_\nu\times(\nabla\times\mathbf{e}_\tau^*)\right)\cdot\hat{\mathbf{n}}\,\mathrm{d}S\\
&= -\int_{\mathcal{S}}\underbrace{(\hat{\mathbf{n}}\times\mathbf{e}_\tau)^*}_{=0}\cdot(\nabla\times\mathbf{e}_\nu)\,\mathrm{d}S+\int_{\mathcal{S}}\underbrace{(\hat{\mathbf{n}}\times\mathbf{e}_\nu)}_{=0}\cdot(\nabla\times\mathbf{e}_\tau^*)\,\mathrm{d}S\\
&= 0, \qquad (3.13)
\end{aligned}$$

with $k_\nu^2\neq k_\tau^2$ indicating that this applies for non-degenerate eigenmodes. In case two eigenmodes share the same wavenumber, the Gram-Schmidt procedure can be applied to orthogonalize these eigenmodes.

Since both the eigenvectors and $\boldsymbol{\mathcal{E}}$ satisfy the same boundary condition, we can safely apply the $\nabla\times\nabla\times$ operator to (3.11), which, by invoking (2.34), yields

$$\nabla\times\nabla\times\boldsymbol{\mathcal{E}}=\sum_\nu k_\nu^2 a_\nu\mathbf{e}_\nu. \qquad (3.14)$$

Substituting this expansion into (3.10), multiplying both sides with $\mathbf{e}_\tau^*$, and integrating over $\mathcal{V}$ leads to

$$a_\tau\left(k_\tau^2-k_0^2\right)\mathcal{N}_\tau^2=(k^2-k_0^2)\int_{\mathcal{V}}\mathbf{e}\cdot\mathbf{e}_\tau^*\,\mathrm{d}V, \qquad (3.15)$$

by exploiting the orthogonality property (3.12). The volume integral in the above expression can be reduced to a surface integral confined to $\mathcal{S}$. To this end, we employ (2.34) to rewrite the volume integral and invoke the proper Green's theorem together with (2.35) to get

$$k_\tau^2\int_{\mathcal{V}}\mathbf{e}\cdot\mathbf{e}_\tau^*\,\mathrm{d}V=k^2\int_{\mathcal{V}}\mathbf{e}\cdot\mathbf{e}_\tau^*\,\mathrm{d}V+\int_{\mathcal{S}}\underbrace{(\hat{\mathbf{n}}\times\mathbf{e}_\tau)^*}_{=0}\cdot(\nabla\times\mathbf{e})\,\mathrm{d}S-\int_{\mathcal{S}}(\hat{\mathbf{n}}\times\mathbf{e})\cdot(\nabla\times\mathbf{e}_\tau)^*\,\mathrm{d}S. \qquad (3.16)$$

Now suppose we have normalized the eigenmodes according to (2.40) such that

$$\nabla\times\mathbf{e}_\tau=k_\tau\mathbf{h}_\tau \qquad (3.17)$$

and vice versa, with $\mathbf{h}_\tau$ the magnetic solenoidal eigenvectors (see (2.38)). To emphasize that the tangential electric fields on $\mathcal{S}$ in both Fig. 3.1(a) and Fig. 3.1(c)

are identical and additionally equal to the tangential electric field just outside $\mathcal{V}$, we denote the tangential component of $\mathbf{e}$ on $\mathcal{S}$ as $\mathbf{e}_0^t$, as in (3.7). This yields the final expression for the coefficient a_τ:

$$a_\tau = \frac{-k_\tau\left(k^2-k_0^2\right)}{\left(k_\tau^2-k_0^2\right)\left(k_\tau^2-k^2\right)\mathcal{N}_\tau^2}\int_{\mathcal{S}}\left(\hat{\mathbf{n}}\times\mathbf{e}_0^t\right)\cdot\mathbf{h}_\tau^*\,\mathrm{d}S. \tag{3.18}$$

To conclude this derivation, we apply the curl to (3.11):

$$\nabla\times\boldsymbol{\mathcal{E}} = -j\omega\mu_0\left(\mathbf{h}-\mathbf{h}''\right) = \sum_\nu k_\nu a_\nu \mathbf{h}_\nu. \tag{3.19}$$

Employing (3.3) finally leads to an expression for the surface current density:

$$\mathbf{j}_s = \mathcal{Y}\mathbf{e}_0^t = -\frac{1}{j\omega\mu_0}\sum_\nu k_\nu a_\nu\left(\hat{\mathbf{n}}\times\mathbf{h}_\nu\right), \tag{3.20}$$

which can be rewritten, by means of the contrast parameter

$$\eta = \left(k^2-k_0^2\right)/j\omega\mu_0 = \sigma_0-\sigma+j\omega\left(\epsilon_0-\epsilon\right), \tag{3.21}$$

as

$$\mathbf{j}_s = \eta\sum_\nu\left[\frac{k_\nu^2}{\left(k_\nu^2-k^2\right)\left(k_\nu^2-k_0^2\right)\mathcal{N}_\nu^2}\int_{\mathcal{S}}\left(\hat{\mathbf{n}}\times\mathbf{e}_0^t\right)\cdot\mathbf{h}_\nu^*\,\mathrm{d}S\right]\left(\hat{\mathbf{n}}\times\mathbf{h}_\nu\right). \tag{3.22}$$

The presented form of the differential surface admittance operator $\mathcal{Y}$ has the main advantage that the integral it entails does not depend in any way on the material properties, as is the case in conventional methods, but only involves the (unknown) electric field on the boundary and the magnetic eigenmodes of the cavity.

3.3 Resonator theory based derivation

Here, we present an alternative derivation for (3.22) based on the theory of resonators as presented in [5]. Although the start and end result are the same, we additionally assume here that the eigenmodes are chosen to be real.

Observe once again, the cases depicted in Fig. 3.1(a) and Fig. 3.1(c). In both situations, the fields inside $\mathcal{V}$ satisfy Maxwell's curl equations (2.1)–(2.2)

$$\nabla\times\mathbf{e} = -j\omega\mu_0\mathbf{h} \qquad \nabla\times\mathbf{e}'' = -j\omega\mu_0\mathbf{h}'' \tag{3.23}$$

$$\nabla\times\mathbf{h} = j\omega\epsilon\mathbf{e} \qquad \nabla\times\mathbf{h}'' = j\omega\epsilon_0\mathbf{e}'' \tag{3.24}$$

and the boundary conditions (2.15)–(2.18)

$$\hat{\mathbf{n}} \cdot \mu_0 (\mathbf{h}_0 - \mathbf{h}) = 0 \qquad \hat{\mathbf{n}} \cdot \mu_0 \left(\mathbf{h}_0 - \mathbf{h}''\right) = 0 \tag{3.25}$$

$$\hat{\mathbf{n}} \times (\mathbf{e}_0 - \mathbf{e}) = 0 \qquad \hat{\mathbf{n}} \times \left(\mathbf{e}_0 - \mathbf{e}''\right) = 0 \tag{3.26}$$

$$\hat{\mathbf{n}} \times (\mathbf{h}_0 - \mathbf{h}) = 0 \qquad \hat{\mathbf{n}} \times \left(\mathbf{h}_0 - \mathbf{h}''\right) = \mathbf{j}_s. \tag{3.27}$$

By subtracting the relations (3.23)–(3.24) that hold for both cases and introducing the field differences as $\mathcal{E} = \mathbf{e} - \mathbf{e}''$ and $\mathcal{H} = \mathbf{h} - \mathbf{h}''$, we get

$$\nabla \times \mathcal{E} = -j\omega\mu_0 \mathcal{H} \tag{3.28}$$

$$\nabla \times \mathcal{H} = j\omega\epsilon_0 \mathcal{E} + j\omega (\epsilon - \epsilon_0)\, \mathbf{e} \equiv j\omega\epsilon_0 \mathcal{E} + \mathcal{J}, \tag{3.29}$$

where we have designated $j\omega(\epsilon - \epsilon_0)\,\mathbf{e}$ as an impressed (bulk) electric current $\mathcal{J}$. The same reasoning leads to the following boundary conditions:

$$\hat{\mathbf{n}} \cdot \mu_0 \mathcal{H} = 0 \tag{3.30}$$

$$\hat{\mathbf{n}} \times \mathcal{E} = 0 \tag{3.31}$$

$$\hat{\mathbf{n}} \times \mathcal{H} = \mathbf{j}_s. \tag{3.32}$$

From (3.28)–(3.32) we deduce that the field differences describe the fields inside a cavity homogeneously filled with the background material and bounded by perfect electrically conducting walls. From Section 2.1.7, we know that this implies that all quantities can be expanded into their corresponding eigenmodes. Since all fields inside $\mathcal{V}$ for both cases are divergence-free, we only need to take the solenoidal eigenmodes into account, i.e., we can ignore $\mathbf{f}_\nu$ and $\mathbf{g}_\nu$ in our expansions. Therefore, we can write $\mathcal{E}$, $\mathcal{H}$ and $\mathcal{J}$ as

$$\mathcal{E} = \sum_\nu a_\nu \mathbf{e}_\nu \tag{3.33}$$

$$\mathcal{H} = \sum_\nu b_\nu \mathbf{h}_\nu \tag{3.34}$$

$$\mathcal{J} = \sum_\nu c_\nu \mathbf{e}_\nu. \tag{3.35}$$

Generally it does not hold that the curl of an infinite sum is equal to the sum of the curl of the individual terms. As such, the curls of the field differences are expanded, separately, into eigenmodes as well:

$$\nabla \times \mathcal{E} = \sum_\nu r_\nu \mathbf{h}_\nu \tag{3.36}$$

$$\nabla \times \mathcal{H} = \sum_\nu s_\nu \mathbf{e}_\nu. \tag{3.37}$$

Plugging these expansions into (3.28)–(3.29) and taking the orthogonality of the eigenmodes into account, the following relations between the expansion coefficients are found:

$$r_\nu = -j\omega\mu_0 b_\nu \tag{3.38}$$
$$s_\nu = j\omega\epsilon_0 a_\nu + c_\nu. \tag{3.39}$$

In determining the remaining coefficients, we project (3.35)–(3.37) onto the various eigenvectors and integrate over $\mathcal{V}$. For this, we will exploit a few properties of these eigenvectors. Besides the choice for real eigenmodes, we invoke the normalization defined in (2.40). A consequence of this is that both sets of eigenmodes share the same normalization constant $\mathcal{N}_\nu$:

$$\mathcal{N}_\nu^2 = \int_{\mathcal{V}} |\mathbf{e}_\nu|^2 \,\mathrm{d}V = \int_{\mathcal{V}} |\mathbf{h}_\nu|^2 \,\mathrm{d}V. \tag{3.40}$$

We start by projecting both sides of (3.35) onto $\mathbf{e}_\tau$ and invoke the eigenmode orthogonality, which leads to

$$c_\tau \mathcal{N}_\tau^2 = \int_{\mathcal{V}} \mathcal{J} \cdot \mathbf{e}_\tau \,\mathrm{d}V = j\omega(\epsilon - \epsilon_0) \int_{\mathcal{V}} \mathbf{e}_\tau \cdot \mathbf{e} \,\mathrm{d}V. \tag{3.41}$$

By utilizing the Helmholtz equation for $\mathbf{e}_\tau$ and the appropriate integral relationships, the integral on the right-hand side is rewritten as

$$\begin{aligned} k_\tau^2 \int_{\mathcal{V}} \mathbf{e}_\tau \cdot \mathbf{e} \,\mathrm{d}V &= \int_{\mathcal{V}} \mathbf{e}_\tau \cdot (\nabla \times \nabla \times \mathbf{e}) \,\mathrm{d}V \\ &+ \int_{\mathcal{S}} (\hat{\mathbf{n}} \times \mathbf{e}_\tau) \cdot (\nabla \times \mathbf{e}) \,\mathrm{d}S - \int_{\mathcal{S}} (\hat{\mathbf{n}} \times \mathbf{e}) \cdot (\nabla \times \mathbf{e}_\tau) \,\mathrm{d}S. \end{aligned} \tag{3.42}$$

Subsequently, the first integral on the right-hand side is transformed to the sought-after integral by invoking the (sourceless) Helmholtz equation for $\mathbf{e}$ while the penultimate term drops out as the tangential component of $\mathbf{e}_\tau$ vanishes on $\mathcal{S}$. This leads to

$$\left(k^2 - k_\tau^2\right) \int_{\mathcal{V}} \mathbf{e}_\tau \cdot \mathbf{e} \,\mathrm{d}V = k_\tau \int_{\mathcal{S}} (\hat{\mathbf{n}} \times \mathbf{e}) \cdot \mathbf{h}_\tau \,\mathrm{d}S. \tag{3.43}$$

Hence, we find the following expression for c_τ:

$$c_\tau = \frac{\left(k_0^2 - k^2\right) k_\tau}{j\omega\mu_0 \left(k^2 - k_\tau^2\right) \mathcal{N}_\tau^2} \int_{\mathcal{S}} (\hat{\mathbf{n}} \times \mathbf{e}) \cdot \mathbf{h}_\tau \,\mathrm{d}S. \tag{3.44}$$

Using the same approach for (3.36) but projecting on $\mathbf{h}_\tau$ and using the adequate vector property leads to

$$r_\tau \mathcal{N}_\tau^2 = \int_{\mathcal{V}} \nabla \cdot (\boldsymbol{\mathcal{E}} \times \mathbf{h}_\tau)\, \mathrm{d}V + \int_{\mathcal{V}} \boldsymbol{\mathcal{E}} \cdot (\nabla \times \mathbf{h}_\tau)\, \mathrm{d}V. \tag{3.45}$$

The first integral can be transformed to a surface integral by the divergence theorem and promptly vanishes because of (3.31). For the second integral we substitute the expansion for $\boldsymbol{\mathcal{E}}$:

$$r_\tau \mathcal{N}_\tau^2 = k_\tau \sum_\nu a_\nu \int_{\mathcal{V}} \mathbf{e}_\nu \cdot \mathbf{e}_\tau \, \mathrm{d}V \tag{3.46}$$

By once again invoking the mode orthogonality, we get the following simple relation between r_τ and a_τ:

$$r_\tau = k_\tau a_\tau, \tag{3.47}$$

thus revealing that in this particular case the curl of an infinite sum is indeed the sum of the curl of the individual terms.

Starting from (3.37), an analogous reasoning leads to the following expression for s_τ:

$$s_\tau = k_\tau b_\tau. \tag{3.48}$$

Combining (3.44), (3.47) and (3.48) with (3.38)–(3.39) enables us to find the following expressions for $\boldsymbol{\mathcal{E}}$ and $\boldsymbol{\mathcal{H}}$:

$$\boldsymbol{\mathcal{E}} = \sum_\nu \mathbf{e}_\nu \frac{-j\omega\mu_0\, \eta\, k_\nu}{\left(k_0^2 - k_\nu^2\right)\left(k^2 - k_\nu^2\right)\mathcal{N}_\nu^2} \int_{\mathcal{S}} (\hat{\mathbf{n}} \times \mathbf{e}) \cdot \mathbf{h}_\nu \, \mathrm{d}S \tag{3.49}$$

$$\boldsymbol{\mathcal{H}} = \sum_\nu \mathbf{h}_\nu \frac{\eta\, k_\nu^2}{\left(k_0^2 - k_\nu^2\right)\left(k^2 - k_\nu^2\right)\mathcal{N}_\nu^2} \int_{\mathcal{S}} (\hat{\mathbf{n}} \times \mathbf{e}) \cdot \mathbf{h}_\nu \, \mathrm{d}S, \tag{3.50}$$

with the contrast parameter η as defined in (3.21).

Plugging (3.50) into (3.32) and employing (3.26), i.e., $\hat{\mathbf{n}} \times \mathbf{e} = \hat{\mathbf{n}} \times \mathbf{e}_0$, gives us the following relation between $\mathbf{j}_s$ and the tangential electric field $\mathbf{e}_0^t$ on $\mathcal{S}$:

$$\mathbf{j}_s = -\eta \sum_\nu \frac{\mathcal{K}_\nu}{\mathcal{N}_\nu^2} \left[\int_{\mathcal{S}} (\hat{\mathbf{n}} \times \mathbf{h}_\nu) \cdot \mathbf{e}_0^t \, \mathrm{d}S \right] (\hat{\mathbf{n}} \times \mathbf{h}_\nu), \tag{3.51}$$

where $\mathcal{K}_\nu$ is introduced for compactness of notation and defined as

$$\mathcal{K}_\nu = \frac{k_\nu^2}{\left(k_0^2 - k_\nu^2\right)\left(k^2 - k_\nu^2\right)} \tag{3.52}$$

Careful comparison of (3.22) and (3.51) shows that both formulations are indeed equivalent (for real eigenfunctions).

References

[1] R. F. Harrington, *Time-Harmonic Electromagnetic Fields*. Wiley-IEEE Press, Sep. 2001.

[2] E. Martini, G. Carli, and S. Maci, "An equivalence theorem based on the use of electric currents radiating in free space", *IEEE Antennas Wireless Propag. Lett.*, vol. 7, pp. 421–424, 2008.

[3] C. Balanis, *Advanced Engineering Electromagnetics, 2nd Edition*. Wiley, 2012.

[4] L. Knockaert and D. De Zutter, "On the complex symmetry of the Poincaré-Steklov operator", *Prog. Electromagn. Res. B*, vol. 7, pp. 145–157, 2008.

[5] J. G. Van Bladel, *Electromagnetic Fields*. John Wiley & Sons, Inc., May 2007.

4

Scattering at Finite Conductors

"No, I move slow. I want to stop time. I'll sit here till I find the problem."

Tyler Joseph

★ ★ ★

In this chapter a novel approach to simulate nonmagnetic homogeneous materials, in particular good conductors, in a boundary integral equation context is introduced. The advocated 3-D differential surface admittance operator relies on the eigenmodes of the volume and as such avoids cumbersome integrals of the Green's function in the medium. Furthermore, a Method of Moments scheme for cylinders is proposed that, through the use of curved rectangles with associated rooftops, preserves the curved nature of the volume, leading to an efficient discretization. Combining both novel methods results in an efficient and versatile way to assess scattering and antenna characteristics. This is demonstrated by studying scattering at different materials and analyzing the influence of finite conductivity on the performance of a dipole and a Yagi-Uda antenna.

4.1 Introduction

The impact of the finite conductivity on scattering and antenna characteristics has been a research topic for over half a century. Initially, approximate current distributions were utilized to include the imperfect conductors' effect on cylindrical scatterers [1] and thin-wire antennas [2]. Another approach uses the surface impedance concept. This impedance relates the external tangential electric and magnetic field at the boundary of the object under study by a function that depends on the material's properties, as such eliminating the need to solve the internal field

problem. This approach thus employs the same principle as the Poincaré-Steklov operator and the differential surface admittance operator, introduced in Chapter 3, but differs from these techniques at a couple of crucial points. Firstly, the surface impedance, or similar methods [3], impose a *local* relationship between the electric and magnetic field on the surface that approximates the true *global* relationship as captured by the aforementioned operators. Secondly, since it is derived based on the study of a planar interface of a good conductor with vacuum [4], it can only be employed for good conductors with sufficient dielectric contrast with the background medium and for a moderate curvature of the boundary surface [5]. Nevertheless, the surface impedance or, as it is also known, the Leontovich boundary condition [6], is widely utilized in modeling good conductors. It is defined as

$$\mathbf{e}^t = Z_s \hat{\mathbf{n}} \times \mathbf{h}^t, \tag{4.1}$$

with the surface impedance $Z_s = (1+j)/\sigma\delta$ equal to the wave impedance Z_c inside the good conductor (see (2.14)). We stress here once more that (4.1) relates both field quantities in a single point by means of the scalar Z_s in contrast to (3.5), which entails a global relation on the entire boundary surface. To overcome its shortcomings, higher-order approximations of the surface impedance boundary condition have been proposed, extending its applicability [7]. Nevertheless, these extensions do not suffice to capture the complete current crowding phenomenon from direct current (DC) to the highest frequencies. Therefore, we propose a differential surface admittance operator for cylinders that produces accurate results for any nonmagnetic material and curvature.

We start by proposing a novel, specific MoM formulation for cylinders, tailored towards this geometry by introducing curved basis functions in Section 4.2. The differential surface admittance operator, as introduced in Chapter 3, is developed for cylinders in Section 4.3. The discretization of this continuous operator by means of the specific set of basis functions is discussed in this section as well. Next, we apply this novel method to a range of examples to show its properties, validity and appositeness in Section 4.5.

4.2 EFIE formulation for cylinders

4.2.1 Basis functions

As discussed in Section 2.2.2, surface meshes are predominately triangle based. Meshing the boundary surface of a circular cylinder by flat triangles, effectively transforms the cylinder into a prism-like polyhedron, losing its curved nature and its circular symmetry. This phenomenon is of course not unique to the cylinder and occurs for all curved objects, as shown for example in Fig. 2.4(a). The effect is generally circumvented by increasing the number of triangles (see e.g., Fig. 2.4(b)), thus improving the approximation of the cylinder, but inadvertently driving up the number of unknowns and the corresponding computational cost. Although curvi-

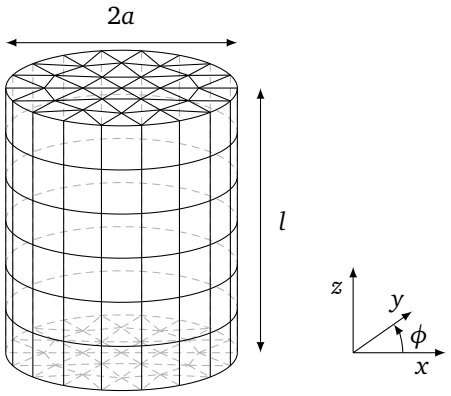

Figure 4.1: Surface mesh of a cylinder using curved rectangles on the mantle and triangles on the end caps.

linear mesh elements do exist, they are usually based on polynomial interpolation and do not have the required fixed radius of curvature of circular cylinders/spheres (see e.g., Figure 4 in [8]), introducing once again approximations of the actual shape. To fully preserve the curved nature of the mantle of the cylinder, we propose here the use of curved rectangles as shown in Fig. 4.1. The corresponding linear basis functions, shown in Fig. 4.2, are defined analogously to the rooftops on flat rectangles (see Fig. 2.5(b) and (2.45)). For the z-oriented rooftop this results in

$$\mathbf{f}_j(\mathbf{r}) = \begin{cases} \left[z - z_j^+\right]\hat{\mathbf{z}}/A_j^+, & \text{if } \mathbf{r} \in \mathrm{R}_j^+ \\ \left[z_j^- - z\right]\hat{\mathbf{z}}/A_j^-, & \text{if } \mathbf{r} \in \mathrm{R}_j^- \\ 0, & \text{elsewhere,} \end{cases} \tag{4.2}$$

where $A_j^\pm$ is the area of the curved rectangle $\mathrm{R}_j^\pm$, respectively, while the ϕ-oriented rooftops are defined as

$$\mathbf{f}_j(\mathbf{r}) = \begin{cases} \left[\phi - \phi_j^+\right]\hat{\boldsymbol{\phi}}/A_j^+, & \text{if } \mathbf{r} \in \mathrm{R}_j^+ \\ \left[\phi_j^- - \phi\right]\hat{\boldsymbol{\phi}}/A_j^-, & \text{if } \mathbf{r} \in \mathrm{R}_j^- \\ 0, & \text{elsewhere.} \end{cases} \tag{4.3}$$

Care should be taken in calculating the divergence of these rooftops, especially the angular ones. The nabla operator in cylindrical coordinates is defined as $\nabla = \frac{\partial}{\partial\rho}\hat{\boldsymbol{\rho}} + \frac{1}{\rho}\hat{\boldsymbol{\rho}} + \frac{1}{\rho}\frac{\partial}{\partial\phi}\hat{\boldsymbol{\phi}} + \frac{\partial}{\partial z}\hat{\mathbf{z}}$, leading thus to (with a the radius of the cylinder)

$$\nabla \cdot (4.2) = \pm\frac{1}{A_j^\pm} \tag{4.4}$$

$$\nabla \cdot (4.3) = \pm\frac{1}{aA_j^\pm}. \tag{4.5}$$

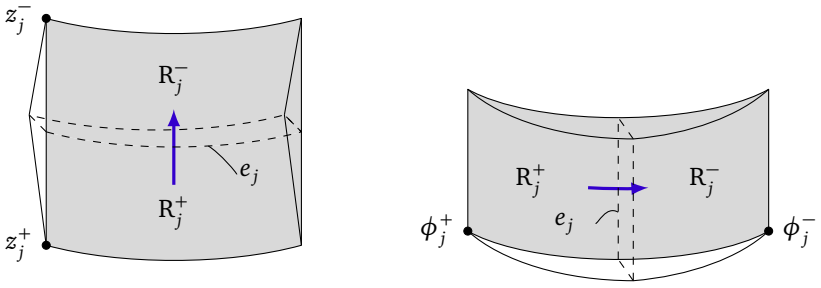

(a) z-oriented rooftop function $\mathbf{f}_j(\mathbf{r})$ defined over curved rectangles R_j^+ and R_j^+.

(b) ϕ-oriented rooftop basis function $\mathbf{f}_j(\mathbf{r})$ defined over curved rectangles R_j^+ and R_j^+.

Figure 4.2: Basis functions defined over a pair of adjacent curved rectangles with common edge e_j.

The (flat) end caps of the cylinders are meshed with triangles (see Fig. 4.1). The corresponding basis functions are the RWG functions [9] as illustrated and defined in (2.44) and Fig. 2.5(a).

This only leaves the edges at the circumference of the end caps to be modeled. The basis functions on these edges are hybrid functions consisting of one half of an RWG and one half of a z-oriented rooftop. The common edge is bifurcated due to a mismatch between the straight edge of the triangle and the bent edge of the curved rectangle involved. As shown, albeit exaggerated, in Fig. 4.3, this leaves a circular segment of the surface uncovered by the mesh and accompanying basis functions. To circumvent this issue, a local Kirchhoff approximation is introduced: all the current that enters/leaves the triangle through the straight edge exits/enters the curved edge immediately. Clearly, this tactic is only valid as long as the distance the current transverses instantly, i.e., the width of the circular segment, is negligible as compared to the wavelength. This way, the error in delay/phase will be acceptable. Considering that the typical mesh length in a MoM mesh is an order of magnitude smaller than the wavelength, the transversal dimension of the circular segment is easily an additional order of magnitude smaller, thus justifying the approximation.

4.2.2 Integrals

With the above choice of basis functions, we can now calculate the elements of the MoM matrix $\overline{\overline{Z}}$ as defined in (2.53). For the two surface integrals of the curved rectangles, the standard Gauss-Legendre quadrature is used, albeit in the (ϕ, z)-plane instead of a Cartesian coordinate plane [10]. For the triangles, a variant of the same quadrature rule specifically tailored towards triangles is applied [11]–[13]. For the hybrid integrals, i.e., a double integral over a triangle/curved rectangle

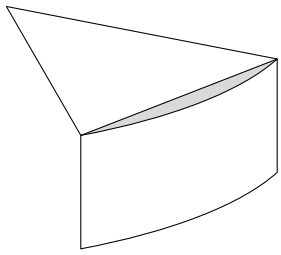

Figure 4.3: Detail of the surface mesh at the circumference of the top end cap. The gray colored area of the surface is not covered by the mesh (exaggerated).

pair, a combined set of quadrature points is used. To cope with the singularities in the integrals, we employ the first method introduced in Section 2.2.3, viz., singularity extraction.

Triangles

The singularity $1/R$ (with R the distance between a point of a triangle and an observation point) can be integrated analytically using the method described in [14]. The integration over the second triangle is then regularized and can thus be tackled by numerical evaluation. This method can be used for any singularity: proximity, vertex, edge and self-patch. The case for two fully overlapping triangles, i.e., the so-called self-patch, is a very important and crucial one as it will contribute to the diagonal of $\overline{\overline{Z}}$, representing the strongest interactions on the surface mesh. Therefore, we employ a complete analytical solution for the double surface integrals (twice over the same triangle) as detailed in [15] to increase the accuracy.

Curved rectangles

The reciprocal Euclidean distance between two points belonging to a pair of curved rectangles becomes singular as well. The Euclidean distance between two points, given in cylindrical coordinates is

$$\begin{aligned} R(\mathbf{r}_1, \mathbf{r}_2) &= \sqrt{\rho_1^2 + \rho_2^2 - 2\rho_1\rho_2\cos(\phi_1 - \phi_2) + (z_1 - z_2)^2} \\ &= \sqrt{4a^2\sin^2\left(\frac{\phi_1 - \phi_2}{2}\right) + (z_1 - z_2)^2}, \end{aligned} \tag{4.6}$$

where the last step assumes that both points are equidistant from the central axis of the cylinder, i.e., $\rho_1 = \rho_2 = a$. In contrast to the distance function in Cartesian coordinates, $\int R^{-1}\,\mathrm{d}S$ over a curved rectangle is not analytically integrable; integration over the angle will result in the incomplete elliptic integral of the first kind [16], preventing further analytical integration. To circumvent this problem,

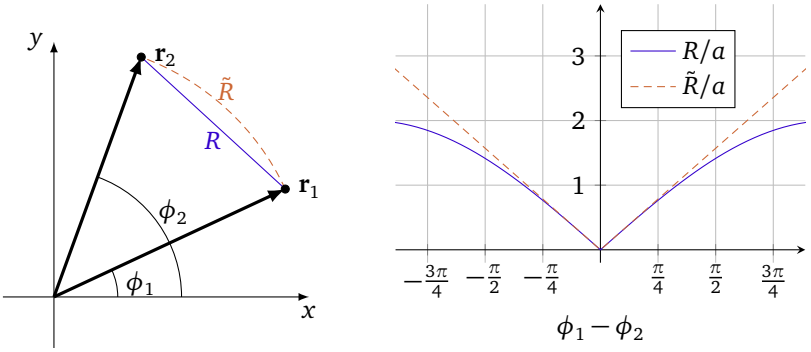

(a) Two points with the Euclidean distance R and its approximation $\tilde{R}$.

(b) Different distance measures (normalized to the radius a) as a function of $\phi_1-\phi_2$.

Figure 4.4: Illustration of the difference between R (blue) and $\tilde{R}$ (orange) for $z_1 = z_2$.

we remark that the analytical integration will only be applied for adjacent or overlapping patches. As such, $\phi_1-\phi_2$ will evaluate to small values and we can approximate the sine in (4.6) by its first order Taylor expansion, leading to an approximate distance function

$$\tilde{R} = \sqrt{a^2(\phi_1-\phi_2)^2+(z_1-z_2)^2}. \tag{4.7}$$

In Fig. 4.4, the difference between both distance measures is illustrated for two points in the same xy-plane. We clearly see that the approximate distance measure approaches the actual Euclidean distance for small angles $\phi_1-\phi_2$. With this distance function, the four-dimensional integration over two curved rectangles of $1/\tilde{R}$ can now be performed analytically, the result of which is presented in Section A.1 in Appendix A. The remainder of the integrand, i.e., in free space

$$G(R)-\frac{1}{\tilde{R}} = \frac{e^{-jkR}}{R}-\frac{1}{\tilde{R}} = \frac{\tilde{R}e^{-jkR}-R}{R\tilde{R}} \tag{4.8}$$

has been regularized and can thus be integrated numerically. For the MoM integrals stemming from the vector potential (first double integral in (2.53)), additional terms appear in the numerator that have to be integrated analytically alongside $1/\tilde{R}$ as well. For the z-oriented rooftops, a factor $\left(z_1-z_1^{\pm}\right)\left(z_2-z_2^{\pm}\right)$ or similar expressions are introduced that fortunately pose no problem to the integration (see Section A.1). The term $\left(\phi_1-\phi_1^{\pm}\right)\left(\phi_2-\phi_2^{\pm}\right)\cos(\phi_1-\phi_2)$ accounts for the ϕ-oriented basis functions, with the cosine originating from $\hat{\boldsymbol{\phi}}_1\cdot\hat{\boldsymbol{\phi}}_2$. The combination of this cosine with $1/\tilde{R}$ is not analytically integrable. To solve this problem, the cosine is approximated by its zeroth order expansion, i.e., 1. Higher accuracy can be obtained by including the second order term $(\phi_1-\phi_2)^2/2$. These integrations can be found in Section A.1 as well.

Triangle-rectangle pair

As the singularity expressions for triangles are exact and do not employ a Taylor-based approximation, the singularity over the triangle is calculated analytically using the same approach as for a pair of triangles [14]. The remaining surface integral over the curved rectangle can then be tackled by numeric quadrature.

4.3 Differential surface admittance operator for cylinders

For the construction of the differential surface admittance operator, as defined in (3.22), we need an expression for the (magnetic) eigenfunctions of a cylindrical cavity, which are calculated analytically in the following subsection. Some properties of these eigenfunctions are computed and discussed as well. In Section 4.3.2, the discretization of the continuous operator is elaborated upon. Through combination with the MoM matrix this then leads to a set of matrix equations that, when solved simultaneously, enables the computation of scattered fields at homogeneous cylinders.

4.3.1 Eigenfunctions of a cylindrical cavity

Circular waveguide

The way we construct the eigenmodes of a cylinder is to first take a look at the eigenmodes of a circular waveguide and in a second step, turn this infinite waveguide into a cavity by terminating its ends with PEC plates. To this end, suppose the cylinder has radius a with its axis aligned along the z-axis. We now split the fields into a longitudinal and transversal part, and through separation of variables write the field quantities as $\mathbf{x}(\mathbf{r}) = \mathbf{x}(\boldsymbol{\rho})e^{-j\gamma z}$, with $\gamma = \beta - j\alpha$, $\beta > 0$ and $\alpha > 0$, enabling a decoupling of Maxwell's (sourceless) curl equations (2.1)–(2.2) into the following set of equations

$$\nabla_t \times e_z(\boldsymbol{\rho})\hat{\mathbf{z}} - j\gamma\hat{\mathbf{z}} \times \mathbf{e}_t(\boldsymbol{\rho}) = -j\omega\mu_0\mathbf{h}_t(\boldsymbol{\rho}) \tag{4.9}$$

$$\nabla_t \times \mathbf{e}_t(\boldsymbol{\rho}) = -j\omega\mu_0 h_z(\boldsymbol{\rho})\hat{\mathbf{z}} \tag{4.10}$$

$$\nabla_t \times h_z(\boldsymbol{\rho})\hat{\mathbf{z}} - j\gamma\hat{\mathbf{z}} \times \mathbf{h}_t(\boldsymbol{\rho}) = j\omega\epsilon\mathbf{e}_t(\boldsymbol{\rho}) \tag{4.11}$$

$$\nabla_t \times \mathbf{h}_t(\boldsymbol{\rho}) = j\omega\epsilon e_z(\boldsymbol{\rho})\hat{\mathbf{z}}, \tag{4.12}$$

where the subscript t denotes transversal components. Through a few substitutions, we can isolate two independent, concurrent Helmholtz equations for h_z and e_z:

$$\nabla_t^2 h_z + \left(k^2 - \gamma^2\right) h_z = 0 \tag{4.13}$$

$$\nabla_t^2 e_z + \left(k^2 - \gamma^2\right) e_z = 0. \tag{4.14}$$

It can be shown that for a homogeneous medium these two equations give rise to two classes of solutions, viz., transverse electric (TE) and transverse magnetic (TM) modes, for which e_z and h_z, respectively, are non-existent. The complete field profile of the TE modes can be derived from h_z as

$$\mathbf{e}_t = \frac{j\omega\mu_0}{k^2-\gamma^2}\left(\hat{\mathbf{z}}\times\nabla_t h_z\right) \tag{4.15}$$

$$\mathbf{h}_t = -\frac{j\gamma}{k^2-\gamma^2}\nabla_t h_z. \tag{4.16}$$

For the TM modes, the transversal fields are

$$\mathbf{e}_t = -\frac{j\gamma}{k^2-\gamma^2}\nabla_t e_z \tag{4.17}$$

$$\mathbf{h}_t = -\frac{j\omega\epsilon_0}{k^2-\gamma^2}\left(\hat{\mathbf{z}}\times\nabla_t e_z\right). \tag{4.18}$$

The solutions to (4.13)–(4.14) for a circle can be found by applying separation of variables in polar coordinates and by invoking the relevant PEC boundary conditions [17], [18]. For the TE modes this leads to the modal field distributions

$$h_{z,mn}(\boldsymbol{\rho}) = J_n(\lambda_{mn}\rho)\,e^{jn\phi} \tag{4.19}$$

$$\mathbf{e}_{t,mn}(\boldsymbol{\rho}) = \frac{j\omega\mu_0}{\lambda_{mn}^2}\left[\lambda_{mn}J_n'(\lambda_{mn}\rho)\,\hat{\boldsymbol{\phi}} - \frac{jn}{\rho}J_n(\lambda_{mn}\rho)\,\hat{\boldsymbol{\rho}}\right]e^{jn\phi} \tag{4.20}$$

$$\mathbf{h}_{t,mn}(\boldsymbol{\rho}) = -\frac{j\gamma_{mn}}{\lambda_{mn}^2}\left[\lambda_{mn}J_n'(\lambda_{mn}\rho)\,\hat{\boldsymbol{\rho}} + \frac{jn}{\rho}J_n(\lambda_{mn}\rho)\,\hat{\boldsymbol{\phi}}\right]e^{jn\phi}, \tag{4.21}$$

with $n\in\mathbb{Z}$, $m\in\mathbb{N}$, $\gamma_{mn}=\sqrt{k^2-\lambda_{mn}^2}$ and $\lambda_{mn}=y_{mn}/a$, where y_{mn} is the m-th zero of the first derivative of the Bessel function of the first kind of order n, i.e., $J_n'(y_{mn})=0$. For the TM modes the expressions are

$$e_{z,mn}(\boldsymbol{\rho}) = J_n(\mu_{mn}\rho)\,e^{jn\phi} \tag{4.22}$$

$$\mathbf{e}_{t,mn}(\boldsymbol{\rho}) = -\frac{j\gamma_{mn}}{\mu_{mn}^2}\left[\mu_{mn}J_n'(\mu_{mn}\rho)\,\hat{\boldsymbol{\rho}} + \frac{jn}{\rho}J_n(\mu_{mn}\rho)\,\hat{\boldsymbol{\phi}}\right]e^{jn\phi} \tag{4.23}$$

$$\mathbf{h}_{t,mn}(\boldsymbol{\rho}) = -\frac{j\omega\epsilon_0}{\mu_{mn}^2}\left[\mu_{mn}J_n'(\mu_{mn}\rho)\,\hat{\boldsymbol{\phi}} - \frac{jn}{\rho}J_n(\mu_{mn}\rho)\,\hat{\boldsymbol{\rho}}\right]e^{jn\phi}, \tag{4.24}$$

with $\gamma_{mn}=\sqrt{k^2-\lambda_{mn}^2}$ and $\mu_{mn}=x_{mn}/a$, where x_{mn} is the m-th zero of the Bessel function of the first kind of order n, i.e., $J_n(x_{mn})=0$. Note that we have chosen, for compactness of notation, to use complex functions for our eigenmodes. It can easily be shown, however, that through linear combinations of two eigenmodes with opposite n, two subsets of real eigenmodes can be obtained per TE/TM set.

Cylindrical cavity

With the modal fields in the cross-section fully determined, we express the fields anywhere in the (infinite) waveguide as a superposition of a right- and left-traveling wave for every eigenmode:

$$\begin{aligned}\mathbf{e}(\mathbf{r}) = &\sum_{n,m} K_{mn}^{+}\left[\mathbf{e}_{t,mn}(\boldsymbol{\rho}) + e_{z,mn}(\boldsymbol{\rho})\hat{\mathbf{z}}\right]e^{-j\gamma_{mn}z} \\ &+ \sum_{n,m} K_{mn}^{-}\left[\mathbf{e}_{t,mn}(\boldsymbol{\rho}) - e_{z,mn}(\boldsymbol{\rho})\hat{\mathbf{z}}\right]e^{j\gamma_{mn}z} \end{aligned} \tag{4.25}$$

$$\begin{aligned}\mathbf{h}(\mathbf{r}) = &\sum_{n,m} K_{mn}^{+}\left[\mathbf{h}_{t,mn}(\boldsymbol{\rho}) + h_{z,mn}(\boldsymbol{\rho})\hat{\mathbf{z}}\right]e^{-j\gamma_{mn}z} \\ &+ \sum_{n,m} K_{mn}^{-}\left[-\mathbf{h}_{t,mn}(\boldsymbol{\rho}) + h_{z,mn}(\boldsymbol{\rho})\hat{\mathbf{z}}\right]e^{j\gamma_{mn}z}. \end{aligned} \tag{4.26}$$

To turn this waveguide into a resonator cavity with height l, the structure is terminated at $z = -l/2$ and $z = l/2$ with PEC end caps, implying that the tangential electric field vanishes at these points. From (4.25), for every separate eigenmode this entails

$$K_{mn}^{+}\mathbf{e}_{t,mn}(\boldsymbol{\rho})e^{j\gamma_{mn}l/2} + K_{mn}^{-}\mathbf{e}_{t,mn}(\boldsymbol{\rho})e^{-j\gamma_{mn}l/2} = 0 \tag{4.27}$$

$$K_{mn}^{+}\mathbf{e}_{t,mn}(\boldsymbol{\rho})e^{-j\gamma_{mn}l/2} + K_{mn}^{-}\mathbf{e}_{t,mn}(\boldsymbol{\rho})e^{j\gamma_{mn}l/2} = 0, \tag{4.28}$$

which in turn leads to the restrictions

$$K_{mn}^{-} = -K_{mn}^{+}e^{\pm j\gamma l} \tag{4.29}$$

$$\sin(\gamma_{mn}l) = 0. \tag{4.30}$$

The second condition forces the propagation constants γ_{mn} to take the values $p\pi/l$ with p a natural number. This requirement is not met generally but, as γ_{mn} is a function of k and thus of the frequency, it can be satisfied at certain frequencies only, i.e., the resonant frequencies. With these restrictions in place, (4.25)–(4.26) becomes for every mode

$$\mathbf{e}_{mnp}(\mathbf{r}) = \mathbf{e}_{t,mn}\sin\left(\frac{p\pi}{l}\left(z - \frac{l}{2}\right)\right) + je_{z,mn}\cos\left(\frac{p\pi}{l}\left(z - \frac{l}{2}\right)\right)\hat{\mathbf{z}} \tag{4.31}$$

$$\mathbf{h}_{mnp}(\mathbf{r}) = Z_c\mathbf{h}_{t,mn}\cos\left(\frac{p\pi}{l}\left(z - \frac{l}{2}\right)\right) - jZ_c h_{z,mn}\sin\left(\frac{p\pi}{l}\left(z - \frac{l}{2}\right)\right)\hat{\mathbf{z}}, \tag{4.32}$$

with Z_c the characteristic impedance (cf. (2.10)). As eigenmodes are only determined up to a (complex) constant, the above expressions have been normalized such that the additional conditions formulated in (2.40) are satisfied.

Applied to the circular waveguide, this yields the full field description of the resonant eigenmodes of the cylindrical cavity. As a result of (4.30), the wavenumber k,

will be discretized. For the TE modes, we get

$$k_{mnp}^2 = \lambda_{mn}^2 + \left(\frac{p\pi}{l}\right)^2 = \frac{y_{mn}^2}{a^2} + \left(\frac{p\pi}{l}\right)^2. \tag{4.33}$$

For the modal field distributions themselves, the substitution of (4.19)–(4.21) into (4.31)–(4.32) yields

$$\mathbf{e}_{mnp}(\mathbf{r}) = k_{mnp}\left[\lambda_{mn} J_n'(\lambda_{mn}\rho)\,\hat{\boldsymbol{\phi}} - \frac{jn}{\rho} J_n(\lambda_{mn}\rho)\,\hat{\boldsymbol{\rho}}\right] e^{jn\phi} \sin\left(\frac{p\pi}{l}z - \frac{p\pi}{2}\right) \tag{4.34}$$

$$\begin{aligned}\mathbf{h}_{mnp}(\mathbf{r}) = -\frac{p\pi}{l}&\left[\lambda_{mn} J_n'(\lambda_{mn}\rho)\,\hat{\boldsymbol{\rho}} + \frac{jn}{\rho} J_n(\lambda_{mn}\rho)\,\hat{\boldsymbol{\phi}}\right] e^{jn\phi} \cos\left(\frac{p\pi}{l}z - \frac{p\pi}{2}\right) \\ &- \lambda_{mn}^2 J_n(\lambda_{mn}\rho)\, e^{jn\phi} \sin\left(\frac{p\pi}{l}z - \frac{p\pi}{2}\right)\hat{\mathbf{z}}.\end{aligned} \tag{4.35}$$

Note that for $p = 0$, the TE eigenmodes do not exist as all the fields are zero.

For the TM modes, on the other hand, the wavenumber is defined as

$$k_{mnp}^2 = \mu_{mn}^2 + \left(\frac{p\pi}{l}\right)^2 = \frac{x_{mn}^2}{a^2} + \left(\frac{p\pi}{l}\right)^2, \tag{4.36}$$

and the modal field distributions are given as

$$\begin{aligned}\mathbf{e}_{mnp}(\mathbf{r}) = -\frac{p\pi}{l}&\left[\mu_{nm} J_n'(\mu_{nm}\rho)\,\hat{\boldsymbol{\rho}} + \frac{jn}{\rho} J_n(\mu_{nm}\rho)\,\hat{\boldsymbol{\phi}}\right] e^{jn\phi} \sin\left(\frac{p\pi}{l}z - \frac{p\pi}{2}\right) \\ &+ \mu_{nm}^2 J_n(\mu_{nm}\rho)\, e^{jn\phi} \cos\left(\frac{p\pi}{l}z - \frac{p\pi}{2}\right)\hat{\mathbf{z}}\end{aligned} \tag{4.37}$$

$$\mathbf{h}_{mnp}(\mathbf{r}) = -k_{nmp}\left[\mu_{nm} J_n'(\mu_{nm}\rho)\,\hat{\boldsymbol{\phi}} - \frac{jn}{\rho} J_n(\mu_{nm}\rho)\,\hat{\boldsymbol{\rho}}\right] e^{jn\phi} \cos\left(\frac{p\pi}{l}z - \frac{p\pi}{2}\right). \tag{4.38}$$

In the definition of the differential surface admittance operator (3.22), one of the terms in the denominator is the normalization constant $\mathcal{N}_\nu^2$, which is defined in (3.12). This constant can be calculated analytically for both sets of eigenmodes by calculating the volume integral, which is separable in cylindrical coordinates, and invoking various (integral) properties of the Bessel functions [19]. For the TE modes, this leads to

$$\mathcal{N}_{mn0}^2 = 0 \tag{4.39}$$

$$\mathcal{N}_{mnp}^2 = k_{mnp}^2 \frac{\pi l}{2}\left(y_{mn}^2 - n^2\right) J_n(y_{mn}), \tag{4.40}$$

$$\tag{4.41}$$

while for the TM modes, the factor is

$$\mathcal{N}_{mnp}^2 = k_{mnp}^2 \frac{\pi l}{\varepsilon_p} x_{mn}^2 J_{n+1}(x_{mn}), \tag{4.42}$$

with ε_p the Neumann factor (see [17]), which evaluates to 1 for $p = 0$ and becomes 2 for all other natural numbers.

4.3.2 Discretization

With all the necessary quantities denoted, we have fully defined the continuous differential surface admittance operator for cylinders. As we have opted for a definition of the eigenmodes with complex functions, we are obliged to use definition (3.22) of the operator. The discretization approach is essentially the MoM procedure; the tangential electric field is expanded into basis functions:

$$\mathbf{e}_0^t = \sum_{j=1}^{N} E_j \mathbf{f}_j(\mathbf{r}), \tag{4.43}$$

and both sides of the equation are tested with the same functions $\mathbf{f}$ to obtain the discretized version of the $\mathcal{Y}$ operator, i.e., $\overline{\overline{Y}}$, with its elements defined as:

$$\overline{\overline{Y}}_{ij} = -\eta \sum_{m,n,p} \frac{\mathcal{K}_{mnp}}{\mathcal{N}_{mnp}^2} \int_{\mathcal{S}_j} \left(\hat{\mathbf{n}} \times \mathbf{h}_{mnp}^*\right) \cdot \mathbf{f}_j(\mathbf{r})\, \mathrm{d}S \int_{\mathcal{S}_i} \left(\hat{\mathbf{n}} \times \mathbf{h}_{mnp}\right) \cdot \mathbf{f}_i(\mathbf{r})\, \mathrm{d}S. \tag{4.44}$$

Note that in the calculation of each element, a triple infinite sum is present. In a numerical implementation, this summation has to be limited along its three dimensions. These maximum values are denoted as (M, N, P), keeping in mind that, as n is an integer, n ranges from $-N$ to N. Moreover, we have to remember that there exist two sets of magnetic eigenmodes, viz., TE and TM. For every value (m, n, p), there are thus two contributions to every matrix element.

The integrals in (4.44) can be evaluated either analytically or numerically. For the RWG functions used on the end caps, one has to resort to numerical evaluation as the basis functions generally do not have a simple form in cylindrical coordinates that enables integration in conjunction with the (derivative of) Bessel functions. On the other hand, for the mantle of the cylinder, the curved rectangles and associated rooftops provide an easy evaluation of the required integrals; both the (rotated) magnetic eigenmodes and the rooftops are expressed in cylindrical coordinates leading to separate integrals over ϕ and z. These integrals can be solved by straightforward substitutions and through partial integration.

4.4 Full-wave solution

At this point, we combine the discretized differential surface admittance operator with the EFIE operator to obtain a full description of the electromagnetic problem. The main difference with the PEC scattering described in Section 2.2.1, is the boundary condition (2.42): the total electric field, i.e., the sum of the incident and scattered field, does not vanish at the surface as it did for a PEC. Instead, (3.7) has

to satisfied: the current surface density and the electric field at the boundary are related through the differential surface admittance operator $\mathcal{Y}$. In other words, two equations have to be satisfied simultaneously:

$$\hat{\mathbf{n}} \times \mathbf{e}_0^t = \hat{\mathbf{n}} \times \mathbf{e}_{\text{inc}} - Z_c \mathcal{T} \mathbf{j}_s \tag{4.45}$$

$$\mathbf{j}_s = \mathcal{Y} \mathbf{e}_0^t. \tag{4.46}$$

It is evident from the above equations that a simple substitution would suffice to get a single equation for one of the unknowns, i.e., $\mathbf{j}_s$ or $\mathbf{e}_0^t$. However, this combined equation will contain the concatenation of both the $\mathcal{T}$ and $\mathcal{Y}$ operator. Discretization will as such prove a very difficult task, if not impossible, certainly given the singular nature of the integrals in the $\mathcal{T}$ operator. As such, we discretize both (4.45) and (4.46) separately and solve them jointly afterwards. This implies that both $\mathbf{j}_s$ and $\mathbf{e}_0^t$ are to be expanded into basis functions:

$$\mathbf{j}_s = \sum_{p=1}^{N} I_p \mathbf{f}_p(\mathbf{r}) \tag{4.47}$$

$$\mathbf{e}_0^t = \sum_{q=1}^{N} E_q \mathbf{f}_q(\mathbf{r}). \tag{4.48}$$

Plugging these expansions into (4.45) and testing both sides with $\hat{\mathbf{n}} \times \mathbf{f}_i$, yields

$$\sum_q E_q \left\langle \hat{\mathbf{n}} \times \mathbf{f}_i, \hat{\mathbf{n}} \times \mathbf{f}_q \right\rangle = \langle \hat{\mathbf{n}} \times \mathbf{f}_i, \hat{\mathbf{n}} \times \mathbf{e}_{\text{inc}} \rangle - Z_c \sum_p I_q \left\langle \hat{\mathbf{n}} \times \mathbf{f}_i, \mathcal{T} \mathbf{f}_q \right\rangle, \tag{4.49}$$

which can be written compactly as

$$\overline{\overline{G}} \mathbf{E} = \mathbf{P} - \overline{\overline{Z}} \mathbf{I}, \tag{4.50}$$

with $\mathbf{P}$, $\mathbf{I}$ and $\overline{\overline{Z}}$ as defined in (2.51)–(2.53). The elements of $\mathbf{E}$ and the Gram matrix $\overline{\overline{G}}$ are given by

$$\mathbf{E}_i = E_i \tag{4.51}$$

$$\overline{\overline{G}}_{ij} = \int_{\mathcal{S}} \mathbf{f}_i(\mathbf{r}) \cdot \mathbf{f}_j(\mathbf{r}) \, \mathrm{d}S. \tag{4.52}$$

A similar procedure, but testing with $\mathbf{f}_i$ transforms (4.46) into

$$\sum_p I_p \left\langle \mathbf{f}_i, \mathbf{f}_p \right\rangle = \sum_q E_q \left\langle \mathbf{f}_i, \mathcal{Y} \mathbf{f}_p \right\rangle, \tag{4.53}$$

or in compact matrix notation

$$\overline{\overline{G}} \mathbf{I} = \overline{\overline{Y}} \mathbf{E}, \tag{4.54}$$

where the matrix $\overline{\overline{Y}}$ was defined previously in (4.44). Note that for multiple objects (cylinders), $\overline{\overline{Y}}$ is a block diagonal matrix where each block represents the differential surface admittance matrix for each individual object.

Both matrix equations (4.50) and (4.54) together form the discrete version of the continuous equations we intend to solve. By rewriting (4.54) and substituting the result into (4.50), we obtain one single matrix equation

$$\left(\overline{\overline{G}} + \overline{\overline{Z}}\,\overline{\overline{G}}^{-1}\,\overline{\overline{Y}}\right)\mathbf{E} = \mathbf{P}, \tag{4.55}$$

or alternatively, by substituting (4.50) into (4.54), this yields

$$\left(\overline{\overline{G}} + \overline{\overline{Y}}\,\overline{\overline{G}}^{-1}\,\overline{\overline{Z}}\right)\mathbf{I} = \overline{\overline{Y}}\,\overline{\overline{G}}^{-1}\,\mathbf{P}. \tag{4.56}$$

Both equations can be solved either directly or iteratively. In the examples presented in the next section, no discernible advantage for either one of the equations in terms of accuracy (or conditioning) was found. As we are usually interested in the surface current density, (4.56) was preferred.

Gram matrix

The Gram matrix $\overline{\overline{G}}$, defined in (4.52), is a sparse matrix due to the local nature of the employed basis functions. After all, the integral does not vanish if and only if both functions share a common patch (triangle/curved rectangle). For the RWG this thus amounts to a maximum of five nonzero entries per row/column. For the curved rooftops and the hybrid functions, it boils down to three and four elements, respectively, because of the orthogonality of rooftops functions along different coordinate axes.

The integrals featured in the evaluation of these nonzero elements can often be calculated analytically. For the RWG functions, the integrals can be decomposed into various contributions of the form

$$\int_{\mathrm{T}} (\mathbf{r}-\mathbf{r}_a)\cdot(\mathbf{r}-\mathbf{r}_b)\,\mathrm{d}S. \tag{4.57}$$

This integral over the triangle T is the inner product of two half RWGs on the same triangle with $\mathbf{r}_a$ and $\mathbf{r}_b$ the *anchor* points of their respective functions. These points lie at one of the three vertices $(\mathbf{p},\mathbf{q},\mathbf{s})$ of the triangle. With A the area of the triangle, the result of the above integral is [20]

$$\begin{aligned} 2\mathrm{A}\Bigg[&\frac{1}{12}(\mathbf{p}\cdot(\mathbf{p}+\mathbf{q}+\mathbf{s})+\mathbf{q}\cdot(\mathbf{q}+\mathbf{s})+\mathbf{s}\cdot\mathbf{s}) \\ &-\frac{1}{6}(\mathbf{p}+\mathbf{q}+\mathbf{s})\cdot(\mathbf{r}_a+\mathbf{r}_b)+\frac{1}{2}\mathbf{r}_a\cdot\mathbf{r}_b\Bigg]. \end{aligned} \tag{4.58}$$

Closed expressions for the Gram integrals can be found for the curved rectangles as well. Demonstrated here for the z-oriented rooftops (the case of the ϕ-oriented rooftops being completely analogous), two types of simple integrals are found

$$\int_{\phi_0}^{\phi_1}\int_{z_0}^{z_1} (z-z_0)^2 \,\mathrm{d}S = \int_{\phi_0}^{\phi_1}\int_{z_0}^{z_1} (z_1-z)^2 \,\mathrm{d}S = A\frac{(z_1-z_0)^2}{3} \tag{4.59}$$

$$\int_{\phi_0}^{\phi_1}\int_{z_0}^{z_1} (z-z_0)(z_1-z) \,\mathrm{d}S = A\frac{(z_1-z_0)^2}{6}, \tag{4.60}$$

with A the area of the curved rectangle.

4.5 Examples

4.5.1 Validation examples

Scattering at a single cylinder

To validate the novel method, scattering at a single, homogeneous cylinder is considered for several materials. A reference solution is obtained from an in-house, all-purpose BIE-MoM solver [21], [22] that does not leverage the surface admittance operator. At 1 GHz, a cylinder with radius $a = \lambda/3$ and height 2λ is illuminated by a plane wave. The dimensions of the edges in the surface mesh are of the order $\lambda/12$. Traveling along $\hat{\mathbf{x}}$ in the horizontal plane, i.e., in the plane perpendicular to the axis, the plane wave is TE-polarized, viz. its magnetic field is aligned with the axis of the cylinder. Three different materials are studied: a low-contrast dielectric with $\epsilon_r = 4$, a high-contrast dielectric with $\epsilon_r = 100$ and copper with a conductivity of $\sigma = 5.8 \cdot 10^7$ S/m. Radar cross-sections (RCS*s*) in the horizontal plane, halfway the cylinder's length are shown in Fig. 4.6 (only half the range is plotted due to symmetry). These results are computed through the expressions provided in Appendix B. The solid lines represent the reference solution while the various markers demonstrate the solutions obtained by means of the differential surface admittance operator with the cut-off values of the eigenmodes at $(M,N,P) = (200,15,25)$ for the low-contrast dielectric, $(200,50,15)$ for the cylinder with $\epsilon_r = 100$ and $(600,15,25)$ for the copper filled cylinder.

As is evident from Fig. 4.6, excellent agreement between the reference solution and the novel formalism is found. The total root mean square (rms) error stays well below 1% for all examples, validating the accuracy of the differential surface admittance operator. The remaining, minor deviations can be attributed to the mesh detail in both solvers, the finite number of eigenmodes in the novel method and rounding errors.

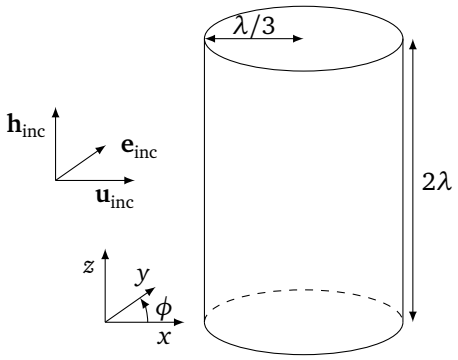

Figure 4.5: Cylinder with length 2λ and radius $a = \lambda/3$ at 1 GHz. A TE-polarized plane wave travels along $\hat{\mathbf{x}}$ in the horizontal plane.

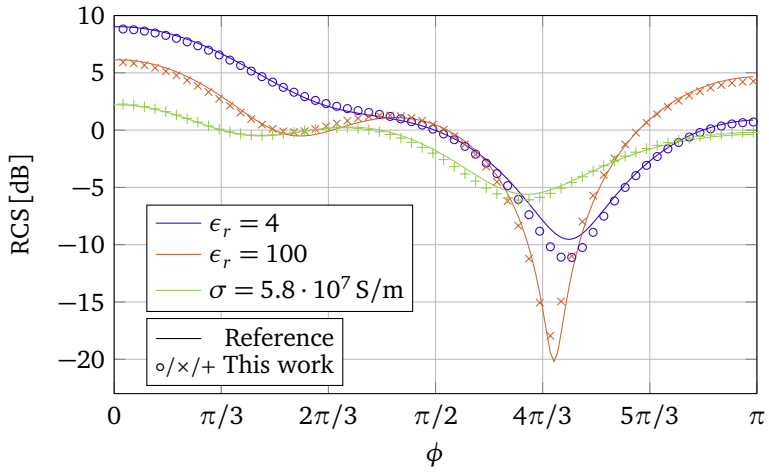

Figure 4.6: Radar cross-sections of the cylinder depicted in Fig. 4.5, illuminated by a plane wave. Reference results for the simulated materials, i.e., a low-contrast dielectric, a high-contrast dielectric and copper, are obtained using in-house BIE-MoM software that is not based on the surface admittance operator.

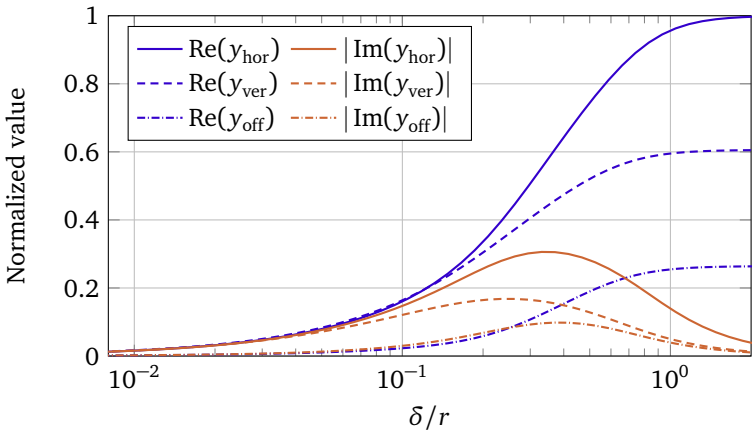

Figure 4.7: Normalized real (blue) and imaginary (orange) part of three selected $\overline{\overline{Y}}$ matrix elements as a function of the normalized skin depth.

Analysis of the discretized $\mathcal{Y}$-operator

Before turning our attention to application examples, the behavior of the $\overline{\overline{Y}}$ matrix is explored in more detail. To this end, the evolution of three matrix elements for the copper cylinder with radius a of the previous section as a function of the relative skin depth δ/a is examined: y_{hor} and y_{ver} both correspond to a diagonal element, the former for a horizontal edge and the latter for a vertical edge on the mantle of the cylinder. The third element y_{off} is an off-diagonal matrix entry that represents the interaction between two vertical mantle edges on opposite sides of the cylinder. The real part (black lines) and imaginary part (gray lines) of these three quantities are shown in Fig. 4.7. The results demonstrate that the real parts are dominant and constant for large relative skin depths while the imaginary parts gain in importance as the skin depth decreases. For very small skin depths, only the diagonal elements remain significant and become proportional to the classical *point-wise* surface admittance $Y_s = \sqrt{\sigma/(j\omega\mu)}$, indicated by the identical absolute value of their real and imaginary part.

Another important influence on the matrix elements is the number of eigenmodes that are taken into account. To illustrate this, the diagonal elements of the previous example, i.e., y_{hor} and y_{ver}, are computed over the same frequency range for an increasing number of eigenmodes in the radial direction, i.e., for increasing M. N and P are set to 5 for this particular example but note that the analysis remains valid for other parameter values as well. The relative error is plotted in Fig. 4.8 where the reference solution is the one obtained for $M = 5000$ as the absolute change in matrix entries was negligible for larger M. As is evident from the graph, a modest number of eigenmodes, say 100, suffices for large skin depths while current crowding in the skin effect regime requires an increasing amount of eigenmodes to be fully captured.

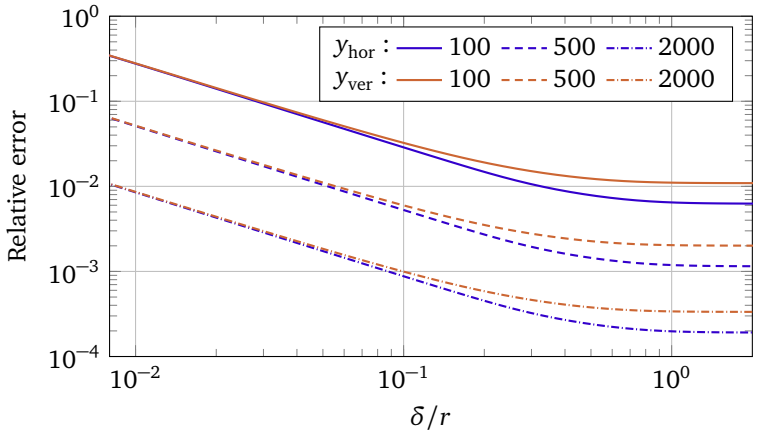

Figure 4.8: Relative error of two distinct diagonal $\overline{\overline{Y}}$ matrix elements, i.e., y_{hor} and y_{ver}, as a function of normalized skin depth for the copper cylinder of Fig. 4.6 for various values of M. Error values are defined with respect to the solution for $M = 5000$.

4.5.2 Application examples

Dipole antenna

Consider a dipole antenna in free space with a total length of 2λ at 1 GHz. As the diameter of wire antennas is generally much smaller than their length (and the wavelength), the radius a is set to $\lambda/500$. The width of the gap between the two cylinders constituting the antenna, is set to $a/50$[1]. The structure is excited by an impinging TM-polarized plane wave for varying inclination angles θ. The normalized open circuit voltage $V_{\text{open, norm}}$ over the dipole's gap, i.e., the potential difference between both cylinders, is numerically computed for increasing conductivity and displayed in Fig. 4.10. The voltage values are normalized with respect to the peak value of the solution for a PEC cylinder (denoted in Fig. 4.10 by the solid line). The range of eigenmodes in this example is given by $(M, N, P) = (500, 12, 15)$. Only half of the range of θ is plotted due to symmetry in the response characteristic. It is evident from the results that, with increasing conductivity, the voltage response evolves towards that of the perfectly conducting cylinder, which is indeed to be expected. At the same time, however, it shows that for a moderate conductivity, a substantial change in antenna response is to be expected. Although such conductivities are well below those of traditional conductors such as copper, they can, for example, be found in solar applications or transparent technologies where materials such as indium tin oxide (ITO) and PEDOT:PSS with typical conductivity values of around $2.4 \cdot 10^5$ S/m and 10^3 S/m, respectively [25], [26], are utilized.

[1] Employing other types of gaps/excitations, e.g., delta-gap [23], [24], will generally only change the right-hand side of (4.55).

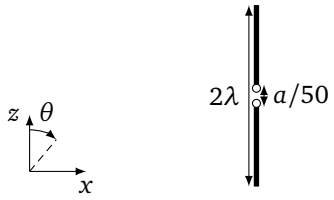

Figure 4.9: Dipole antenna with length 2λ at 1 GHz with radius $a = \lambda/500$.

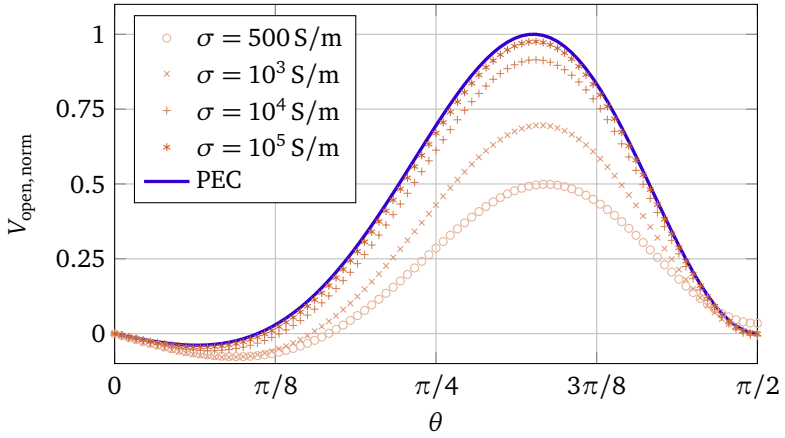

Figure 4.10: Normalized open circuit voltage $V_{\text{open,norm}}$ of a dipole for a 2λ dipole at 1 GHz for various conductivity values. The dipole is excited by a TM-polarized plane wave at varying inclination angles.

Yagi-Uda antenna

Consider the Yagi-Uda antenna displayed in Fig. 4.11. The driving component of this structure is a dipole antenna with length l_f. The remaining elements are of a parasitic nature: one reflector with length l_r at a distance d_r behind the central dipole and three directors with length l_d which are placed in front with a spacing of d_d. All wires have the same radius a. Values for these parameters can be found in Table 4.1 for the Yagi-Uda operating at 110 MHz, i.e., the center frequency of the localizer in an instrument landing system (ILS). The gain of this configuration is calculated numerically by means of the proposed differential surface admittance operator method for circular cylinders for varying inclination angles θ in the vertical plane (xz-plane). This gain pattern is plotted in Fig. 4.12 for decreasing values of the skin depth δ, i.e., for increasing conductivity σ. A reference solution for a PEC Yagi-Uda is obtained through 4nec2 [27], a free Numerical Electromagnetics Code (NEC) based antenna modeler. Due to the inherent symmetry of the structure under study, only half the range of θ is shown. It is apparent that the antenna response evolves towards that of the PEC solution for decreasing skin

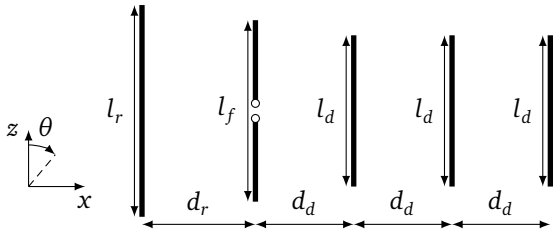

Figure 4.11: Yagi-Uda wire antenna with dipole feed, one reflector and three directors. Dimensions for operation at 110 MHz can be found in Table 4.1.

Table 4.1: Dimensions (in m) of the antenna in Fig. 4.11.

Parameter	Value	Parameter	Value
l_f	1.332	a (radius)	0.001
l_r	1.348	d_r	0.8
l_d	1.12	d_d	0.637

depths. Moreover, it is shown that an insufficient conductivity detrimentally affects the antenna's characteristics. The remaining discrepancy between the solution for $\delta/a = 0.01$ and the PEC reference can be attributed to both the fundamental approximations of the reference solution, viz., thin-wire MoM, and the finite mesh of the employed method.

The individual patterns can be interpreted as follows. For the lowest conductivity, i.e., $\delta/a = 10$, the gain pattern resembles that of a single dipole, albeit with a very low efficiency. The parasitic elements do not seem to skew the response, revealing them to be transparent for the fields emitted by the central dipole. Increasing the conductivity shifts the entire pattern up towards the 2.15 dBi gain expected for an ideal dipole antenna. At the same time, however, the influence of the reflector and directors increases and the typical Yadi-Uda skew starts emerging. This explains why the backwards gain for the $\delta/a = 1$ antenna lies above that of the better conductors: the gain of the central antenna approaches that of the individual dipole but the lowered conductivity still cripples the strength of the parasitic elements. Only when the conductivity ensures sufficiently strong skin effect phenomena, we observe a substantial front-to-back-ratio crop up.

4.6 Conclusions

In this chapter, the 3-D differential surface admittance operator has been adopted in the context of wire antennas to assess the influence of finite conductivity on their performance and characteristics. Furthermore, a specific MoM formulation, tailored to cylinders, is developed. Through the use of curved rectangles with cor-

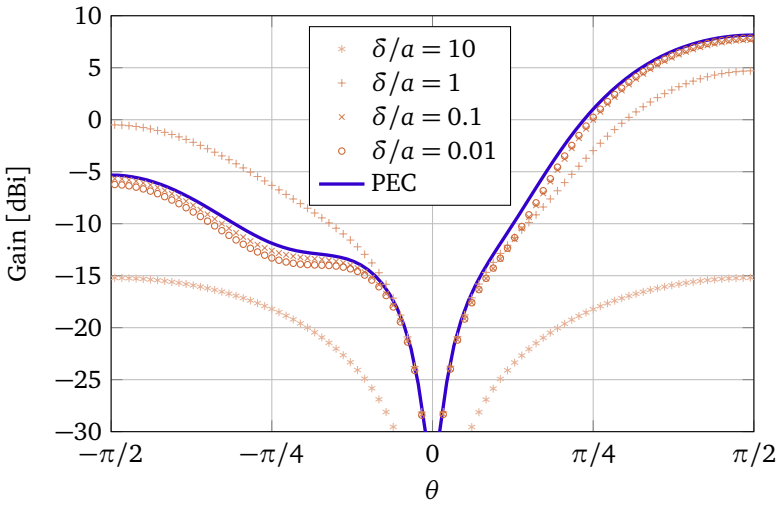

Figure 4.12: Gain of the Yagi-Uda antenna at 110 MHz for various values of the skin depth ($a = 1$ mm and $f = 110$ MHz are kept constant, only the conductivity changes). The reference PEC solution is obtained through 4nec2 [27].

responding rooftops functions, an efficient meshing of cylinders is realized without sacrificing their curved nature. The construction of the associated MoM matrix is tackled, with particular care taken in dealing with the singular integrals. The continuous differential surface admittance operator was constructed starting from the eigenfunctions of the volume and discretized on the same surface mesh, optimally exploiting its advantageous properties. The novel method was thoroughly validated by comparing its performance with an established BIE-MoM solver, proving its versatility for a wide variety of materials, while at the same time delving deeper into its broadband properties and investigating the convergence behavior of the matrix elements. Moreover, the method was utilized to examine a dipole and a Yagi-Uda antenna for various conductivity values, demonstrating its applicability in the analysis of the material's influence on antenna performance.

References

[1] E. Cassedy and J. Fainberg, "Back scattering cross sections of cylindrical wires of finite conductivity", *IRE Trans. Antennas Propag.*, vol. 8, no. 1, pp. 1–7, Jan. 1960.

[2] R. King, C. Harrison, and E. Aronson, "The imperfectly conducting cylindrical transmitting antenna: Numerical results", *IEEE Trans. Antennas Propag.*, vol. 14, no. 5, pp. 535–542, Sep. 1966.

[3] L. Medgyesi-Mitschang and J. Putnam, "Integral equation formulations for imperfectly conducting scatterers", *IEEE Trans. Antennas Propag.*, vol. 33, no. 2, pp. 206–214, Feb. 1985.

[4] F. Olyslager and D. De Zutter, "Skin effect", in *Wiley Encycl. Electr. Electron. Eng.* Hoboken, NJ, USA: John Wiley & Sons, Inc., Dec. 1999.

[5] D.-S. Wang, "Limits and validity of the impedance boundary condition on penetrable surfaces", *IEEE Trans. Antennas Propag.*, vol. 35, no. 4, pp. 453–457, Apr. 1987.

[6] T. Senior and J. Volakis, *Approximate Boundary Conditions in Electromagnetics*, ser. Electromagnetics and Radar Series. Institution of Electrical Engineers, 1995.

[7] L. Di Rienzo, S. Yuferev, and N. Ida, "Computation of the impedance matrix of multiconductor transmission lines using high-order surface impedance boundary conditions", *IEEE Trans. Electromagn. Compat.*, vol. 50, no. 4, pp. 974–984, Nov. 2008.

[8] M. Djordjević and B. Notaroš, "Double higher order Method of Moments for surface integral equation modeling of metallic and dielectric antennas and scatterers", *IEEE Trans. Antennas Propag.*, vol. 52, no. 8, pp. 2118–2129, Aug. 2004.

[9] S. Rao, D. Wilton, and A. Glisson, "Electromagnetic scattering by surfaces of arbitrary shape", *IEEE Trans. Antennas Propag.*, vol. 30, no. 3, pp. 409–418, May 1982.

[10] M. Abramowitz and I. A. Stegun, *Handbook of Mathematical Functions: With Formulas, Graphs, and Mathematical Tables*. National Bureau of Standards, 1964.

[11] G. R. Cowper, "Gaussian quadrature formulas for triangles", *Int. J. Numer. Methods Eng.*, vol. 7, no. 3, pp. 405–408, 1973.

[12] D. A. Dunavant, "High degree efficient symmetrical Gaussian quadrature rules for the triangle", *Int. J. Numer. Methods Eng.*, vol. 21, no. 6, pp. 1129–1148, Jun. 1985.

[13] S. Wandzura and H. Xiao, "Symmetric quadrature rules on a triangle", *Comput. Math. with Appl.*, vol. 45, no. 12, pp. 1829–1840, Jun. 2003.

[14] P. Ylä-Oijala and M. Taskinen, "Calculation of CFIE impedance matrix elements with RWG and n x RWG functions", *IEEE Trans. Antennas Propag.*, vol. 51, no. 8, pp. 1837–1846, Aug. 2003.

[15] P. Arcioni, M. Bressan, and L. Perregrini, "On the evaluation of the double surface integrals arising in the application of the boundary integral method to 3-D problems", *IEEE Trans. Microw. Theory Techn.*, vol. 45, no. 3, pp. 436–439, Mar. 1997.

[16] I. Gradshteyn and I. Ryzhik, *Table of Integrals, Series, and Products*. Academic Press, 2007.

[17] J. G. Van Bladel, *Electromagnetic Fields*. John Wiley & Sons, Inc., May 2007.

[18] C. Balanis, *Advanced Engineering Electromagnetics, 2nd Edition*. Wiley, 2012.

[19] F. W. J. Olver, D. W. Lozier, R. F. Boisvert, and C. W. Clark, *NIST Handbook of Mathematical Functions*. Cambridge Univ. Press, 2010.

[20] F. Boeykens, "Hybrid electromagnetic simulation techniques for the computer-aided design of flexible antennas", PhD thesis, Ghent University, Nov. 2013.

[21] M. Gossye, M. Huynen, D. Vande Ginste, D. De Zutter, and H. Rogier, "A Calderón preconditioner for high dielectric contrast media", *IEEE Trans. Antennas Propag.*, vol. 66, no. 2, pp. 808–818, Feb. 2018.

[22] I. Bogaert, "On the analytical treatment of singular impedance integrals in electromagnetics", in *2013 International Conference on Electromagnetics in Advanced Applications (ICEAA)*, Sep. 2013, pp. 624–627.

[23] R. F. Harrington, *Field Computation by Moment Methods*. Wiley-IEEE Press, May 1993.

[24] G. Eleftheriades and J. Mosig, "On the network characterization of planar passive circuits using the method of moments", *IEEE Trans. Microw. Theory Techn.*, vol. 44, no. 3, pp. 438–445, Mar. 1996.

[25] C. Kocia and S. V. Hum, "Design of an optically transparent reflectarray for solar applications using indium tin oxide", *IEEE Trans. Antennas Propag.*, vol. 64, no. 7, pp. 2884–2893, 2016.

[26] Y. H. Kim, C. Sachse, M. L. MacHala, C. May, L. Müller-Meskamp, and K. Leo, "Highly conductive PEDOT:PSS electrode with optimized solvent and thermal post-treatment for ITO-free organic solar cells", *Adv. Funct. Mater.*, vol. 21, no. 6, pp. 1076–1081, 2011.

[27] A. Voors. (2015). 4nec2: Antenna modeler, [Online]. Available: `http://www.qsl.net/4nec2/`.

5
Interconnect Modeling

"Let us step into the night and pursue that flighty temptress, adventure."

J.K. Rowling

★ ★ ★

Full-wave techniques to rigorously characterize 3-D lossy interconnects are presented in this chapter. Two distinct differential surface admittance operator formulations for cuboids are given where the second formulation employs entire domain basis functions and closed sums of infinite series to improve the accuracy and efficiency of its computation. Encompassing this operator in an alternative MPIE interpretation enables integration in conventional circuit solvers and results in accurate resistance and inductance evaluation. Combining the differential surface admittance operator with the augmented EFIE formulation leads to a matrix system that permits a comprehensive broadband full impedance characterization of interconnect structures. Both methods are thoroughly validated on numerous examples by comparison with both state-of-the-art academic research and commercial solvers demonstrating its versatility and appositeness. Additionally, various application examples are provided to further prove the applicability and accuracy of the presented work.

5.1 Introduction

The continuing search for smaller and faster electronic circuits to satisfy the needs of our information-driven global society has led to increasingly complex structures in both printed circuit board (PCB) and integrated circuit (IC) technologies. One example of such an innovation is the rise of 3-D ICs [1]. The increased density

of components and interconnects poses a myriad of challenges, not least in terms of signal integrity. Proximity of various signal lines and noisy circuits to interconnects introduces numerous detrimental phenomena such as crosstalk and signal distortion. These effects only get amplified by the cluttered electromagnetic environment and the high-frequency spectral content of digital signals caused by increasing data rates. Accurate modeling of circuits and especially interconnects becomes ever more indispensable in modern design tools.

Referring to Chapter 1 for a more detailed overview of various CEM methods that are employed in interconnect modeling, some key points are picked out here. 3-D interconnect modeling approaches can generally be categorized as either volume or surface discretization methods. The former category houses, among others, the well-known FEM. By meshing the entire 3-D volume, this method provides a versatile tool for a wide range of applications. However, volume discretization requires a very large number of (small) mesh elements to properly represent phenomena such as the skin and proximity effect in good conductors, leading to computationally intractable linear systems.

BEMs such as the MoM are inherently less susceptible to this problem as only the surface is meshed. Nevertheless, tackling the interior problem for highly conductive media remains a challenging feat. The calculation of the interaction integrals [2] or guaranteeing the accuracy of the iterative solution [3] poses big challenges of its own. A popular class of approximate techniques employs the surface impedance concept [4], previously discussed in Section 4.1. In this chapter, we introduce the differential surface admittance operator as a solution to overcome the problems generally associated with modeling lossy interconnects.

In Section 5.2, we first discuss the MoM scheme used for the modeling of cuboids, the basic building blocks for interconnects, including a discussion of the singular integrals. Additionally, two different solutions to the complete matrix system (both including the differential surface admittance operator) are proposed and compared. This operator is subsequently introduced for cuboids, once again based on the eigenfunctions of the volume, in Section 5.3. In Section 5.4, we take another look at the same operator and come up with a different calculation approach, based on entire domain basis functions, that proves to be more efficient and accurate. Afterwards, the different techniques and methods are validated, applied and compared numerically in Section 5.5.

5.2 EFIE formulation for cuboids

5.2.1 Basis functions

In contrast to the cylinder, discussed in Section 4.2, the cuboid is a volume with flat faces and we can thus without any problem apply standard surface meshing techniques, i.e., triangular and/or rectangular meshes. Here, we opt for the latter as the faces of a cuboid lend themselves perfectly to a rectangular mesh, leading

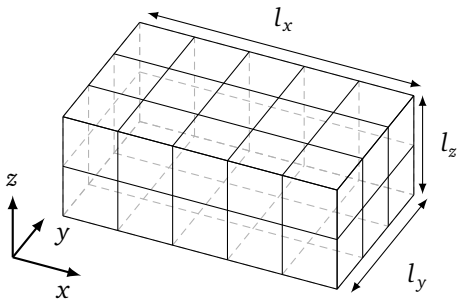

Figure 5.1: Surface mesh of a cuboid using rectangular patches.

to fewer unknowns then a triangular mesh with the same average edge length. An example of a surface mesh (with uniform subdivision along each Cartesian axis) is shown in Fig. 5.1. The associated linear basis functions are the rooftops, introduced in (2.45) and Fig. 2.5(b) in Section 2.2.2. As the rooftops on the cuboid are aligned along the principal axes of the local Cartesian coordinate system, the general definition (2.45) simplifies to expressions of the form $\pm\left(x - x_j^{\pm}\right)\hat{\mathbf{x}}/A_j^{\pm}$, with analogous forms for the other axes.

5.2.2 Integrals

With the rooftops as basis functions, the integrals for the calculation of the MoM matrix have to be tackled. As was the case for the curved rectangles and triangles, we use standard Gauss-Legendre quadrature for the four-dimensional integrals governing all pairs of rectangles. Of course, the singular integrals still pose an issue and have to be dealt with. Once again, we opt for singularity extraction. For rectangular patches a similar, general procedure as for the triangles exists [5] that calculates the inner surface integral analytically and computes the outer, regularized one numerically. In a cuboid we can go one step further since two rectangles are not oriented arbitrarily: they lie either in parallel planes (with as special case the same plane) or perpendicular planes. This results in double surface integrals that are completely analytically calculable over its four dimensions. The results of these computations are provided in Appendix A, specifically Sections A.2 and A.3.

5.2.3 Alternative interpretation of the MPIE

In Section 4.4 the EFIE in its MPIE formulation was solved jointly with the differential surface admittance operator to evaluate scattering at arbitrary materials. In this chapter, we deploy the combined techniques for the analysis of interconnects through an alternative interpretation of the EFIE that lends itself more to the study of interconnects. In this formulation, the integration of circuit elements such as

sources and other discrete elements is possible, as well as a straightforward way to connect various building blocks to build more complex structures.

The starting point is the expression for the electric field in terms of its potentials (see (2.22)), which states that the scattered field can be expressed as

$$\mathbf{e}_{\text{sc}} = \mathbf{e}_0 - \mathbf{e}_{\text{inc}} = -j\omega\mathbf{a} - \nabla\phi. \tag{5.1}$$

By introducing the same expansion and testing technique as utilized in the previous chapter (cf. (4.47)–(4.48)), we can turn (5.1) into a matrix equation. The tangential electric field $\mathbf{e}_0^t$ and surface current density $\mathbf{j}_s$ are thus expanded into linear basis functions, viz., rooftops, and the equation is tested on both sides with the same functions. For the first term on the left-hand side this leads to

$$\int_{\mathcal{S}_i} \mathbf{e}_0^t \cdot \mathbf{f}_i \,\mathrm{d}S = \sum_j E_j \int_{\mathcal{S}_i} \mathbf{f}_j \cdot \mathbf{f}_i \,\mathrm{d}S = \sum_j \overline{\overline{G}}_{ij} E_j, \tag{5.2}$$

with $\overline{\overline{G}}$ the Gram matrix. For the rooftops, each row in the Gram matrix will have three nonzero entries, which are calculated through integrals completely analogous to (4.59)–(4.60) (see also (5.79)–(5.80)).

The weighted incident field is taken into account through the vector $\mathbf{P}$, defined in (2.51). The contribution of the vector potential is a dense matrix that is obtained through expansion of the surface current density and corresponds to the first term of (2.53):

$$\int_{\mathcal{S}_i} \mathbf{a} \cdot \mathbf{f}_i \,\mathrm{d}S = \sum_j I_j \mu_0 \int_{\mathcal{S}_i} \int_{\mathcal{S}_j} G\left(|\mathbf{r} - \mathbf{r}'|\right) \mathbf{f}_j \cdot \mathbf{f}_i \,\mathrm{d}S \,\mathrm{d}S' = \sum_j \overline{\overline{L}}_{ij} I_j. \tag{5.3}$$

That leaves the scalar potential to be dealt with. By applying the proper vector identity and invoking the divergence theorem, this term becomes

$$\begin{aligned}
\int_{\mathcal{S}_i} \nabla\phi \cdot \mathbf{f}_i \,\mathrm{d}S &= \int_{\mathcal{S}_i} \nabla \cdot (\phi \mathbf{f}_i) \,\mathrm{d}S - \int_{\mathcal{S}_i} \phi \nabla \cdot \mathbf{f}_i \,\mathrm{d}S \\
&= \oint_{c_i} \phi \underbrace{\hat{\mathbf{n}} \cdot \mathbf{f}_i}_{=0} \,\mathrm{d}c - \left[\int_{\mathrm{R}_i^+} \frac{\phi}{A_i^+} \,\mathrm{d}S - \int_{\mathrm{R}_i^-} \frac{\phi}{A_i^-} \,\mathrm{d}S \right] \\
&= V_i^- - V_i^+,
\end{aligned} \tag{5.4}$$

with $V_i^\pm$ the average potential on the rectangles $\mathrm{R}_j^\pm$ that make up the basis function $\mathbf{f}_i$. As such, (5.1) is discretized into

$$\overline{\overline{G}}\mathbf{E} - \mathbf{P} = -j\omega\overline{\overline{L}}\mathbf{I} + \mathbf{V}^+ - \mathbf{V}^-, \tag{5.5}$$

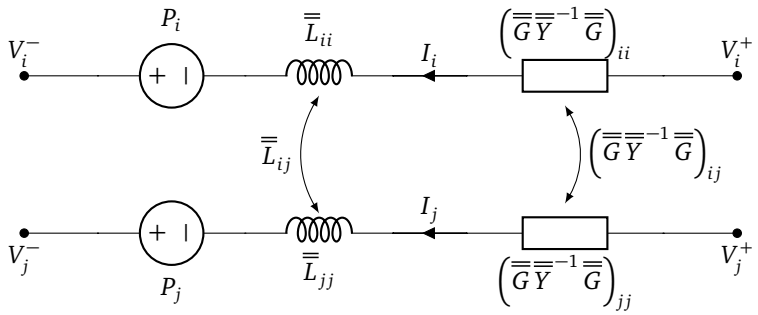

Figure 5.2: Equivalent circuit interpretation of (5.6). Each node corresponds to the average potential on a rectangle and each branch maps to an edge.

where $\mathbf{V}^{\pm}$ constellates the average potentials for all rectangles. We can now eliminate one set of unknowns by introducing the 3-D differential surface admittance operator, which will be discussed further for cuboids in Sections 5.3 and 5.4. In discretized form (see (4.54)), this operator satisfies $\overline{\overline{G}}\mathbf{I} = \overline{\overline{Y}}\mathbf{E}$, leading to

$$\left(\overline{\overline{G}}\,\overline{\overline{Y}}^{-1}\overline{\overline{G}}\right)\mathbf{I} - \mathbf{P} = -j\omega\overline{\overline{L}}\mathbf{I} + \mathbf{V}^{+} - \mathbf{V}^{-}. \tag{5.6}$$

This equation can be interpreted as a circuit with a node for every rectangle in the mesh and a branch for every edge, as shown in Fig. 5.2. The main advantage of this approach is the ease of integration with discrete components such as sources or loads and the ability to employ conventional circuit solvers. Throughout this work, (5.6) will be solved by means of the popular circuit solver LTspice® [6].

5.2.4 Augmented EFIE

Although (5.6) can be used to successfully characterize circuits, it does not offer a complete description of the electromagnetic interactions. By only taking the vector potential's influence into account through the matrix $\overline{\overline{L}}$, capacitive effects will be neglected. Notwithstanding that this approach is taken very often in interconnect modeling, if we want a truly broadband characterization of (complex) structures, it is paramount to include all electromagnetic (coupling) effects. To this end, we cast the differential surface admittance operator into the so-called augmented EFIE formulation [7]. This technique formulates two matrix equations with two sets of unknowns and solves them jointly. The first equation is actually (5.6), which can be rewritten as

$$\left(\overline{\overline{G}}\,\overline{\overline{Y}}^{-1}\overline{\overline{G}} + j\omega\overline{\overline{L}}\right)\mathbf{I} - \overline{\overline{T}}\mathbf{V} = \mathbf{P}. \tag{5.7}$$

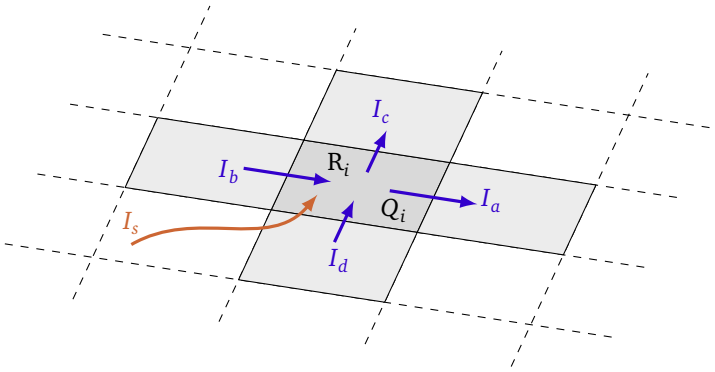

Figure 5.3: Charge conservation on a single rectangle R_i. The blue arrows represent the various rooftop functions that contribute to the charge Q on the dark gray rectangle while the orange arrow is a (possible) external current source.

The vector $\mathbf{V}$ and incidence matrix $\overline{\overline{T}}$, which maps the patches and edges of the mesh, are defined as

$$(\mathbf{V})_i = \int_{R_i} \frac{\phi}{A_i}\, dS, \tag{5.8}$$

$$\left(\overline{\overline{T}}\right)_{ij} = \begin{cases} 1, & \text{if } R_j \text{ is } R_i^+ \text{ of } \mathbf{f}_i \\ -1, & \text{if } R_j \text{ is } R_i^- \text{ of } \mathbf{f}_i \\ 0, & \text{otherwise,} \end{cases} \tag{5.9}$$

with R_g being a rectangle of the surface mesh with a corresponding area A_g. The second equation is found by discretizing the following expression for the scalar potential

$$\phi(\mathbf{r}) = \frac{1}{\epsilon_0} \int_S G\left(|\mathbf{r}-\mathbf{r}'|\right) \rho_s\left(\mathbf{r}'\right) dS'. \tag{5.10}$$

Inserting the piecewise constant divergence of the basis functions that correspond to the charge on each patch and averaging over the rectangles of the mesh, leads to the following matrix relation

$$\mathbf{V} = \overline{\overline{K}}\mathbf{Q}, \tag{5.11}$$

with the column vector $\mathbf{Q}$ collecting the charges on each rectangle and with the elements of $\overline{\overline{K}}$ given by

$$\overline{\overline{K}}_{ij} = \frac{1}{\epsilon_0} \int_{R_i} \int_{R_j} \frac{G\left(|\mathbf{r}-\mathbf{r}'|\right)}{A_i A_j}\, dS\, dS'. \tag{5.12}$$

To eliminate $\mathbf{Q}$, we discretize the conservation of charge law on every rectangle. As shown for an arbitrary rectangle R_i in Fig. 5.3, various currents (can) contribute

to a single rectangle: rooftops defined on adjacent patches and possibly external current sources. The charge conservation equation $\nabla \cdot \mathbf{j}_s + j\omega\rho_s = 0$ on R_i then becomes

$$I_a - I_b + I_c - I_d + j\omega Q_i = I_s. \tag{5.13}$$

Generalizing this relation to all mesh elements, leads to the matrix equation

$$\overline{\overline{T}}^T \mathbf{I} + j\omega\mathbf{Q} = \mathbf{S}, \tag{5.14}$$

where the vector $\mathbf{S}$ contains the external current sources.

Combining (5.7) together with (5.11) and (5.14), leads to the following set of matrix equations

$$\begin{bmatrix} \overline{\overline{G}}\,\overline{\overline{Y}}^{-1}\overline{\overline{G}} + j\omega\overline{\overline{L}} & -\overline{\overline{T}} \\ \overline{\overline{T}}^T & j\omega\overline{\overline{K}}^{-1} \end{bmatrix} \begin{bmatrix} \mathbf{I} \\ \mathbf{V} \end{bmatrix} = \begin{bmatrix} \mathbf{P} \\ \mathbf{S} \end{bmatrix}. \tag{5.15}$$

This equation can subsequently be solved by a direct or iterative solver. This matrix equation is only one possible variant of the augmented EFIE [7], [8]. By rescaling one or more equations and/or choosing another set of unknowns, e.g., charges instead of potentials, alternative formulations are obtained with varying properties. This way an EFIE devoid of low-frequency breakdown can be obtained down to very low frequencies when charge neutrality is enforced [8]. The question remains, however, how the introduction of the differential surface admittance matrix influences this desirable behavior. The frequency independent nature of its elements for large skin depths (and thus low frequencies), as shown in Fig. 4.7, seems promising in this regard but a full analysis for various materials and configurations is not included in this dissertation and is subject for future work.

At this point, however, (5.15) represents a set of separate objects residing in a background medium without any interconnection. In order to represent realistic structures, the various cuboids should be combined. We achieve this by introducing an infinitesimally small PEC wire connection between adjacent rectangles of two cuboids which equates the voltages of the adjacent rectangles and introduces an extra, yet *unknown* current flowing integrally from one rectangle to the other. This is implemented in the matrix system (5.15) by introducing an extra row with only two nonzero entries 1 and -1 to equate the voltages and an extra column with only two nonzero entries 1 and -1 to add the additional current to the two charge conservation equations of the involved rectangles.

5.3 Differential surface admittance operator for cuboids

In constructing the differential surface admittance operator, as defined in (3.51), the magnetic eigenfunctions of a cuboid cavity are required, which we present in the following subsection. The discretization of the operator is illustrated in Section 5.3.2 and can then be employed in either (5.6) or (5.15) to characterize interconnects.

5.3.1 Eigenfunctions of a cuboid cavity

Rectangular waveguide

We derive the eigenfunctions for the cuboid in the same way as we did for the cylinder: first we determine the eigenmodes for the rectangular waveguide. Afterwards we transform the waveguide into a cavity by terminating its ends with PEC plates. Thus, suppose that we have a rectangular waveguide with its cross-section in the xy-plane with dimensions l_x and l_y and its propagation direction aligned along the z-axis. Based on the derivation presented in Section 4.3.1, we find that the eigenmodes fall apart into two sets: TE and TM. By solving (4.13)–(4.14) with PEC boundary conditions through separation of variables and plugging the results in (4.15)–(4.18), we get the modal field distributions in the rectangle. For the TE modes, these are

$$h_{z,mn}(\boldsymbol{\rho}) = \cos(\lambda_x x)\cos\left(\lambda_y y\right) \tag{5.16}$$

$$\mathbf{e}_{t,mn}(\boldsymbol{\rho}) = \frac{j\omega\mu_0}{\lambda_x^2+\lambda_y^2}\left[\lambda_y \cos(\lambda_x x)\sin\left(\lambda_y y\right)\hat{\mathbf{x}} - \lambda_x \sin(\lambda_x x)\cos\left(\lambda_y y\right)\hat{\mathbf{y}}\right] \tag{5.17}$$

$$\mathbf{h}_{t,mn}(\boldsymbol{\rho}) = \frac{j\gamma_{mn}}{\lambda_x^2+\lambda_y^2}\left[\lambda_x \sin(\lambda_x x)\cos\left(\lambda_y y\right)\hat{\mathbf{x}} + \lambda_y \cos(\lambda_x x)\sin\left(\lambda_y y\right)\hat{\mathbf{y}}\right], \tag{5.18}$$

with $m \in \mathbb{N}$, $n \in \mathbb{N}$, $\gamma_{mn} = \sqrt{k^2-\lambda_x^2-\lambda_y^2}$, $\lambda_x = m\pi/l_x$ and $\lambda_y = n\pi/l_y$. For the TM modes, the modal field distributions satisfy

$$e_{z,mn}(\boldsymbol{\rho}) = \sin(\lambda_x x)\sin\left(\lambda_y y\right) \tag{5.19}$$

$$\mathbf{e}_{t,mn}(\boldsymbol{\rho}) = -\frac{j\gamma_{mn}}{\lambda_x^2+\lambda_y^2}\left[\lambda_x \cos(\lambda_x x)\sin\left(\lambda_y y\right)\hat{\mathbf{x}} + \lambda_y \sin(\lambda_x x)\cos\left(\lambda_y y\right)\hat{\mathbf{y}}\right] \tag{5.20}$$

$$\mathbf{h}_{t,mn}(\boldsymbol{\rho}) = \frac{j\omega\epsilon_0}{\lambda_x^2+\lambda_y^2}\left[\lambda_y \sin(\lambda_x x)\cos\left(\lambda_y y\right)\hat{\mathbf{x}} - \lambda_x \cos(\lambda_x x)\sin\left(\lambda_y y\right)\hat{\mathbf{y}}\right]. \tag{5.21}$$

Rectangular cavity

By substituting (5.16)–(5.18) and (5.19)–(5.21) into (4.25)–(4.26), we get the fields at any point in the waveguide. By placing PEC end caps at $z = 0$ and $z = l_z$, we obtain the cuboid resonator cavity. These boundary conditions lead to very similar restrictions as (4.29)–(4.30), viz.,

$$K_{mn}^{-} = -K_{mn}^{+} \tag{5.22}$$

$$\sin(\gamma_{mn} l_z) = 0. \tag{5.23}$$

Similar to the cylinder, these conditions force γ_{mn} to be $p\pi/l_z = \lambda_z$ with $p \in \mathbb{N}$. As such we find that the total modal field distribution at resonance frequencies for every mode is given by

$$\mathbf{e}_{mnp}(\mathbf{r}) = \mathbf{e}_{t,mn} \sin(\lambda_z z) + j e_{z,mn} \cos(\lambda_z z)\,\hat{\mathbf{z}} \tag{5.24}$$

$$\mathbf{h}_{mnp}(\mathbf{r}) = Z_c \mathbf{h}_{t,mn} \cos(\lambda_z z) - j Z_c h_{z,mn} \sin(\lambda_z z)\,\hat{\mathbf{z}}, \tag{5.25}$$

where we have normalized the expressions such that they satisfy (2.40).

Due to (5.23), the wavenumber can only take a discrete number of values. In contrast to the cylindrical cavity, the mode wavenumber is the same for both sets of modes:

$$k_{mnp}^2 = \lambda_x^2 + \lambda_y^2 + \lambda_z^2 = \left(\frac{m\pi}{l_x}\right)^2 + \left(\frac{n\pi}{l_y}\right)^2 + \left(\frac{p\pi}{l_z}\right)^2. \tag{5.26}$$

The TE modes satisfy the field distributions

$$\begin{aligned} \mathbf{e}_{mnp} = \;& k_{mnp}\lambda_y \cos(\lambda_x x) \sin\left(\lambda_y y\right) \sin(\lambda_z z)\,\hat{\mathbf{x}} \\ & - k_{mnp}\lambda_x \sin(\lambda_x x) \cos\left(\lambda_y y\right) \sin(\lambda_z z)\,\hat{\mathbf{y}} \end{aligned} \tag{5.27}$$

$$\begin{aligned} \mathbf{h}_{mnp} = \;& \lambda_z\lambda_x \sin(\lambda_x x) \cos\left(\lambda_y y\right) \cos(\lambda_z z)\,\hat{\mathbf{x}} \\ & + \lambda_z\lambda_y \cos(\lambda_x x) \sin\left(\lambda_y y\right) \cos(\lambda_z z)\,\hat{\mathbf{y}} \\ & - \left(\lambda_x^2 + \lambda_y^2\right) \cos(\lambda_x x) \cos\left(\lambda_y y\right) \sin(\lambda_z z)\,\hat{\mathbf{z}} \end{aligned} \tag{5.28}$$

Note that for $p = 0$ or $m = n = 0$, all field components vanish.

The TM eigenfunctions are given by

$$\begin{aligned} \mathbf{e}_{mnp} = \;& -\lambda_z\lambda_x \cos(\lambda_x x) \sin\left(\lambda_y y\right) \sin(\lambda_z z)\,\hat{\mathbf{x}} \\ & + \lambda_z\lambda_y \sin(\lambda_x x) \cos\left(\lambda_y y\right) \sin(\lambda_z z)\,\hat{\mathbf{y}} \\ & + \left(\lambda_x^2 + \lambda_y^2\right) \sin(\lambda_x x) \sin\left(\lambda_y y\right) \cos(\lambda_z z)\,\hat{\mathbf{z}} \end{aligned} \tag{5.29}$$

$$\begin{aligned} \mathbf{h}_{mnp} = \;& k_{mnp}\lambda_y \sin(\lambda_x x) \cos\left(\lambda_y y\right) \cos(\lambda_z z)\,\hat{\mathbf{x}}. \\ & - k_{mnp}\lambda_x \cos(\lambda_x x) \sin\left(\lambda_y y\right) \cos(\lambda_z z)\,\hat{\mathbf{y}} \end{aligned} \tag{5.30}$$

These modes vanish for $m = 0$ or $n = 0$.

The normalization factors $\mathcal{N}_\nu^2$ of both sets of eigenmodes are easily computed as the volume integral is separable in Cartesian coordinates [9]. For the TE modes this gives

$$\mathcal{N}_{mn0}^2 = \mathcal{N}_{00p}^2 = 0 \tag{5.31}$$

$$\mathcal{N}_{mnp}^2 = k_{mnp}^2 \frac{V}{2\varepsilon_m \varepsilon_n} \left(\lambda_x^2 + \lambda_y^2\right), \tag{5.32}$$

with $V = l_x l_y l_z$, i.e., the volume of the cuboid, while for the TM functions we find

$$\mathcal{N}_{0np}^2 = \mathcal{N}_{m0p}^2 = 0 \tag{5.33}$$

$$\mathcal{N}_{mnp}^2 = k_{mnp}^2 \frac{V}{4\varepsilon_p} \left(\lambda_x^2 + \lambda_y^2\right), \tag{5.34}$$

with ε_i the Neumann factor [9], which equals 1 for $i = 0$ and 2 otherwise.

5.3.2 Discretization

The expressions for the magnetic eigenmodes and their normalization factors suffice to construct the differential surface admittance operators for cuboids. However, when utilizing this operator in (5.6) or (5.15), we require the discretized version of (3.51). Analogous to the approach for the cylinder in Section 4.3.2, we expand the tangential electric field into basis functions and test the operator with the same set of functions to obtain

$$\overline{\overline{Y}}_{ij} = -\eta \sum_{m,n,p} \frac{\mathcal{K}_{mnp}}{\mathcal{N}_{mnp}^2} \int_{\mathcal{S}_j} \left(\hat{\mathbf{n}} \times \mathbf{h}_{mnp}\right) \cdot \mathbf{f}_j(\mathbf{r}) \, \mathrm{d}S \int_{\mathcal{S}_i} \left(\hat{\mathbf{n}} \times \mathbf{h}_{mnp}\right) \cdot \mathbf{f}_i(\mathbf{r}) \, \mathrm{d}S. \tag{5.35}$$

Note that in the calculation of each element, a triple infinite sum is present. In a numerical implementation, this summation is limited along its three dimensions. These maximum values are further denoted as (M, N, P). Moreover, we have to keep in mind that there exist two sets of magnetic eigenmodes, viz., TE and TM. For every value (m, n, p), there are thus two contributions to every matrix element.

The integrals to be evaluated in (5.35) can all be calculated analytically for the employed rooftops as they align along the same axes as the eigenmodes. This results in simple integrals of either trigonometric functions or the product of a first order polynomial and a (co)sine. All contributions to the $\overline{\overline{Y}}$ matrix can thus be computed exactly.

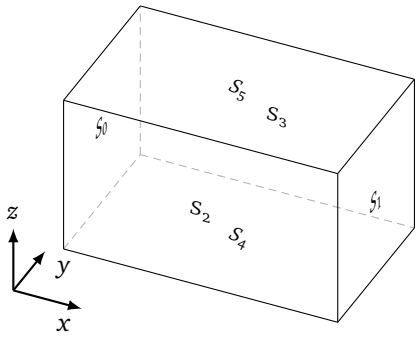

Figure 5.4: Illustration of the numbering convention of the different faces of a cuboid.

5.4 Revisited differential surface admittance operator

The calculation method for the differential surface admittance operator summarized in (5.35) enables the characterization of any nonmagnetic material for any frequency. However, as demonstrated in Section 4.5.1 for the cylinder, the method has a drawback: for good conductors, a considerable amount of eigenmodes is required to fully take the skin effect into account. Technically it is no problem to increase the number of eigenmodes but this does lengthen the computational time. This is why, in this section, we revisit the differential surface admittance operator for cuboids to obtain an expression for this operator that alleviates this problem. Initially, we present the operator for entire domain basis functions, leading to a sparse formulation in Section 5.4.1. Next we show in Section 5.4.2 that certain infinite sums in this sparse formulation have closed analytical expressions, improving the convergence behavior, especially for strongly developed skin effect phenomena. In the end in Section 5.4.3, we provide transformation matrices to switch back to local basis functions, enabling seamless inclusion into (5.6) or (5.15).

5.4.1 Expansion matrix

In (3.51), the eigenmodes themselves are actually not required but rather their tangential component on $\mathcal{S}$. Numbering the cuboid's six faces S_i from 0 to 5, corresponding to the outward-pointing normal vectors $(-\hat{\mathbf{x}}, \hat{\mathbf{x}}, -\hat{\mathbf{y}}, \hat{\mathbf{y}}, -\hat{\mathbf{z}}, \hat{\mathbf{z}})$, they are located at $x = 0, x = l_x, y = 0, y = l_y, z = 0$ and $z = l_z$, respectively as demonstrated in Fig. 5.4.

The rotated magnetic eigenmodes on S_0 are thus given by

$$\begin{aligned} S_0 : -\hat{\mathbf{x}} \times \mathbf{h}_{mnp} = &- \zeta_{y,mnp} \sin\left(\lambda_y y\right) \cos\left(\lambda_z z\right) \hat{\mathbf{z}} \\ &+ \zeta_{z,mnp} \sin\left(\lambda_z z\right) \cos\left(\lambda_y y\right) \hat{\mathbf{y}}, \end{aligned} \tag{5.36}$$

where we have introduced $\zeta_{\beta,mnp}$ as a placeholder for the pertinent factor of the β-component of either TE or TM modes, where β stands for x, y or z, and made

explicitly clear that they (can) depend on all three indices. Remark that $\zeta_{z,mnp}$ vanishes for TM modes. Careful inspection of the same quantity on the other sides of the cuboid shows that they all have the same form: each is composed of two terms along the two axes which comprise the face and, in turn, each term contains the product of a sine and cosine function. Furthermore, it turns out that the contribution along a particular axis shows a cosine dependence for the coordinate along that axis and a sine dependence along the remaining axis. In (5.36), for example, the first term oriented along $\hat{\mathbf{z}}$ has a $\cos(\lambda_z z)$ and a $\sin(\lambda_y y)$ dependence.

This observation prompts us to expand both $\mathbf{e}_0^t$ and $\mathbf{j}_s$ in similar functions, i.e., entire domain basis functions, on each face and exploit the orthogonality of the trigonometric functions. For example, the tangential electric field on S_0 is expanded as

$$S_0 : \mathbf{e}_0^t = \sum_{n',p'} \mathbf{e}_{0,n'p'} = \sum_{n',p'} \Big(a^0_{0,n'p'} \sin\left(\lambda'_y y\right) \cos\left(\lambda'_z z\right) \hat{\mathbf{z}} + a^1_{0,n'p'} \sin\left(\lambda'_z z\right) \cos\left(\lambda'_y y\right) \hat{\mathbf{y}} \Big), \tag{5.37}$$

with n' and p' being the two indices governing the expansion along the y- and z-axis, respectively, λ'_y and λ'_z fulfilling the same role as in (5.26) but for these primed indices n' and p', and $a^0_{0,n'p'}$ and $a^1_{0,n'p'}$ the unknown expansion coefficients on S_0 along its two axes.

For every term $\mathbf{e}_{0,n'p'}$, the integral in (3.51) can then be expressed as

$$\int_{S_0} \left(-\hat{\mathbf{x}} \times \mathbf{h}_{mnp}\right) \cdot \mathbf{e}_{0,n'p'} \, \mathrm{d}S = -\delta_{nn'} \delta_{pp'} \frac{A_0}{2} \left[a^0_{0,n'p'} \zeta_{y,mnp} \frac{\sigma_n}{\varepsilon_p} - a^1_{0,n'p'} \zeta_{z,mnp} \frac{\sigma_p}{\varepsilon_n} \right], \tag{5.38}$$

with σ_i zero for $i = 0$ and 1 otherwise, with A_0 the area of face S_0, and δ_{ij} the Kronecker delta. These Kronecker deltas imply that we can henceforth replace $\{n', p'\}$ by $\{n, p\}$. Focusing now, for illustration purposes, on the expansions coefficients $a^0_{0,np}$ along $\hat{\mathbf{z}}$ and plugging the results back into (3.51) gives

$$\mathbf{j}_s = \frac{-\eta A_0}{2} \sum_{n,p} \frac{\sigma_n}{\epsilon_p} \sum_m \frac{\mathcal{K}_{mnp}}{\mathcal{N}^2_{mnp}} a^0_{0,np} \zeta_{y,mnp} \left(\hat{\mathbf{n}} \times \mathbf{h}_{mnp}\right). \tag{5.39}$$

At this point, we can expand the surface current density on each face in exactly the same way as the tangential electric field. Illustrating this first for S_0, we get

$$S_0 : \mathbf{j}_s = \sum_{n'',p''} \mathbf{j}_{0,n''p''} = \sum_{n'',p''} \Big(b^0_{0,n''p''} \sin\left(\lambda''_y y\right) \cos\left(\lambda''_z z\right) \hat{\mathbf{z}} + b^1_{0,n''p''} \sin\left(\lambda''_z z\right) \cos\left(\lambda''_y y\right) \hat{\mathbf{y}} \Big), \tag{5.40}$$

where we have introduced the double primed indices n'' and p'' analogously to the primed ones in (5.37). Focusing again on a single component (along the z-axis)

and introducing the relevant term of $\hat{\mathbf{n}} \times \mathbf{h}_{mnp}$ on the same face, (5.39) yields

$$b^0_{0,n''p''} \sin\left(\lambda''_y y\right) \cos\left(\lambda''_z z\right) = \frac{\eta A_0}{2} \sum_{n,p} \frac{\sigma_n}{\epsilon_p} \sum_m \frac{\mathcal{K}_{mnp}}{\mathcal{N}^2_{mnp}} a^0_{0,np} \zeta^2_{y,mnp} \sin\left(\lambda_y y\right) \cos\left(\lambda_z z\right). \tag{5.41}$$

In order to isolate $b^0_{0,n''p''}$, we multiply both sides by $\sin\left(\lambda''_y y\right)\cos\left(\lambda''_z z\right)$ and integrate over S_0. This once again forces the (double) primed indices to take the same values as their nonprimed counterparts, leading to

$$b^0_{0,np} = \frac{A_0 \sigma_n}{2\epsilon_p} \left[\eta \sum_m \frac{\mathcal{K}_{mnp}}{\mathcal{N}^2_{mnp}} \zeta^2_{y,mnp} \right] a^0_{0,np}. \tag{5.42}$$

This equation fully captures the influence of a single $a^0_{0,np}$ component of the tangential electric field on its counterpart, i.e., the $b^0_{0,np}$ component of the surface current density. For the y-component of $\mathbf{j}_s$ in (5.40), we find a similar relation:

$$b^1_{0,np} = \frac{A_0 \sigma_n}{2\epsilon_p} \left[-\eta \sum_m \frac{\mathcal{K}_{mnp}}{\mathcal{N}^2_{mnp}} \zeta_{y,mnp} \zeta_{z,mnp} \right] a^0_{0,np}. \tag{5.43}$$

The same procedure can now be repeated for the other five faces to fully determine the impact that this one component of the expanded tangential electric field has on the surface current densities on all faces. We will pick a few of these components to showcase their most important characteristics.

First, a closer look at the opposite face, i.e., S_1, shows that the rotated magnetic eigenmode and surface current density are given by

$$\begin{aligned} S_1 : \hat{\mathbf{x}} \times \mathbf{h}_{mnp} = &+ \zeta_{y,mnp} (-1)^m \sin\left(\lambda_y y\right) \cos\left(\lambda_z z\right) \hat{\mathbf{z}} \\ &- \zeta_{z,mnp} (-1)^m \sin\left(\lambda_z z\right) \cos\left(\lambda_y y\right) \hat{\mathbf{y}}, \end{aligned} \tag{5.44}$$

$$\begin{aligned} S_1 : \mathbf{j}_s = \sum_{n'',p''} \mathbf{j}_{1,n''p''} = &\sum_{n'',p''} b^0_{1,n''p''} \sin\left(\lambda''_y y\right) \cos\left(\lambda''_z z\right) \hat{\mathbf{z}} \\ &+ b^1_{1,n''p''} \sin\left(\lambda''_z z\right) \cos\left(\lambda''_y y\right) \hat{\mathbf{y}}. \end{aligned} \tag{5.45}$$

Following the same reasoning as outlined above, we thus find the following relation between $a^0_{0,np}$ and $b^0_{1,np}$:

$$b^0_{1,np} = \frac{A_0 \sigma_n}{2\epsilon_p} s \left[-\eta \sum_m \frac{\mathcal{K}_{mnp}}{\mathcal{N}^2_{mnp}} (-1)^m \zeta^2_{y,mnp} \right] a^0_{0,np}, \tag{5.46}$$

while for $b^1_{1,np}$ we get

$$b^1_{1,np} = \frac{A_0 \sigma_n}{2\epsilon_p} \left[\eta \sum_m \frac{\mathcal{K}_{mnp}}{\mathcal{N}^2_{mnp}} (-1)^m \zeta_{y,mnp} \zeta_{z,mnp} \right] a^0_{0,np}. \tag{5.47}$$

We immediately see that (5.46) and (5.47) are very similar to (5.42) and (5.43), respectively; the only difference is a minus sign and the factor $(-1)^m$ in the summation.

Next, we observe the influence on a perpendicular face, e.g., S_2. Here, the rotated magnetic eigenmodes and the expansion of $\mathbf{j}_s$ are given by

$$\begin{aligned} S_2 : -\hat{\mathbf{y}} \times \mathbf{h}_{mnp} = &- \zeta_{z,mnp} \sin(\lambda_z z) \cos(\lambda_x x)\, \hat{\mathbf{x}} \\ &+ \zeta_{x,mnp} \sin(\lambda_x x) \cos(\lambda_z z)\, \hat{\mathbf{z}}, \end{aligned} \tag{5.48}$$

$$\begin{aligned} S_2 : \mathbf{j}_s = \sum_{p'',m''} \mathbf{j}_{2,p''m''} = \sum_{p'',m''} & b^0_{2,p''m''} \sin\left(\lambda''_z z\right) \cos\left(\lambda''_x x\right) \hat{\mathbf{x}} \\ &+ b^1_{2,p''m''} \sin\left(\lambda''_x x\right) \cos\left(\lambda''_z z\right) \hat{\mathbf{z}}. \end{aligned} \tag{5.49}$$

Substituting these in (5.39) and selecting the component along the x-axis, we obtain the equivalent of (5.41) as

$$\begin{aligned} & b^0_{2,p''m''} \sin\left(\lambda''_z z\right) \cos\left(\lambda''_x x\right) = \\ & \frac{\eta A_0}{2} \sum_{n,p} \frac{\sigma_n}{\epsilon_p} \sum_m \frac{\mathcal{K}_{mnp}}{\mathcal{N}^2_{mnp}} a^0_{0,np} \zeta_{y,mnp} \zeta_{z,mnp} \sin(\lambda_z z) \cos(\lambda_x x). \end{aligned} \tag{5.50}$$

Employing a similar projection to isolate $b^0_{2,p''m''}$ as before, the double primed indices collapse onto their nonprimed equivalents. This time, however, these indices, i.e., m and p, do not correspond (completely) with the indices of $a^0_{0,np}$, i.e., n and p. As such, this projection enforces an extra condition on the index m and the summation, as found for example in (5.42), over m vanishes, leading to:

$$b^0_{2,pm} = \frac{A_0}{2} \sum_n \frac{\sigma_n}{\epsilon_p} \left[\eta \frac{\mathcal{K}_{mnp}}{\mathcal{N}^2_{mnp}} \zeta_{y,mnp} \zeta_{z,mnp} \right] a^0_{0,np}. \tag{5.51}$$

For all other surface current density expansion coefficients one finds similar results. In short, we can write the relation between $a^0_{0,np}$ and any other nonzero expansion coefficient $b^j_{i,mnp}$ on face S_i along its first ($j = 0$) or second axis ($j = 1$) as

$$b^j_{i,mnp} = \Omega^j_{i,mnp} \left(\frac{A_0}{2} \frac{\sigma_n}{\epsilon_p} \right) a^0_{0,np}, \tag{5.52}$$

for the same face S_0 and the opposite face S_1, where $\Omega^j_{i,mnp}$ evaluates to a single infinite sum (as for example shown in (5.42) and (5.46)) and to

$$b^j_{i,mnp} = \sum_{n \text{ or } p} \Upsilon^j_{i,mnp} \left(\frac{A_0}{2} \frac{\sigma_n}{\epsilon_p} \right) a^0_{0,np}, \tag{5.53}$$

for the remaining faces where the summation runs over n for S_2 and S_3 and over p for S_4 and S_5. Note, however, that $\Upsilon^j_{i,mnp}$ is a known scalar (as, e.g., for S_2 in (5.51)). Note as well that the bracketed term is independent of either i or j and only linked to the face and direction of $a^0_{0,np}$.

At this point, we have fully described the relation between one set of electric field expansion coefficients on S_0 and all relevant current density coefficients on all faces. The same approach can now be repeated for all the other faces and directions to obtain a complete global relation between all expansion coefficients of both quantities. Clearly, the results are the same as described above apart from the required cyclic permutation of the axes and the employed indices. In summary, when we collect all coefficients into the vectors $\mathbf{a}_c$ and $\mathbf{b}_c$, we get

$$\mathbf{b}_c = \overline{\overline{Y}}_c\, \mathbf{a}_c = \overline{\overline{X}}\,\overline{\overline{D}}\mathbf{a}_c, \tag{5.54}$$

with the expansion matrix $\overline{\overline{X}}$ being a sparse matrix whose nonzero entries are the — still to be evaluated — $\Omega^j_{i,mnp}$ and the already known scalar values $\Upsilon^j_{i,mnp}$, and where $\overline{\overline{D}}$ is a diagonal matrix with elements similar to the bracketed term in (5.52) and (5.53).

5.4.2 Explicit analytic expressions

Although all elements in $\overline{\overline{Y}}_c$ (or in particular in $\overline{\overline{X}}$) are theoretically fully defined, the infinite sum that still appears in $\Omega^j_{i,mnp}$ poses a computational challenge. However, we will now show that this sum possesses a closed analytical form, as such avoiding a cut-off of the sum and the corresponding loss in accuracy in the actual implementation, especially at high frequencies when accurate skin effect modeling is imperative.

As a first example, we examine the $\Omega^j_{i,mnp}$ values for (5.42). Adding up the contributions from both the TE and TM modes, we get

$$\Omega^j_{i,mnp} = \frac{4\eta}{V}\sigma_n \left[\sum_{m=0}^{\infty} \frac{\epsilon_m \lambda_y^2 \lambda_z^2}{\left(k^2 - k_{mnp}^2\right)\left(k_0^2 - k_{mnp}^2\right)\left(\lambda_x^2 + \lambda_y^2\right)} + \epsilon_p \sum_{m=1}^{\infty} \frac{k_{mnp}^2 \lambda_x^2}{\left(k^2 - k_{mnp}^2\right)\left(k_0^2 - k_{mnp}^2\right)\left(\lambda_x^2 + \lambda_y^2\right)} \right]. \tag{5.55}$$

By extracting the $m = 0$ term of the first sum and recombining both fractions using the following substitutions:

$$\alpha = \frac{l_x}{\pi}\alpha' = \frac{l_x}{\pi}\sqrt{k^2 - \lambda_y^2 - \lambda_z^2} \tag{5.56}$$

$$\alpha_0 = \frac{l_x}{\pi}\alpha_0' = \frac{l_x}{\pi}\sqrt{k_0^2 - \lambda_y^2 - \lambda_z^2} \tag{5.57}$$

$$\theta = \frac{l_x}{\pi}\lambda_y = nl_x/l_y \qquad\qquad \vartheta = \frac{l_x}{\pi}\lambda_z = pl_x/l_z \tag{5.58}$$

we get the following expression for (5.55)

$$\Omega^j_{i,mnp} = \frac{4\eta}{V}\sigma_n\frac{l_x^2}{\pi^2}\left[\vartheta^2\left(\frac{1}{\alpha^2\alpha_0^2} + 2\sum_{m=1}^{\infty}\frac{1}{(m^2-\alpha^2)\left(m^2-\alpha_0^2\right)}\right) + \epsilon_p\sum_{m=1}^{\infty}\frac{m^2}{(m^2-\alpha^2)\left(m^2-\alpha_0^2\right)}\right]. \tag{5.59}$$

The sums in this expression have closed analytical forms as outlined in Appendix C:

$$\Omega^j_{i,mnp} = \frac{4\eta}{V}\sigma_n\frac{l_x^2}{\pi^2}\left[2\vartheta^2\Omega_0(\alpha,\alpha_0) + \epsilon_p\Omega_2(\alpha,\alpha_0)\right]. \tag{5.60}$$

$$= -\frac{2\sigma_n\epsilon_p l_x}{j\omega\mu_0 V}\left[\frac{k^2-\lambda_y^2}{\alpha'}\cot(\pi\alpha) - \frac{k_0^2-\lambda_y^2}{\alpha_0'}\cot(\pi\alpha_0)\right] \tag{5.61}$$

Second, the same procedure is applied to the sum in (5.43). In this case, the TM contribution vanishes as $\zeta_z^{\mathrm{TM}} \equiv 0$, yielding

$$\Omega^j_{i,mnp} = -\frac{4\eta}{V}\sum_{m=0}^{\infty}\frac{\epsilon_m\lambda_y\lambda_z}{\left(k^2-k_{mnp}^2\right)\left(k_0^2-k_{mnp}^2\right)}$$

$$= -\frac{4\eta}{V}\frac{l_x^2}{\pi^2}\theta\vartheta\left[2\Omega_0(\alpha,\alpha_0)\right] \tag{5.62}$$

$$= \frac{4l_x}{j\omega\mu_0 V}\lambda_y\lambda_z\left[\frac{1}{\alpha'}\cot(\pi\alpha) - \frac{1}{\alpha_0'}\cot(\pi\alpha_0)\right] \tag{5.63}$$

Third, as observed before (see (5.46) and (5.47)), very similar sums appear for parallel, non-coinciding planes. For example, the $\Omega^j_{i,mnp}$ value in (5.47) becomes:

$$\Omega^j_{i,mnp} = \frac{4\eta}{V}\sum_{m=0}^{\infty}\frac{\epsilon_m(-1)^m\lambda_y\lambda_z}{\left(k^2-k_{mnp}^2\right)\left(k_0^2-k_{mnp}^2\right)}$$

$$= \frac{4\eta}{V}\frac{l_x^2}{\pi^2}\theta\vartheta\left[2\Psi_0(\alpha,\alpha_0)\right], \tag{5.64}$$

$$= -\frac{4l_x}{j\omega\mu_0 V}\lambda_y\lambda_z\left[\frac{1}{\alpha'}\csc(\pi\alpha) - \frac{1}{\alpha_0'}\csc(\pi\alpha_0)\right] \tag{5.65}$$

where we observe that the only difference with (5.62) is a minus sign and another type of auxiliary function, i.e., $\Psi_n(\cdot,\cdot)$ instead of $\Omega_n(\cdot,\cdot)$, to account for the $(-1)^m$ factor in the sum.

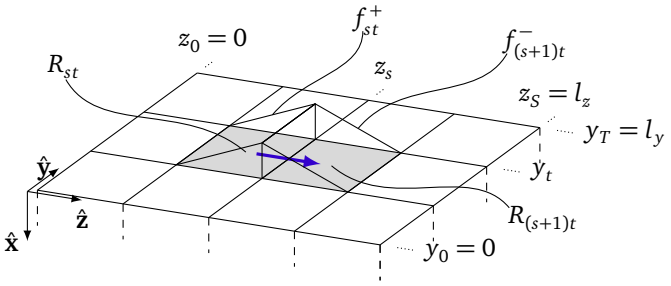

Figure 5.5: Definition of a rooftop along $\hat{\mathbf{z}}$ on face S_0.

Above, we have demonstrated the existence of closed-form expressions for some specific examples. The same procedure is followed for all other expansion coefficients and, as expected from the symmetry of the problem, the resulting expressions are all of the same form provided that the correct cyclic permutation of the axes and indices is performed. At this point, it is important to stress that $\overline{\overline{Y}}_c$ in (5.54) is free from infinite sums and, thus, efficiently and accurately maps the expansions coefficients $\mathbf{a}_c$ onto $\mathbf{b}_c$.

5.4.3 Discretized $\mathcal{Y}$-operator for a cuboid

In Section 5.4.1 we derived an analytical form of the differential surface admittance operator for a cuboid based on entire domain basis functions. In order to integrate it into (5.6) or (5.15), we need to convert to and from the rooftops employed to discretize the surface of the cuboid(s) [10]. Restricting ourselves once more to S_0 and the $\hat{\mathbf{z}}$-component on this face, we expand $e_z = \mathbf{e} \cdot \hat{\mathbf{z}}$ as

$$S_0 : e_z = \sum_{s=1}^{S} \sum_{t=1}^{T} A_{0,st}^{0} f_{st}^{+} + A_{0,(s-1)t}^{0} f_{st}^{-}, \tag{5.66}$$

with S and T the number of divisions along $\hat{\mathbf{z}}$ and $\hat{\mathbf{y}}$, respectively. The positive and negative half-rooftop functions f_{st}^{+} and f_{st}^{-}, as illustrated in Fig. 5.5, are defined as

$$f_{st}^{+} = \frac{z - z_{s-1}}{\Delta z \Delta y}, \qquad \{y, z\} \in R_{st} \tag{5.67}$$

$$f_{st}^{-} = \frac{z_s - z}{\Delta z \Delta y}, \qquad \{y, z\} \in R_{st}, \tag{5.68}$$

with R_{st} the rectangle that supports the half-rooftop function (see Fig. 5.5) and Δz and Δy its length along the z- and y-axis, respectively. This expansion should equal the z-component of (5.37):

$$S_0 : e_z = \sum_{n',p'} a_{0,n'p'}^{0} \sin\left(\lambda_y' y\right) \cos\left(\lambda_z' z\right) \tag{5.69}$$

To connect expansions (5.66) and (5.69), we project them both onto the entire domain basis function $\sin\left(\lambda_y y\right)\cos\left(\lambda_z z\right)\hat{\mathbf{z}}$. For (5.69), the resulting integral resembles (5.38) and results in $a^0_{0,np}A_0\sigma_n/(2\varepsilon_p)$. For (5.66), one gets,

$$\sum_{s=1}^{S}\sum_{t=1}^{T}A^0_{0,st}I^+_{st}+A^0_{0,(s-1)t}I^-_{st}, \tag{5.70}$$

with

$$I^{\pm}_{st}=\int_{R_{st}}f^{\pm}_{st}\sin\left(\lambda_y y\right)\cos\left(\lambda_z z\right)\,\mathrm{d}S=\phi_y\phi^{\pm}_z, \tag{5.71}$$

and

$$\phi_y=\frac{-1}{\Delta y\lambda_y}\left[\cos\left(\lambda_y y_t\right)-\cos\left(\lambda_y y_{t-1}\right)\right] \tag{5.72}$$

$$\phi^+_z=\frac{\sin\left(\lambda_z z_s\right)}{\lambda_z}+\frac{\cos\left(\lambda_z z_s\right)-\cos\left(\lambda_z z_{s-1}\right)}{\lambda^2_z\Delta z} \tag{5.73}$$

$$\phi^-_z=-\frac{\sin\left(\lambda_z z_{s-1}\right)}{\lambda_z}-\frac{\cos\left(\lambda_z z_s\right)-\cos\left(\lambda_z z_{s-1}\right)}{\lambda^2_z\Delta z}. \tag{5.74}$$

When we generalize the results obtained above to all directions and faces and collect all rooftop basis function expansion coefficients (of the type $A^0_{0,st}$ in (5.66)) into the vector $\mathbf{E}$, we get the following relation:

$$\overline{\overline{M}}\mathbf{E}=\overline{\overline{D}}\mathbf{a}_c, \tag{5.75}$$

where the matrix $\overline{\overline{M}}$ links the rooftop and trigonometric functions via expression of the type (5.70) and the previously introduced diagonal scaling matrix $\overline{\overline{D}}$ (see (5.54)) is present on the right-hand side.

For the surface current density, we start with similar expansions:

$$S_0: j_{s,z}=\sum_{s=1}^{S}\sum_{t=1}^{T}B^0_{0,st}f^+_{st}+B^0_{0,(s-1)t}f^-_{st}, \tag{5.76}$$

$$S_0: j_{s,z}=\sum_{n'',p''}b^0_{0,n''p''}\sin\left(\lambda''_y y\right)\cos\left(\lambda''_z z\right), \tag{5.77}$$

which we now project onto rooftop testing functions $\mathbf{f}_{s't'}=\left[f^+_{s't'}+f^-_{s't'}\right]\hat{\mathbf{z}}$. For (5.77) this results in an integral of the same form as in (5.71) thus giving the following result for this procedure:

$$\overline{\overline{M}}^T\mathbf{b}_c. \tag{5.78}$$

Projecting (5.76) onto rooftops, results in the Gram matrix $\overline{\overline{G}}$. As mentioned before (see (5.2)) only three elements per row/column are nonzero in $\overline{\overline{G}}$: two entries for

partially overlapping rooftops and one for the self-interaction. Therefore, only two distinct integrals are required (with $A_{R_{st}}$ being the area of R_{st}):

$$\int_{R_{st}} f_{st}^{+} f_{st}^{+} \,\mathrm{d}S = \int_{R_{st}} f_{st}^{-} f_{st}^{-} \,\mathrm{d}S = \frac{A_{R_{st}}}{3(\Delta y)^2}, \tag{5.79}$$

$$\int_{R_{st}} f_{st}^{+} f_{s(t-1)}^{-} \,\mathrm{d}S = \frac{A_{R_{st}}}{6(\Delta y)^2}. \tag{5.80}$$

Consequently, the relation between both expansions of $\mathbf{j}_s$ is

$$\overline{\overline{G}}\mathbf{I} = \overline{\overline{M}}^{T} \mathbf{b}_c, \tag{5.81}$$

where $\mathbf{I}$ collects all rooftop function expansion coefficients (of the type $B^0_{0,st}$ in (5.76)) of $\mathbf{j}_s$. Combining (5.75) and (5.81) together with (5.54), finally yields

$$\mathbf{I} = \overline{\overline{G}}^{-1} \overline{\overline{M}}^{T} \overline{\overline{Y}}_c \overline{\overline{D}}^{-1} \overline{\overline{M}}\mathbf{E} \tag{5.82}$$

$$= \overline{\overline{G}}^{-1} \left(\overline{\overline{M}}^{T} \overline{\overline{X}} \overline{\overline{M}} \right) \mathbf{E} \tag{5.83}$$

$$= \overline{\overline{G}}^{-1} \overline{\overline{Y}} \mathbf{E}, \tag{5.84}$$

with $\overline{\overline{Y}}$ now being the discrete version of (3.51). The entire procedure leading to (5.84) has been schematically summarized in Fig. 5.6. We conclude this section with some remarks about $\overline{\overline{Y}}$. All material properties and frequency dependencies are encapsulated in $\overline{\overline{X}}$. This implies that the calculation of the total matrix for various frequencies and/or materials only calls for separate instances of $\overline{\overline{X}}$ while $\overline{\overline{M}}$ can be reused. Similarly, all the mesh information is captured by $\overline{\overline{M}}$. The size of $\overline{\overline{X}}$ (and thus of $\overline{\overline{M}}$) depends on the number of entire domain basis functions that are taken into account.

5.5 Examples

In this chapter, we have defined two matrix equations to jointly solve the exterior and interior problem. At the same time, we have provided two distinct ways to compute the differential surface admittance operator for cuboids. For the remainder of this chapter, *Method 1* will denote the combination of (5.6) and (5.35), i.e., the equivalent circuit interpretation combined with the original differential surface admittance matrix formulation solved by a circuit solver. *Method 2*, on the other hand, utilizes the set of matrix equations (5.15) in conjunction with the revisited differential surface admittance operator (5.84) solved through conventional matrix solvers. *Method 3* obtains full-wave results by using the set of matrix equations (5.15) but combined with the original differential surface admittance operator (5.35) and will be employed in a comparison between both $\overline{\overline{Y}}$-matrix calculation methods.

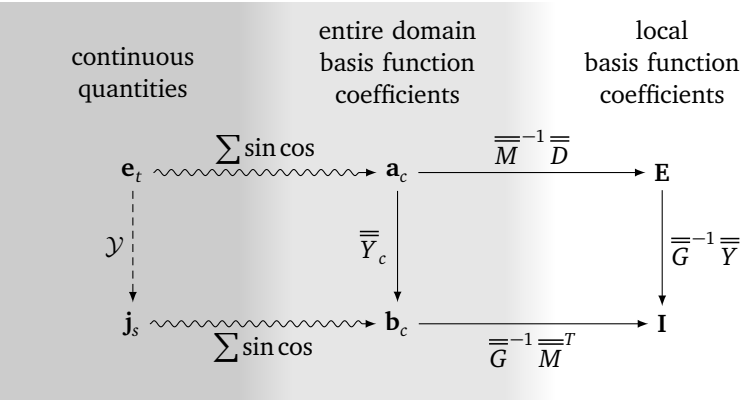

Figure 5.6: Schematic overview of the discretization procedure.

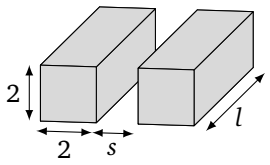

Figure 5.7: Two parallel copper conductors with cross-section 2 mm × 2 mm, length l and separation s.

5.5.1 Validation examples

Two parallel copper conductors

As a first example, we consider two parallel copper conductors ($\sigma = 5.6 \cdot 10^7$ S/m), both with a rectangular cross-section of 2 mm × 2 mm, varying length l and separation distance s as shown in Fig. 5.7 (all dimensions are given in mm). This configuration is a 3-D version of the second example of Fig. 9 in [11]. The resistance and inductance per unit of length (p.u.l.) are calculated through Method 1 by diving the total resistance/inductance by the length l. The resistance per meter is shown in Fig. 5.8(a). The low-frequency value is the same for all configurations and corresponds to the DC value obtained by Pouillet's law. For increasing frequencies the resistance for the various separations starts to fan out due to the proximity effect, which is strongest for the smallest spacing. (Results from [11] are not shown on the figure since the near-perfect agreement clutters the graph.) The corresponding inductance per unit of length is depicted in Fig. 5.8(b). Here we observe that both parameters have a much stronger influence on the results. A considerable length is required to evolve towards the pure 2-D results, especially for the low-frequency limit.

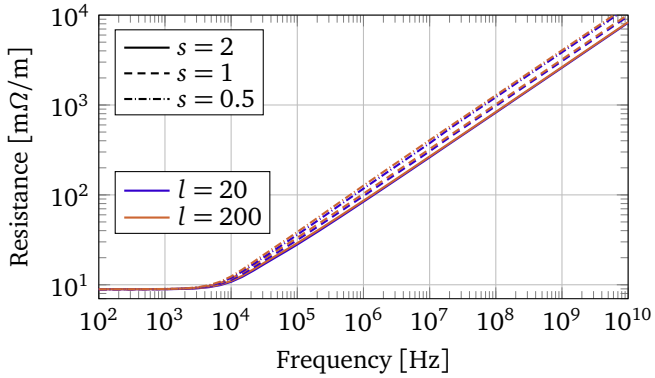

(a) Resistance in mΩ/m.

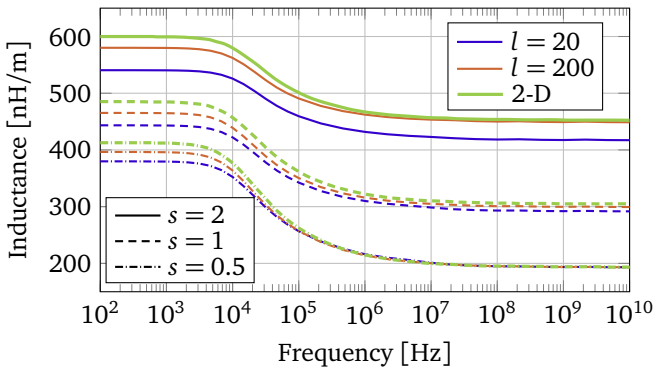

(b) Inductance in nH/m.

Figure 5.8: Resistance and inductance of the structure shown in Fig. 5.7 for various separations s and lengths l. The 2-D reference solution is obtained through the technique described in [11]. All dimensions are given in millimeter.

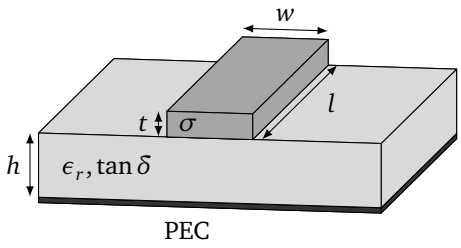

Figure 5.9: Microstrip configuration on a RO4350B RF substrate ($\epsilon_r = 3.48, \tan\delta = 0.003$, $w = 530\,\mu$m, $t = 35\,\mu$m, $h = 250\,\mu$m, $l = 10$ mm, $\sigma = 5.8 \cdot 10^7$ S/m).

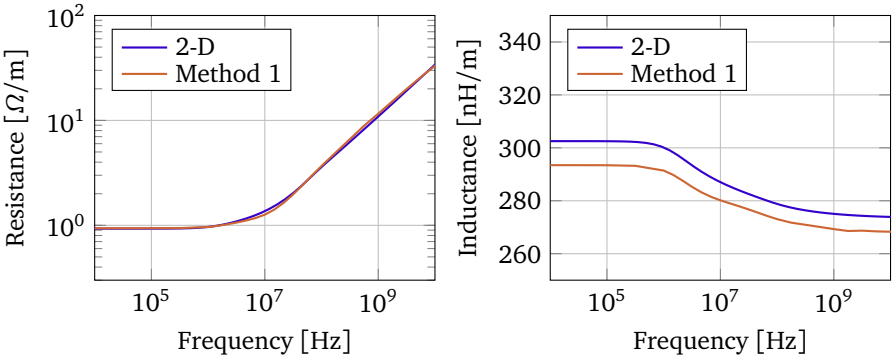

(a) P.u.l. resistance in Ω/m.

(b) P.u.l. inductance in nH/m.

Figure 5.10: P.u.l. resistance and inductance of the microstrip shown in Fig. 5.9. The 2-D reference result is calculated through the method reported in [12].

Microstrip

Consider, as a second example characterized with Method 1, a PCB microstrip configuration as presented in Fig. 5.9. A copper conductor ($\sigma = 5.8 \cdot 10^7$S/m) and a perfect electric ground plane are placed on either sides of a RO4350B substrate ($\epsilon_r = 3.48$, $\tan\delta = 0.003$). The height of this substrate is $h = 250\,\mu$m while the dimensions of the strip are $530\,\mu\text{m} \times 35\,\mu\text{m} \times 10\,\text{mm}$.

The resistance p.u.l. , simply obtained by dividing the total resistance of the strip by its finite length l, is shown in Fig. 5.10(a) together with a 2-D reference solution obtained through the technique described in [12]. The low-frequency value converges to the Pouillet value while we clearly see the influence of the skin effect for increasing frequencies. Furthermore, we observe an excellent agreement between the 2-D results and our proposed method.

In Fig. 5.10(b) the inductance per unit of length is plotted for both methods. For this characteristic we observe a much stronger influence of the finite length of the microstrip. The difference between the curves is strongest for the low-frequency inductance where we observe a difference of 3 % between both results. However, tests have shown that increasing the length of the microstrip raises the curve towards the 2-D result, as expected.

Right-angled corner

The two previous examples are essentially 2-D problems and as such do not fully take advantage of the possibilities of the techniques presented in this chapter. Thereto, our third example to be solved with Method 1 is a copper ($\sigma = 5.6 \cdot 10^7$ S/m) right-angled corner as shown in Fig. 5.11(a). The height h and width a

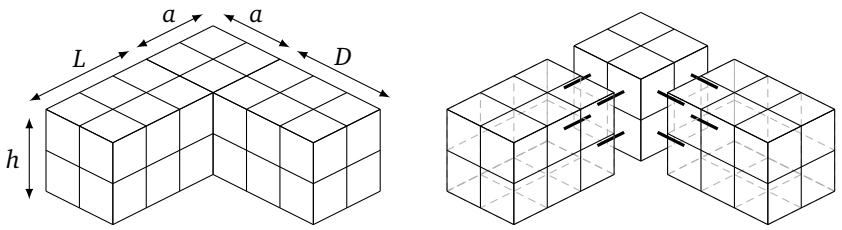

(a) Geometry of the right-angled corner. (b) Connection between the different cuboids.

Figure 5.11: Geometry of the right-angled corner with fixed dimensions $h = a = 2\,\text{mm}$ and variable lengths L and D. The second figure shows the details of the connection between the different cuboids that make up the total structure.

are set to 2 mm while L and D, the lengths of both arms, are varied. Figure 5.11(b) illustrates the subdivision of the structure: the corner is divided into three distinct cuboids which are placed next to each other. The actual connection between two blocks is provided by a wire between two adjacent rectangles (or equivalently voltage nodes) on both cuboids, implemented in the equivalent circuit by a short circuit between the two voltage nodes. This ensures that the current flows uninhibited from one cuboid to the other without changing direction or phase. The resistance was computed not only for the right-angled corner but also for a single straight cuboid with the combined length of both arms and the corner block, i.e., $L + a + D$ such that the volume of both topologies is the same. In Fig. 5.12, the resistance is shown for two different configurations. For the lower frequencies we observe that the corner has a lower resistance than the corresponding cuboid in both cases. This DC value has been verified with a finite difference method (FDM) program, solving Laplace's problem, and demonstrates perfect agreement (shown with markers on the y-axis). At the same time, the results for the single straight cuboids coincide with the Pouillet value. When the frequency is raised, the proximity effect causes the resistance of the corners to start increasing earlier, resulting in a crossover of the curves and eventually a higher resistance for the corner.

Fringing effect

So far we have solved problems with Method 1; a formulation which does not take capacitance effects into account. By utilizing Method 2, on the other hand, all contributions of the Green's function are taken into account, leading to a full electromagnetic characterization. As a first example, consider the geometry depicted in Fig. 5.13. A copper plate ($\sigma = 5.8 \cdot 10^7\,\text{S/m}$) of dimension $l \times w$ with a thickness of $1\,\mu\text{m}$ is fed by a stub of $20\,\mu\text{m} \times 5\,\mu\text{m}$ and suspended $2.5\,\mu\text{m}$ above a PEC ground plane. Initially we choose $l = w = 50\,\mu\text{m}$ and use the simple parallel plate formula ($C_{\text{pp}} = \epsilon A/d$) for both cuboids to estimate the total capacitance of this structure (see Table 5.1). However, this ignores the fringing fields and will

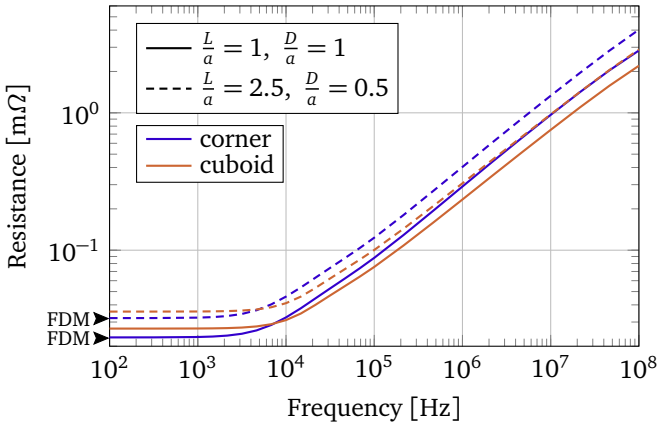

Figure 5.12: Resistance of a copper, right-angled corner in mΩ, compared to a cuboid with the same total volume, for various configurations as a function of frequency with $h = a = 2\,\text{mm}$. The markers on the left indicate the DC resistance as obtained through a FDM.

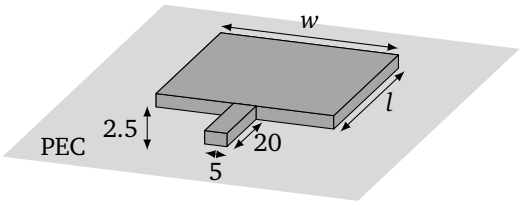

Figure 5.13: Copper plate ($\sigma = 5.8 \cdot 10^7\,\text{S/m}$) with a feed stub above a PEC half-space. The thickness of the conductor is $1\,\mu$m. All other dimensions are given in μm on the figure.

as such underestimate the true capacitance. Various analytical expressions to estimate this effect can be found for 2-D and 3-D capacitors. We will employ the simple expressions for 2-D conductors with a finite thickness as found in [13] and apply them along two dimensions for an improved estimation. All results are collected in Table 5.1. It is apparent that the parallel plate formula severely underestimates the total capacitance. Employing the analytical formulas results in a 30 % increase while our full-wave solution computes a capacitance that is 37 % larger. The additional increase found with the integral equation solution is due to the corners and the connection of both blocks.

According to the parallel plate formula, the capacitance only depends on the area of the plate and not on its shape. However, the analytical formulas contradict this and suggest that fringing effects do depend on the exact shape. Therefore, we investigate configurations with the same, fixed area for various aspect ratios $\alpha = l/w$. The difference between the calculated and nominal capacitance of 9.208 fF is characterized by the fringing factor γ such that $C = \gamma\, C_{\text{pp}}$. For some specific values of α the capacitances are included in Table 5.1. From Fig. 5.14 we see that

Table 5.1: Capacitance in fF of the structure in Fig. 5.13

l [μm]	w [μm]	$\alpha = l/w$	C_{pp}	Yuan/Trick [13]	Method 2
50	50	1	9.208	12.035	12.647
111.80	22.36	5	9.208	12.742	13.524
22.36	111.80	0.2	9.208	12.742	13.462

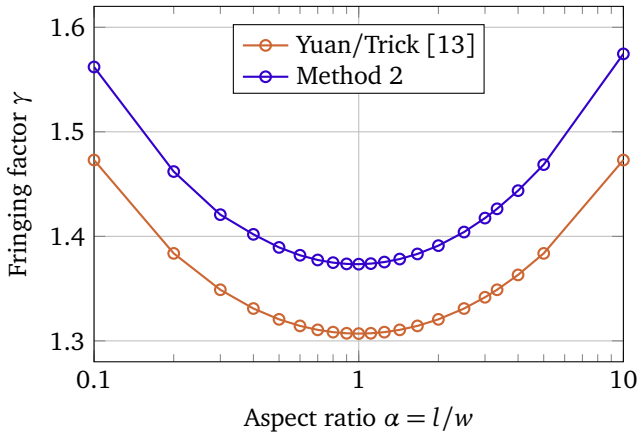

Figure 5.14: Fringing factor γ for various aspect ratios $\alpha = l/w$.

γ is minimum for a square plate and increases the more the plate is elongated in either direction. Note as well that the capacitance for reciprocal aspect ratios is slightly different according to the simulation results. Two such values are included in Table 5.1 and show that for *longer* plates the capacitance is marginally larger than for *wider* plates. This phenomenon can be attributed to the feed stub, which is aligned along the length of the plate, and a such introduces a small asymmetry.

Gap capacitance

For the second example solved with Method 2, we examine a structure that exhibits both capacitive and inductive behavior. The example constitutes a simple structure consisting of two copper ($\sigma = 5.8{\cdot}10^7$ S/m) blocks with dimensions 2 mm×2 mm× 20 mm. This example is not only used to further validate Method 2, but it is also employed to compare the revisited $\overline{\overline{Y}}$, cf. (5.84), with the initial formulation, i.e., (5.35) employed in Method 3, in terms of accuracy, computation time and memory requirement.

Focusing on the electrical performance of the structure first, we calculate its impedance by measuring the voltage over the terminals where a unit current source connects to the copper blocks. The magnitude of this impedance is shown in Fig. 5.16 for

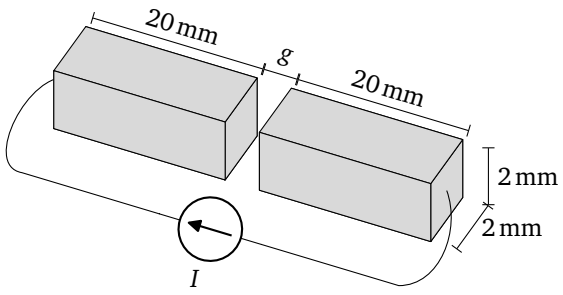

Figure 5.15: Two copper blocks (2 mm × 2 mm × 20 mm) separated by a variable distance g.

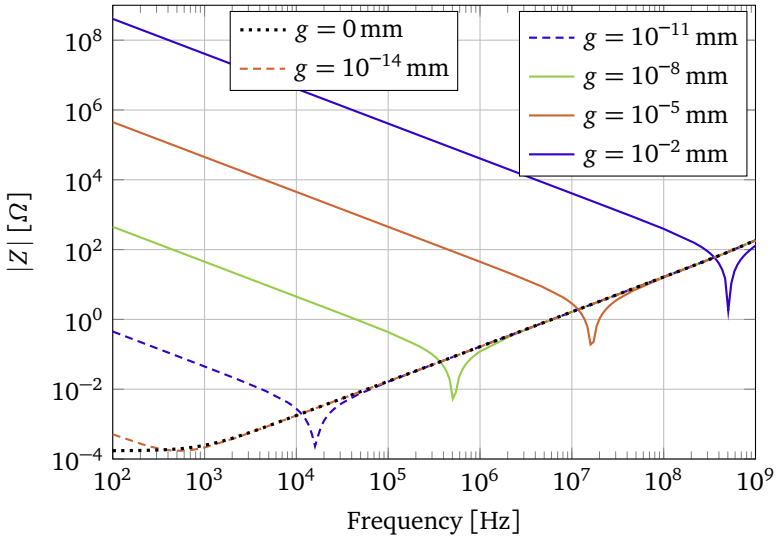

Figure 5.16: Magnitude of the total impedance of the two copper blocks shown in Fig. 5.15 as a function of frequency for various separation distances g.

various values of the gap g. The black dotted line, i.e., for $g = 0$ mm, corresponds to one single copper block of length 40 mm and is included as a reference result for the limit $g \to 0$.

For all nonzero values of g, a series resonance occurs due to the interplay of the inductance, which is the same for all configurations, and the capacitance of the gap, which decreases for increasing distances as such pushing the resonance frequency to higher values. Once beyond its self-resonance, the inductive behavior dominates and the impedance response coincides with the reference results regardless of the separation distance.

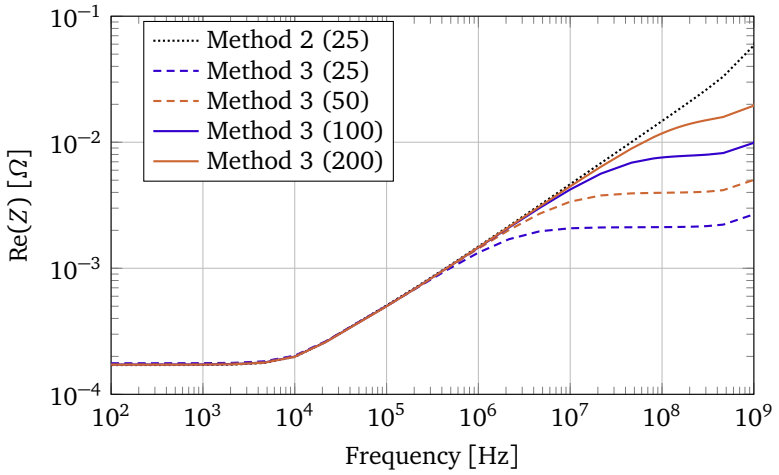

Figure 5.17: Real part of the impedance for two copper blocks (see Fig. 5.15) as a function of frequency with $g = 1\,\mu$m for Method 2 and Method 3. The number of entire domain basis functions used along the x-, y- and z-axis are $\{M, M, 25\}$ respectively (with both blocks aligned along the z-axis) and the employed value of M is denoted between brackets.

To assess the accuracy of the two distinct surface admittance matrix computation avenues, we turn our attention to the real part of the impedance for a fixed separation distance g of $1\,\mu$m. In Fig. 5.17, we clearly see that for low frequencies, Method 2 (black dotted curve) correctly predicts the Pouillet resistance value of $1.7 \cdot 10^{-4}\,\Omega$ and that it exhibits the characteristic $\sqrt{f}$-behavior as the skin effect develops. The maximum value M of the indices governing the cross-section, i.e., m and n, has been set to 25, with the same value along the longitudinal z-axis. When we compare this to Method 3 with the same restrictions on the indices, we see that while the low-frequency results coincide nicely, the resistance curve for (5.35) levels out around 10 MHz. This nonphysical result is caused by cutting off the infinite summation for numerical evaluation, which is clearly detrimental for accurate results, especially for a strongly developed skin effect. This leveling out would be alleviated by driving up the number of eigenmodes M to higher values, but as shown in Fig. 5.17, even a considerable amount of eigenmodes does not suffice to yield adequate results over the complete frequency range. Moreover, it comes at a high computation cost. In Method 2, this shortcoming is solved by exploiting the closed form of the infinite sums as demonstrated in Section 5.4.2.

Table 5.2 contains a more detailed comparison of the computation cost by listing the computation time per frequency point and memory consumption for the provided example. A set-up time of 170 s for the computation of the $\overline{\overline{L}}$ and $\overline{\overline{K}}$ matrices is not included as these results can be reused for all frequency points. From the table we clearly see that the computation time and memory requirements for both methods are of the same order for the same number of eigenmodes. However,

Table 5.2: Computation time and memory usage per frequency point for the configuration of Fig. 5.17.

Metric	Method 2 (25)	Method 3 (25)	Method 3 (200)
$\overline{\overline{Y}}$ calculation [s]	0.86	0.88	30.91
Matrix solution [s]	0.5	0.51	0.5
$\overline{\overline{Y}}$ calculation [MiB]	5.6	5.1	5.5

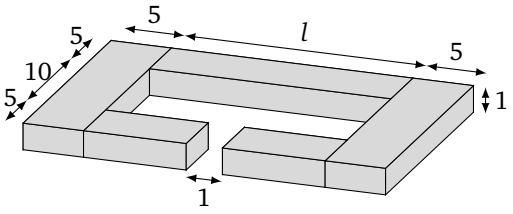

Figure 5.18: Copper loop with one side of variable length l. All dimensions shown are given in μm.

when comparing to the result from Method 3 with an increased number of eigenmodes to increase accuracy at higher frequencies, the entire domain basis functions based method evidently outperforms the other technique. The memory consumption stays roughly the same but the computation time increases by a factor 35 for an increase of M from 25 to 200.

5.5.2 Application examples

Rectangular loop

The initial application example is a rectangular loop, characterized with Method 1. The dimensions (in micrometers) are found in Fig. 5.18. First we examine the loop for a fixed side length l of 20 μm. The configuration is the same as the one from Fig. 3 in [14] and therefore the conductivity of copper is taken to be $\sigma = 5.6 \cdot 10^7$ S/m. The total resistance and inductance of this loop is measured over the 1 μm gap and shown on both panels of Fig. 5.19 and is compared with two 3-D electromagnetic (EM) industry standards, viz., Analysis Systems (ANSYS) High Frequency Simulation Software (HFSS) [15] and Computer Simulation Technology (CST) Microwave Studio (MWS) [16]. In Fig. 5.19(a) we see that both reference solutions coincide with our result at low frequencies while the value from [14] is larger, similar to what we observed for the single corner in Section 5.5.1. The low-frequency inductance of the proposed method coincides with the value computed by HFSS and together they lie within a 3 % margin of the result from CST MWS while the value from [14] differs 9.6 % and 6.6 % from both reference solutions, respectively. This shows that limiting the flow of the current in each cuboid to its longitudinal direction, as assumed in [14], introduces non-negligible deviations.

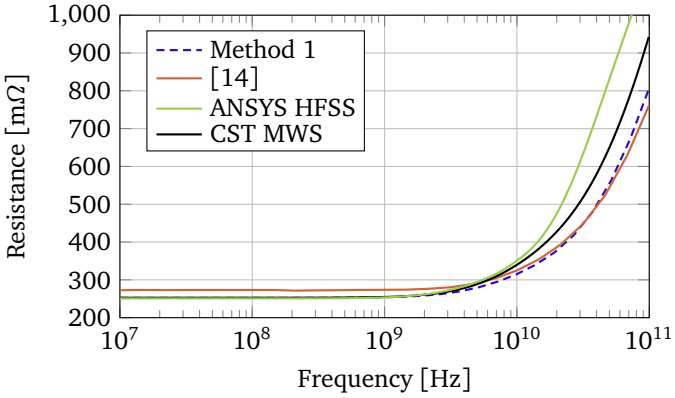

(a) Resistance in mΩ.

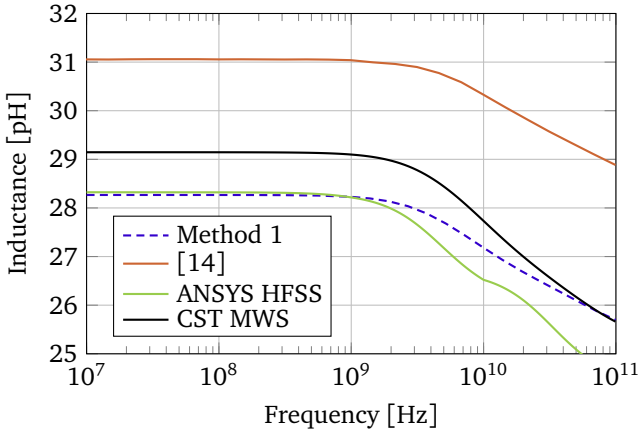

(b) Inductance in pH.

Figure 5.19: Resistance and inductance of the copper loop ($\sigma = 5.6 \cdot 10^7$ S/m) of Fig. 5.18 for $l = 20\,\mu$m as a function of frequency. The configuration is taken from [14] and this result is shown alongside with simulation results from ANSYS HFSS and CST MWS.

Table 5.3: DC resistance of a straight copper ($\sigma = 5.8 \cdot 10^7$ S/m) cuboid and loop (see Fig. 5.18) for various values of l.

l [μm]	cuboid [mΩ]	loop [mΩ]
10	203.5	175.5
15	237.9	210.2
20	272.4	245.0
25	306.9	279.8
30	341.4	314.6

For higher frequencies, both reference solutions' resistance and inductance start changing earlier and at a faster rate. As radiation losses are extremely small and considering the unphysical *kink* in the inductance curve of HFSS in Fig. 5.19(b), we conclude that faulty meshing of the inside of the good conductor fails to properly assess the current crowding and proximity effects in both volume meshing solvers. Meanwhile, our method and the one described in [14] make use of BIEs and alleviate this shortcoming. Both methods demonstrate near identical trends or evolutions for higher frequencies despite their low-frequency difference. This justifies the advocated differential surface admittance operator based BEM for the modeling of 3-D interconnects.

Second, we vary the length l of the loop and again calculate the resistance and inductance with Method 1 shown in Fig. 5.20, this time for a conductivity of $\sigma = 5.8 \cdot 10^7$ S/m. Careful inspection of the low-frequency value of the resistances shows that the obtained values are smaller than the DC Pouillet resistance of a single cuboid with the same total length as the loop (see the selected results in Table 5.3). This can be attributed to an accurate 3-D modeling of the corners present in the loop as demonstrated before for the single corner in Fig. 5.12. For the higher frequencies we note that the curves are more tightly packed. The smaller value of l makes the loop more compact and brings the various conductors closer together. This strengthens the proximity effect and causes the smaller loop's resistance to start increasing at an earlier frequency than for the larger loop.

Parallel plate capacitor with feed structure

The second validation example, depicted in Fig. 5.21, represents a copper ($\sigma = 5.8 \cdot 10^7$ S/m) parallel plate capacitor with variable width w and a 1 μm separation between the plates, fed via two traces that form a rectangular loop. All dimensions are annotated on the figure and are given in μm. The total impedance of this structure is measured over the 1 μm gap for a broad frequency range and obtained through Method 2. In Fig. 5.22 the absolute value of this impedance is shown for various values of w (including results from CST MWS shown with markers) and for a reference planar loop. This reference loop has the same shape and dimen-

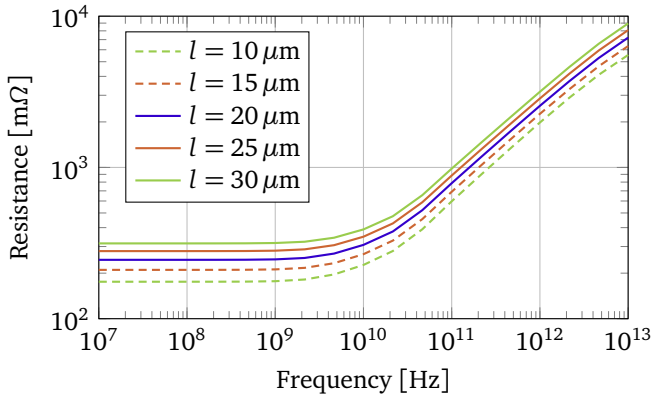

(a) Resistance in mΩ.

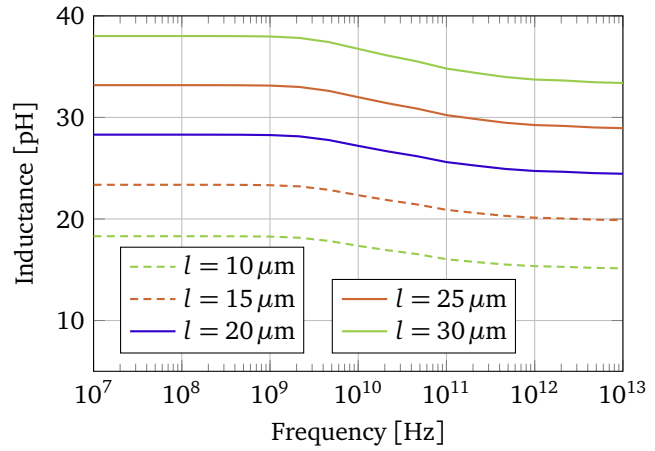

(b) Inductance in pH.

Figure 5.20: Resistance and inductance of the copper loop ($\sigma = 5.8 \cdot 10^7$ S/m) of Fig. 5.18 for various values of the parameter l.

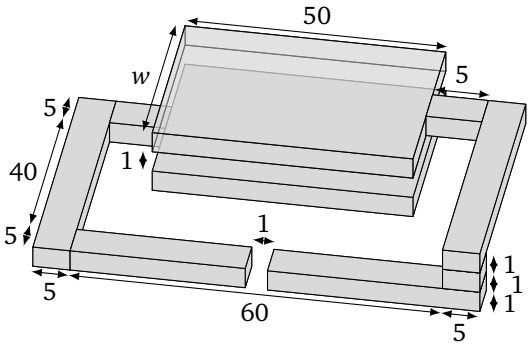

Figure 5.21: Two copper ($\sigma = 5.8 \cdot 10^7\,\mathrm{S/m}$) plates of variable width w with a feeding structure. All dimensions shown are in μm. The impedance is measured over the 1 μm gap.

sions, i.e., 60 μm × 40 μm, as the structure in Fig. 5.21 but lacks the parallel plates, and thus resembles the previous example, shown in Fig. 5.18. For low frequencies, we see that the structure behaves as a capacitance which increases for larger widths w. The response of the planar loop, on the other hand, indicates inductive behavior with a non-negligible resistive component that levels out the response for the lowest frequencies. Around 150 GHz, the structure undergoes a series resonance, whose precise frequency shifts with w as the capacitance changes. For even higher frequencies (around 700 GHz), the structure endures a second (parallel) resonance. This phenomenon is caused by the capacitance of the gap where the impedance is measured. The planar loop exhibits the same resonance albeit at a lower frequency of 630 GHz due the absence of the parallel plate capacitance.

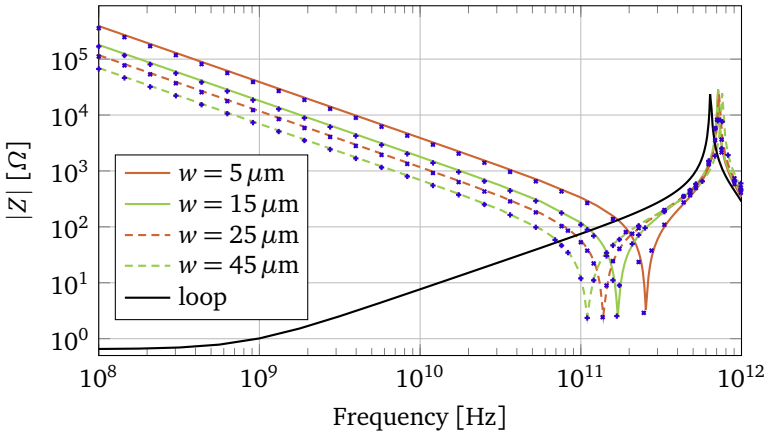

Figure 5.22: Absolute value of the impedance of the structure in Fig. 5.21 for various values of w. Lines indicate results obtained via Method 2, while the CST MWS results are indicated by blue markers.

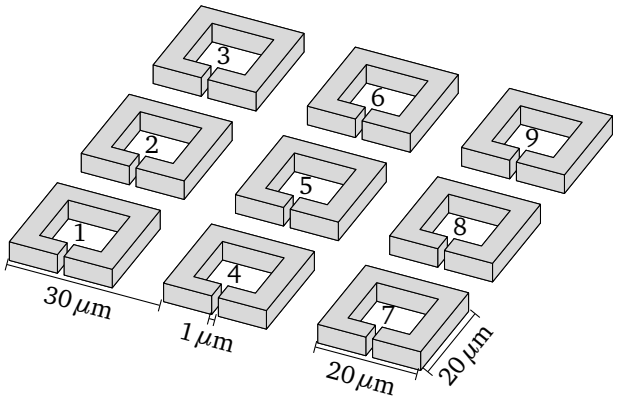

Figure 5.23: 3×3 array of square, copper loops (20 μm×20 μm) with a square cross section of 4 μm×4 μm spaced 30 μm apart. A port is defined over a 1 μm gap on the same side for every loop [17].

Rectangular loop array

Consider an array of square, copper ($\sigma = 5.8 \cdot 10^7$ S/m) coils, arranged in a 3×3 grid with a mutual spacing of 30 μm as described and simulated with VoxHenry in [17] (see Fig. 5.23). Each coil, having a square cross-section with side 4 μm, measures 20 μm×20 μm. In the middle of one side of all coils, a port is defined over a 1 μm gap. The array will be studied for two different cases, viz., with and without ground plane, by means of Method 2. In case of a ground plane,an infinite PEC plane is positioned 2 μm below the loops. Both situations are compared to a corresponding ANSYS HFSS simulation.

In Fig. 5.24 a diagonal element from the structure's Z-parameters is shown as a function of frequency. Fig. 5.24(a) shows the real part of Z_{55}, i.e., the resistance of the central loop. Method 2, VoxHenry (see [17]) and HFSS all predict the same response although a small deviation is visible at higher frequencies between all three. This can be attributed to the inherent difference between volumetric methods, volume integral equation (VIE) methods and BEMs. Nevertheless, it is apparent from the set of results that the ground plane has a negligible influence on the resistance.

Turning to Fig. 5.24(b), the imaginary part of the same Z-matrix element over ω is shown in pH. The curves for the structure in free space both coincide very well with the VoxHenry result. The case with ground plane results in an offset between both curves. This deviation is caused by the different implementation of the infinite ground plane. In our BIE approach, this feature is taken into account through the Green's function while in the FEM based HFSS solver this is achieved through the appropriate boundary conditions on the bounding box of the simulation domain. In [17] the shift in inductance due to the ground plane is not observed but can be attributed to the fact that their ground plane is finite and lossy.

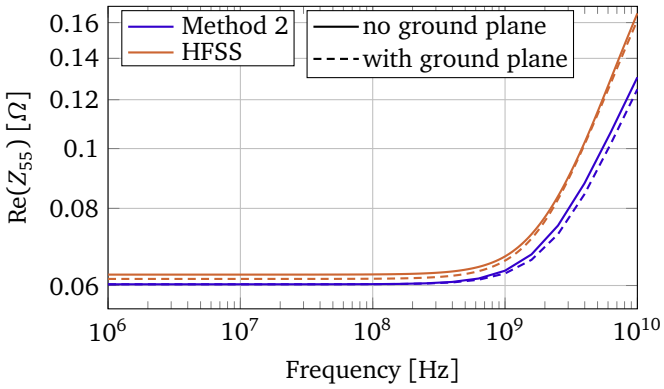

(a) Real part of Z_{55} expressed in Ω.

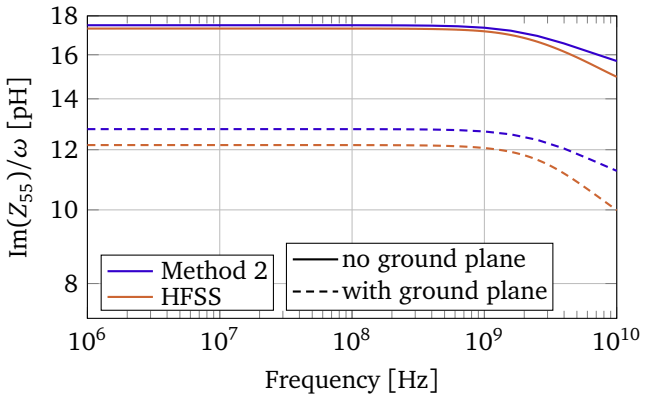

(b) Imaginary part of Z_{55} over ω expressed in pH.

Figure 5.24: Real and imaginary part of Z_{55} as a function of frequency for the geometry shown in Fig. 5.23 with (solid) and without (dashed) ground plane.

Moving on to the off-diagonal elements in Fig. 5.25, we take a closer look at the coupling between two sets of adjacent loops, i.e., loop two and loop five in Fig. 5.25(a) and loop four and loop five in Fig. 5.25(b), respectively. For the first pair, the correspondence between both solvers is similar to Fig. 5.24(b) while for the second pair there is a larger discrepancy. Comparing the two pairs, both our method and HFSS predict a smaller coupling for the second pair but using the differential surface admittance operator this drop is bigger, resulting in the observed difference in the response. A possible explanation for this disparity is the difference in port definition between the compared methods. Still, comparing to the VoxHenry results, we see that our response curves again coincide nicely for the free space case.

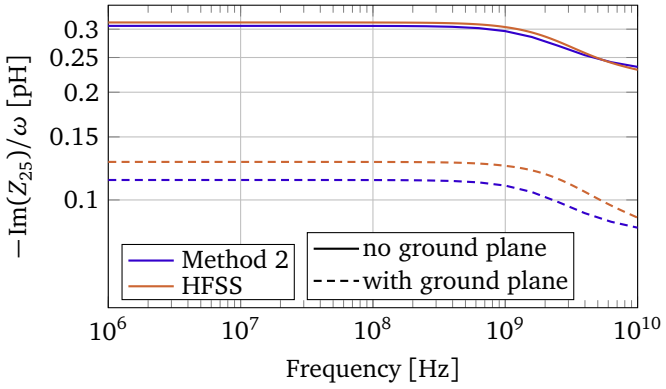

(a) The negative imaginary part of Z_{25} over ω expressed in pH.

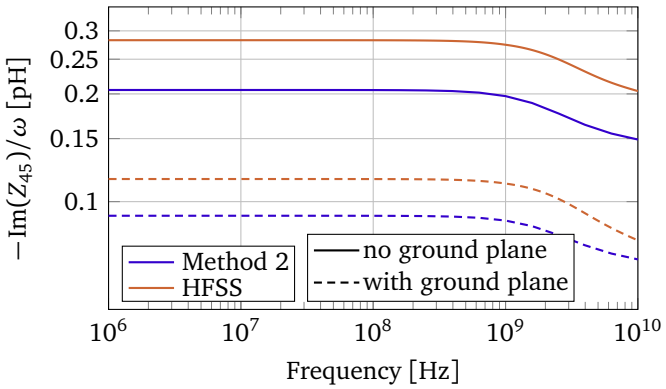

(b) The negative imaginary part of Z_{45} over ω expressed in pH.

Figure 5.25: Selected nondiagonal impedance matrix elements as a function of frequency for the geometry shown in Fig. 5.23 with (solid) and without (dashed) ground plane.

Two coupled on-chip inductors

As a final example, a test chip was designed, manufactured and measured by Geert Van der Plas and Xiao Sun in Eric Beyne's 3-D system integration group at imec. This chip consists of an aluminum ($\sigma = 3.77{\cdot}10^7$ S/m) loop placed 6.508 μm above a smaller copper ($\sigma = 5.8 \cdot 10^7$ S/m) loop. Both elements have the same inner dimensions for the loop, i.e., 100 μm $\times$ 70 μm, but have different cross-sections, as shown in Fig. 5.26 together with all other relevant dimensions, which are all given in micrometers. The loops are placed in an on-chip multilayered stack-up that is not included here as the nonmagnetic materials have negligible influence on the mainly inductive coupling phenomena in this setup. The scattering parameters of this structure are simulated by means of Method 2 and HFSS. The coupling

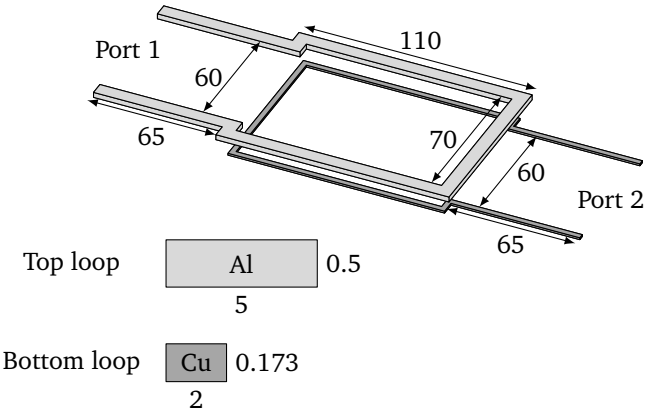

Figure 5.26: Two coupled loops spaced 6.508 μm apart. The top aluminum loop ($\sigma = 3.77 \cdot 10^7$ S/m) has a cross section of 5 μm×0.5 μm while the bottom copper loop measures 2μm×0.173 μm. All dimensions in the figure are given in μm.

is also compared to measurement data and shown in Fig. 5.27. The measured diagonal elements of the S-matrix are not included in the analysis as the complex feed structure and measurement setup did not allow for stable de-embedding over the entire frequency range.

Starting with Fig. 5.27(a), we observe excellent agreement between the proposed method, HFSS and the measured $|S_{21}|$. The measurement shows a slightly lower coupling over the entire frequency band due to additional losses in the measurement. At the end of the frequency range the three curves diverge more due to high-frequency noise in the measurement data and the earlier observed difference between volumetric and surface methods. Advancing to Fig. 5.27(b), we show the absolute value of S_{11} and S_{22} for the coupled loops. Once again, we obtain very good agreement between our Method 2 and HFSS.

5.6 Conclusions

In this chapter, we have introduced a framework to accurately characterize 3-D interconnect structures. For the evaluation of the structures, two different EFIE formulation were derived: one led to a circuit interpretation of the boundary integral equation that was solved using conventional circuit solvers while the other, based on the augmented EFIE, yielded a set of matrix equations that fully describes the electromagnetic problem. Furthermore, the differential surface admittance for the quintessential building block of interconnects, i.e., the cuboid, was derived based on the eigenmodes of the volume. Two options were presented: the conventional form analogous to the one present for cylinder in Chapter 4, and an improved formulation, specifically for cuboids, that through the use of entire domain basis

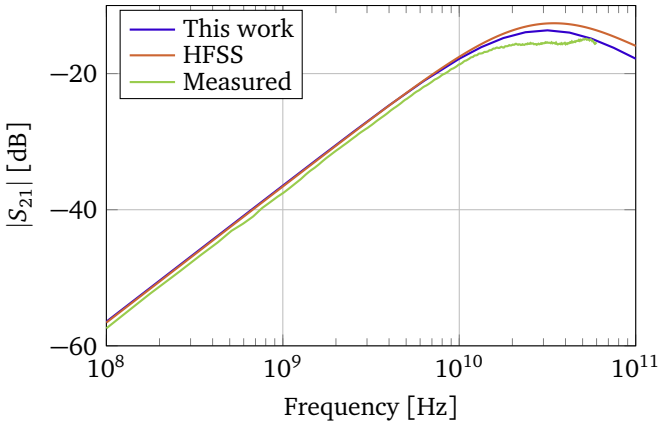

(a) Absolute value of S_{21}.

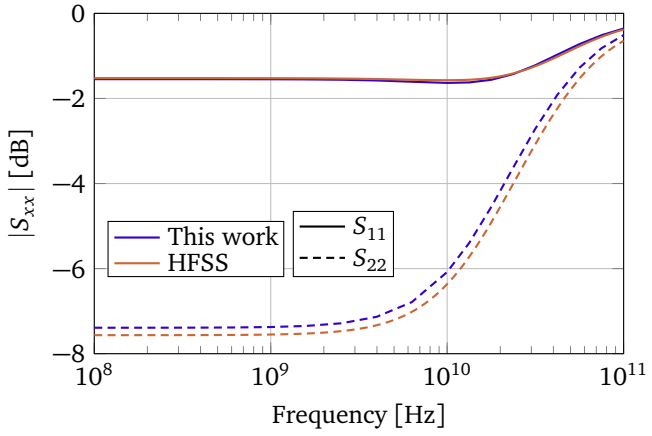

(b) Absolute value of S_{11} and S_{22}.

Figure 5.27: Scattering matrix elements as a function of frequency for the geometry shown in Fig. 5.26.

functions and the sum of infinite series, resulted in a faster, more accurate differential surface admittance matrix. The presented methods have been thoroughly validated through numerous examples including 2-D reference results, meticulous evaluation of essential 3-D building blocks and careful computation of nonidealized capacitors. Additionally, both expressions for the differential surface admittance matrix have been painstakingly compared in a simple example to assess their accuracy and computational cost/speed. Afterwards, both methods were utilized to study a few applications examples, ranging from a single loop and parallel plate capacitor with feed structure to an array of rectangular loops and coupled on-chip inductors.

References

[1] E. Sicard, W. Jianfei, R. J. Shen, E. P. Li, E. X. Liu, J. Kim, J. Cho, and M. Swaminathan, "Recent advances in electromagnetic compatibility of 3D-ICs - Part I", *IEEE Electromagn. Compat.*, vol. 4, no. 4, pp. 79–89, 2015.

[2] J. Peeters, I. Bogaert, and D. De Zutter, "Calculation of MoM interaction integrals in highly conductive media", *IEEE Trans. Antennas Propag.*, vol. 60, no. 2, pp. 930–940, Feb. 2012.

[3] M. Gossye, M. Huynen, D. Vande Ginste, D. De Zutter, and H. Rogier, "A Calderón preconditioner for high dielectric contrast media", *IEEE Trans. Antennas Propag.*, vol. 66, no. 2, pp. 808–818, Feb. 2018.

[4] T. Senior and J. Volakis, *Approximate Boundary Conditions in Electromagnetics*, ser. Electromagnetics and Radar Series. Institution of Electrical Engineers, 1995.

[5] I. Hänninen, M. Taskinen, and J. Sarvas, "Singularity subtraction integral formulae for surface integral equations with RWG, rooftop and hybrid basis functions", *Prog. Electromagn. Res.*, vol. 63, pp. 243–278, 2006.

[6] Linear Technology. (2016). LT SPice XVII, [Online]. Available: `http://www.linear.com/ltpsice/`.

[7] Z. G. Qian and W. C. Chew, "An augmented electric field integral equation for high-speed interconnect analysis", *Microw. Opt. Technol. Lett.*, vol. 50, no. 10, pp. 2658–2662, Oct. 2008.

[8] ——, "Fast full-wave surface integral equation solver for multiscale structure modeling", *IEEE Trans. Antennas Propag.*, vol. 57, no. 11, pp. 3594–3601, Nov. 2009.

[9] J. G. Van Bladel, *Electromagnetic Fields*. John Wiley & Sons, Inc., May 2007.

[10] G. Lippens, "Model order reduction in the context of interconnects", PhD thesis, Ghent University, 2006.

[11] D. De Zutter and L. Knockaert, "Skin effect modeling based on a differential surface admittance operator", *IEEE Trans. Microw. Theory Techn.*, vol. 53, no. 8, pp. 2526–2538, Aug. 2005.

[12] T. Demeester and D. De Zutter, "Quasi-TM transmission line parameters of coupled lossy lines based on the Dirichlet to Neumann boundary operator", *IEEE Trans. Microw. Theory Techn.*, vol. 56, no. 7, pp. 1649–1660, Jul. 2008.

[13] C. P. Yuan and T. N. Trick, "A simple formula for the estimation of the capacitance of two-dimensional interconnects in VLSI circuits", *IEEE Electron Device Lett.*, vol. 3, no. 12, pp. 391–393, 1982.

[14] U. R. Patel, S. V. Hum, and P. Triverio, "A magneto-quasi-static surface formulation to calculate the impedance of 3D interconnects with arbitrary cross-section", in *2017 IEEE 21st Workshop on Signal and Power Integrity (SPI)*, May 2017, pp. 1–4.

[15] Ansys Inc. (2015). ANSYS HFSS, [Online]. Available: `https://www.ansys.com/`.

[16] Computer Simulation Technology. (2017). CST MICROWAVE STUDIO, [Online]. Available: `https://www.cst.com/`.

[17] A. C. Yucel, I. P. Georgakis, A. G. Polimeridis, H. Bağci, and J. K. White, "VoxHenry: FFT-accelerated inductance extraction for voxelized geometries", *IEEE Trans. Microw. Theory Techn.*, vol. 66, no. 4, pp. 1723–1735, Apr. 2018.

6

The Differential Surface Admittance Operator for Combined Magnetic and Dielectric Contrast

"Some humans would do anything to see if it was possible to do it.
If you put a large switch in some cave somewhere, with a sign on it saying
'End-of-the-World Switch. PLEASE DO NOT TOUCH',
the paint wouldn't even have time to dry. "

Terry Pratchett

★ ★ ★

This chapter details an extension of the 3-D differential surface admittance operator for cuboids. By computing two separate Poincaré-Steklov operators for the cuboid directly, the restriction on nonmagnetic materials for the differential surface admittance operator based on eigenmodes is alleviated. The pair of operators are computed by considering the cuboid as the superposition of six waveguides with one of its open ends metallized. Based on the modes in these waveguides and by expanding the unknown quantities in entire domain basis functions, the differential surface admittance operator can be found in all six cases. Computing the explicit formulas for one of the six cases, reveals that the required expressions resemble these of the nonmagnetic variant of the operator and indeed are a generalization of the latter.

6.1 Introduction

The differential surface admittance operator as presented in Section 3.1 was derived from the general equivalence theorem and enables the replacement of a homogeneous material by the background medium through a single equivalent (electrical) surface current density. In subsequent sections and chapters, expressions for this operator based on the eigenmodes of a volume were constructed and applied to cylinders and cuboids, and its usage was demonstrated for a variety of materials and configurations. However, in all these cases an additional restriction was enforced: the material in question had to be nonmagnetic or, less restrictive, was required to have the same permeability as the background medium. Although this supplementary constraint applies to the lion's share of materials employed in circuits, antennas, etc., ranging from dielectrics to (good) conductors, an important subset of materials, i.e., magnetic materials, is excluded that play a crucial role in certain applications. One such example are the so-called mu-metals. These materials combine a high permeability with low hysteresis losses and limited anisotropy, justifying their prevalent usage in an electromagnetic compatibility (EMC) context where low-frequency magnetic shielding is essential, e.g., MRI [1].

In this chapter, we present an alternative approach to the entire domain basis functions construction of the differential surface admittance operator for cuboids as described in Section 5.4. Not only does this derivation provide additional insight into the structure of this operator, it does not require the absence of magnetic contrast, opening the way to the inclusion of materials with both an electric and magnetic contrast. In Section 6.2, we clarify the working principle of this derivation based on the construction of a Poincaré-Steklov operator for the cuboid from its eigenmodes. In Sections 6.3.1 and 6.3.2, expressions for the surface current density are determined.

6.2 Poincaré-Steklov operator for cuboids

Referring back to Section 3.1, it was shown in (3.7) that the differential surface admittance operator can be expressed as the difference between two Poincaré-Steklov operators, one for the original situation and one for the equivalent scenario. In the derivation of the general expressions for the differential surface admittance operator based on the eigenfunctions of the volume, however, the differential operator was formed directly, contracting the additional nonmagnetic constraint along the way. Here, we determine both Poincaré-Steklov operators first and only afterwards substitute them into (3.7), leading to the sought after $\mathcal{Y}$-operator.

To construct the Poincaré-Steklov operator, which expresses the rotated tangential magnetic field $\hat{\mathbf{n}} \times \mathbf{h}^t$ in any point on the surface $\mathcal{S}$ as a function of the tangential electric field $\mathbf{e}^t$ in all points on that same surface, we take the following approach: in accordance with the superposition principle, the overall dependence of $\hat{\mathbf{n}} \times \mathbf{h}^t$ on $\mathbf{e}^t$ can be obtained by putting $\mathbf{e}^t = \mathbf{0}$ on all but one of the faces of the cuboid

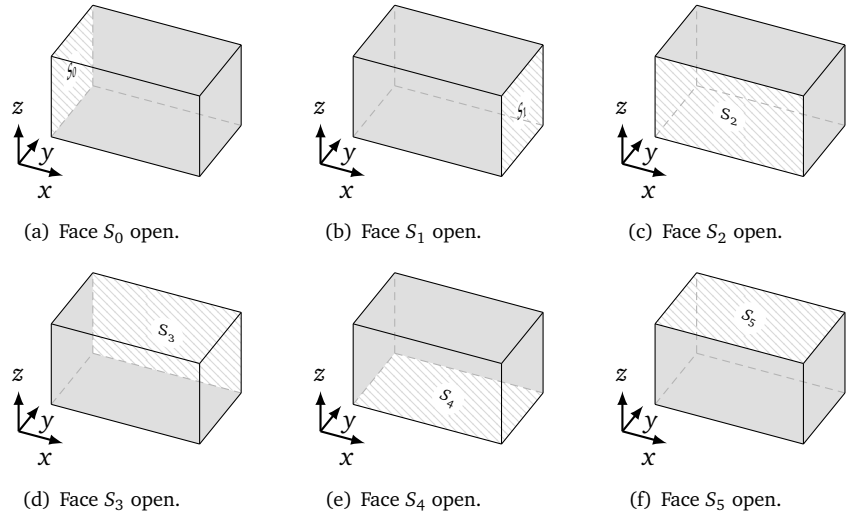

(a) Face S_0 open. (b) Face S_1 open. (c) Face S_2 open.

(d) Face S_3 open. (e) Face S_4 open. (f) Face S_5 open.

Figure 6.1: Superposition principle applied to the cuboid for the calculation of its Poincaré-Steklov operator. Throughout this chapter, situation (f) is discussed in detail, knowing that cases (a)-(e) are completely analogous.

and determining the resulting $\hat{\mathbf{n}} \times \mathbf{h}^t$ on all the faces as long as the volume is filled with a linear material (shown in Fig. 6.1). Naturally, this procedure has to be repeated for all other five faces to achieve the complete solution. Analogous to the formulation in Section 5.4.1, we thus only discuss the case for one of the six faces in the remainder of this chapter, knowing that the other faces can be treated in completely the same way.

A cuboid filled with a material characterized by (ϵ, μ), whose tangential electric field vanishes on its surface, except for one single face, can be considered a PEC waveguide with one of its open ends metallized. In order to tie in with the notation and choices of Chapter 5, we take the waveguide to be oriented along the z-axis. As such, the fields inside can be expressed as a sum of two sets of modes, viz., the TE modes (5.16)–(5.18) and the TM modes (5.19)–(5.21). As the fifth metallized face, we choose the face at $z = 0$; in other words, the *open* face of the structure where $\mathbf{e}^t \neq \mathbf{0}$ is the face at $z = l_z$, i.e., S_5 (this corresponds to Fig. 6.1(f)).

When constructing the Poincaré-Steklov operator, we have to choose a representation for $\mathbf{e}^t$ and $\hat{\mathbf{n}} \times \mathbf{h}^t$ that ensures that these field quantities can take all possible values. Inspired by Section 5.4.1, the most elegant choice is the use of entire domain basis functions as they optimally profit from the properties of the eigenmodes. Careful inspection of the mode expressions in the waveguide, before metallizing

face S_4, shows that on S_4 and S_5

$$e_x \text{ and } \hat{\mathbf{n}} \times h_y \propto \cos(\lambda_x x)\sin\left(\lambda_y y\right) \tag{6.1}$$

$$e_y \text{ and } \hat{\mathbf{n}} \times h_x \propto \sin(\lambda_x x)\cos\left(\lambda_y y\right), \tag{6.2}$$

i.e., a cosine dependence along the direction of the electric field and a sine dependence in the direction of the magnetic field. λ_x and λ_y are defined as $m\pi/l_x$ and $n\pi/l_z$, respectively. Similar expressions for the rotated tangential magnetic fields are to be made on all other faces as well. Although this choice of basis functions will prove to be beneficial in constructing the $\mathcal{Y}$-operator, it may prove difficult to integrate this form into the integral equation that solves the equivalent problem's exterior. However, the transformation to another basis, e.g., local basis functions, is generally easily found and for rooftop functions specifically, it is found to be $\overline{\overline{M}}$ as constructed in Section 5.4.3.

A consequence of our choice of entire domain basis functions is that it turns out to be advantageous to recombine the TE and TM modes (5.16)–(5.21) into two new sets where either $e_x \neq 0$ and $e_y = 0$ or vice versa. By multiplying the TM modes by $-\omega\mu\lambda_x/\gamma_{mn}\lambda_y$ (with $\gamma_{mn} = \sqrt{k^2-\lambda_x^2-\lambda_y^2}$) and combining both modes, the modal field distributions for the first set become

$$e_{z,mn}(\boldsymbol{\rho}) = -\frac{\lambda_x}{j\gamma_{mn}}\sin(\lambda_x x)\sin\left(\lambda_y y\right) \tag{6.3}$$

$$h_{z,mn}(\boldsymbol{\rho}) = \frac{\lambda_y}{j\omega\mu}\cos(\lambda_x x)\cos\left(\lambda_y y\right) \tag{6.4}$$

$$\mathbf{e}_{t,mn}(\boldsymbol{\rho}) = \left[\cos(\lambda_x x)\sin\left(\lambda_y y\right)\hat{\mathbf{x}} + 0\,\hat{\mathbf{y}}\right] \tag{6.5}$$

$$\mathbf{h}_{t,mn}(\boldsymbol{\rho}) = \frac{\lambda_y}{\omega\mu\gamma_{mn}}\left[-\lambda_x\sin(\lambda_x x)\cos\left(\lambda_y y\right)\hat{\mathbf{x}} + \frac{k^2-\lambda_y^2}{\lambda_y}\cos(\lambda_x x)\sin\left(\lambda_y y\right)\hat{\mathbf{y}}\right], \tag{6.6}$$

while multiplying with the factor $\omega\mu\lambda_y/\gamma_{mn}\lambda_x$ for the TM modes, the linear combination gives

$$e_{z,mn}(\boldsymbol{\rho}) = -\frac{\lambda_y}{j\gamma_{mn}}\sin(\lambda_x x)\sin\left(\lambda_y y\right) \tag{6.7}$$

$$h_{z,mn}(\boldsymbol{\rho}) = -\frac{\lambda_x}{j\omega\mu}\cos(\lambda_x x)\cos\left(\lambda_y y\right) \tag{6.8}$$

$$\mathbf{e}_{t,mn}(\boldsymbol{\rho}) = \left[0\,\hat{\mathbf{x}} + \sin(\lambda_x x)\cos\left(\lambda_y y\right)\hat{\mathbf{y}}\right] \tag{6.9}$$

$$\mathbf{h}_{t,mn}(\boldsymbol{\rho}) = \frac{\lambda_x}{\omega\mu\gamma_{mn}}\left[-\frac{k^2-\lambda_x^2}{\lambda_x}\sin(\lambda_x x)\cos\left(\lambda_y y\right)\hat{\mathbf{x}} + \lambda_y\cos(\lambda_x x)\sin\left(\lambda_y y\right)\hat{\mathbf{y}}\right]. \tag{6.10}$$

Note that we have normalized both sets such that e_x and e_y have unit amplitude.

At this point, we have enforced $\mathbf{e}^t = \mathbf{0}$ on faces $S_0 - S_3$ but not yet on S_4, i.e., the face at $z = 0$. In order to achieve this, we remember that (6.3)–(6.10) are solutions for waves propagating in the positive z-direction and thus have an $\exp(-j\gamma_{mn}z)$ dependence. This also implies that we can construct a set of modes for waves propagating in the opposite direction with the corresponding $\exp(+j\gamma_{mn}z)$ dependence (simply obtained by substituting γ_{mn} for $-\gamma_{mn}$). If we combine them such that e_x and e_y have a sine dependence in z, the condition $\mathbf{e}^t = \mathbf{0}$ at S_4 is automatically satisfied. For the first set, this leads to

$$e_{z,mn} = -\frac{\lambda_x}{\gamma_{mn}} \sin(\lambda_x x) \sin\left(\lambda_y y\right) \cos(\gamma_{mn} z) \tag{6.11}$$

$$h_{z,mn} = \frac{\lambda_y}{j\omega\mu} \cos(\lambda_x x) \cos\left(\lambda_y y\right) \sin(\gamma_{mn} z) \tag{6.12}$$

$$e_{x,mn} = \cos(\lambda_x x) \sin\left(\lambda_y y\right) \sin(\gamma_{mn} z) \tag{6.13}$$

$$\begin{aligned} \mathbf{h}_{t,mn} = \frac{1}{j\omega\mu\gamma_{mn}} \big[& \lambda_x \lambda_y \sin(\lambda_x x) \cos\left(\lambda_y y\right) \cos(\gamma_{mn} z)\, \hat{\mathbf{x}} \\ & - \left(k^2 - \lambda_y^2\right) \cos(\lambda_x x) \sin\left(\lambda_y y\right) \cos(\gamma_{mn} z)\, \hat{\mathbf{y}} \big], \end{aligned} \tag{6.14}$$

and for the second set, this yields

$$e_{z,mn} = -\frac{\lambda_y}{\gamma_{mn}} \sin(\lambda_x x) \sin\left(\lambda_y y\right) \cos(\gamma_{mn} z) \tag{6.15}$$

$$h_{z,mn} = -\frac{\lambda_x}{j\omega\mu} \cos(\lambda_x x) \cos\left(\lambda_y y\right) \sin(\gamma_{mn} z) \tag{6.16}$$

$$e_{y,mn} = \sin(\lambda_x x) \cos\left(\lambda_y y\right) \sin(\gamma_{mn} z) \tag{6.17}$$

$$\begin{aligned} \mathbf{h}_{t,mn} = \frac{1}{j\omega\mu\gamma_{mn}} \big[& \left(k^2 - \lambda_x^2\right) \sin(\lambda_x x) \cos\left(\lambda_y y\right) \cos(\gamma_{mn} z)\, \hat{\mathbf{x}} \\ & - \lambda_x \lambda_y \cos(\lambda_x x) \sin\left(\lambda_y y\right) \cos(\gamma_{mn} z)\, \hat{\mathbf{y}} \big]. \end{aligned} \tag{6.18}$$

Remark that during the combination we have also rescaled both sets such that e_x and e_y, respectively, have a unit coefficient.

With these expressions, we can now construct the part of the Poincaré-Steklov $\mathcal{P}$ operator for the cuboid originating from nonzero electric fields on S_5. We only need to set z to l_z in (6.13) or (6.17), respectively, and divide by $\sin(\gamma_{mn} l_z)$ to obtain the entire domain basis functions (6.1)–(6.2) for $\mathbf{e}^t$ on this face. By extracting the resulting $\hat{\mathbf{n}} \times \mathbf{h}^t$ on all six faces, we obtain $\mathcal{P}$. By repeating the entire procedure for a cuboid filled with the background material (ϵ_0, μ_0), we get the operator $\mathcal{P}''$ (see (3.6)) for the equivalent configuration. Subtracting both yields the differential surface admittance operator. In the following section, we directly calculate the effect of $\mathbf{e}^t$ on S_5 on the surface current density $\mathbf{j}_s$ on all faces, i.e., we immediately calculate the entries for $\mathcal{Y}$.

6.3 Surface current density on the cuboid's surface

With the two Poincaré-Steklov operators $\mathcal{P}$ and $\mathcal{P}''$ fully defined, we can construct the $\mathcal{Y}$-operator from them since $\mathbf{j}_s = \hat{\mathbf{n}} \times (\mathbf{h} - \mathbf{h}'') = (\mathcal{P} - \mathcal{P}'')\,\mathbf{e}_0^t = \mathcal{Y}\,\mathbf{e}^t$. In the following section, we take a look at every face of the cuboid and compute the surface current density resulting from the following two basis functions on S_5, corresponding to set 1 and 2, respectively,

$$e_x = \cos(\lambda_x x)\sin\left(\lambda_y y\right) \tag{6.19}$$

$$e_y = \sin(\lambda_x x)\cos\left(\lambda_y y\right). \tag{6.20}$$

6.3.1 Surface current density on parallel faces

S_5 **to** S_5

First, we look at the induced surface current density on the same face of the cuboid as the nonzero tangential electric field, i.e., S_5 with $\hat{\mathbf{n}} = \hat{\mathbf{z}}$. For the first set, the excitation (6.19) gives rise to a surface current density along both x and y, which we denote in terms of the entire domain basis functions as

$$j_{s,x} = A^0 \cos(\lambda_x x)\sin\left(\lambda_y y\right) \tag{6.21}$$

$$j_{s,y} = A^1 \sin(\lambda_x x)\cos\left(\lambda_y y\right). \tag{6.22}$$

The coefficients A^0 and A^1 are found by first setting $z = l_z$ in (6.14) and dividing the result by $\sin(\gamma_{mn} l_z)$, i.e., the factor that rescales e_x to the formulation of an entire domain basis functions. This procedure is then repeated for the waveguide filled with the background medium and these factors are subtracted from the ones obtained from (6.14). These resulting coefficients A_0 and A_1 are as such found to be

$$A^0 = \frac{1}{j\omega}\left[\frac{k^2 - \lambda_y^2}{\mu\gamma}\cot(\gamma l_z) - \frac{k_0^2 - \lambda_y^2}{\mu_0\gamma_0}\cot(\gamma_0 l_z)\right] \tag{6.23}$$

$$A^1 = \frac{1}{j\omega}\lambda_x\lambda_y\left[\frac{1}{\mu\gamma}\cot(\gamma l_z) - \frac{1}{\mu_0\gamma_0}\cot(\gamma_0 l_z)\right], \tag{6.24}$$

with $k_0 = \omega\sqrt{\epsilon_0\mu_0}$ and $\gamma_0 = \sqrt{k_0^2 - \lambda_x^2 - \lambda_y^2}$ and where we have dropped the subscript mn on γ/γ_0. Comparing these to (5.61) and (5.63), we see that the same expressions have been found (except for a constant factor) if $\mu = \mu_0$. This shows that the sum of the infinite series as detailed in Appendix C and employed in Section 5.4.2 indeed successfully transforms the series into trigonometric functions. We can now also clearly see the origin of the difference between the two trigonometric functions; they are a result of the difference between the two pertinent Poincaré-Steklov operators.

For the second set, e_y is the nonzero tangential electric field and, just like e_x, induces a surface current density in both directions of S_0:

$$j_{s,x} = \tilde{A}^0 \cos(\lambda_x x) \sin(\lambda_y y) \tag{6.25}$$

$$j_{s,y} = \tilde{A}^1 \sin(\lambda_x x) \cos(\lambda_y y). \tag{6.26}$$

Finding the unknown coefficients is done completely analogously to the first set and yields

$$\tilde{A}^0 = \frac{1}{j\omega} \lambda_x \lambda_y \left[\frac{1}{\mu\gamma} \cot(\gamma l_z) - \frac{1}{\mu_0 \gamma_0} \cot(\gamma_0 l_z) \right] \tag{6.27}$$

$$\tilde{A}^1 = \frac{1}{j\omega} \left[\frac{k^2 - \lambda_x^2}{\mu\gamma} \cot(\gamma l_z) - \frac{k_0^2 - \lambda_x^2}{\mu_0 \gamma_0} \cot(\gamma_0 l_z) \right]. \tag{6.28}$$

Comparing $\tilde{A}^0$ and $\tilde{A}^1$ to A^0 and A^1, we see that $A^0 = \tilde{A}^1$ and $A^1 = \tilde{A}^0$ if λ_x and λ_y are swapped. Actually, A^1 and $\tilde{A}^0$ are equal anyway as they are symmetric in λ_x and λ_y.

S_5 to S_4

On the face opposite to the excitation face, i.e., S_4 with $\hat{\mathbf{n}} = -\hat{\mathbf{z}}$, e_x generates very similar surface current densities as before (6.21)–(6.22) but this time with coefficients B^0 and B^1, which, through the same procedure, are found to be

$$B^0 = -\frac{1}{j\omega} \left[\frac{k^2 - \lambda_y^2}{\mu\gamma} \csc(\gamma l_z) - \frac{k_0^2 - \lambda_y^2}{\mu_0 \gamma_0} \csc(\gamma_0 l_z) \right] \tag{6.29}$$

$$B^1 = -\frac{1}{j\omega} \lambda_x \lambda_y \left[\frac{1}{\mu\gamma} \csc(\gamma l_z) - \frac{1}{\mu_0 \gamma_0} \csc(\gamma_0 l_z) \right]. \tag{6.30}$$

Analyzing B^0 and B^1 and comparing with the results on S_5, we see that B^0 and B^1 can be derived from A^0 and A^1, respectively, by replacing cot by $-\csc$. Repeating the same calculation for the second set, reveals that the same holds for $\tilde{B}^0$ and $\tilde{B}^1$ as well, leading to

$$\tilde{B}^0 = -\frac{1}{j\omega} \lambda_x \lambda_y \left[\frac{1}{\mu\gamma} \csc(\gamma l_z) - \frac{1}{\mu_0 \gamma_0} \csc(\gamma_0 l_z) \right] \tag{6.31}$$

$$\tilde{B}^1 = -\frac{1}{j\omega} \left[\frac{k^2 - \lambda_x^2}{\mu\gamma} \csc(\gamma l_z) - \frac{k_0^2 - \lambda_x^2}{\mu_0 \gamma_0} \csc(\gamma_0 l_z) \right]. \tag{6.32}$$

Remark at this point that a single entire domain basis function of the electric field is linked to the same type of basis function for the surface current density along both directions on a parallel or coinciding face. This relation is demonstrated schematically in Fig. 6.2. In the next section, we will see that this one-to-one correspondence no longer holds for the perpendicular faces.

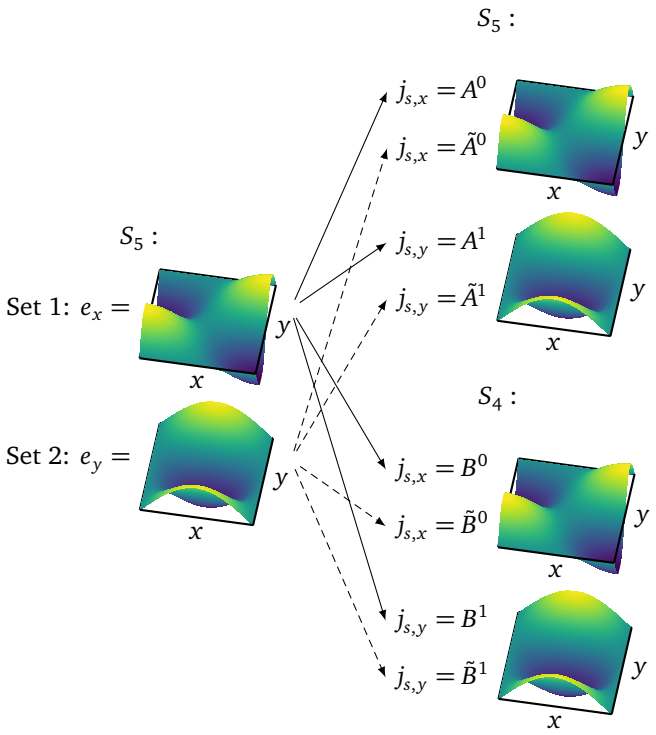

Figure 6.2: Schematic overview of the induced surface current density of set 1 and set 2 on faces S_5 and S_4. In the illustration m and n are set to 1 and 2, respectively.

6.3.2 Surface current density on perpendicular faces

S_5 **to** S_3

Keeping the same e_x on S_5 as the source of the induced surface current densities, we now turn to the face at $y = l_y$ with $\hat{\mathbf{n}} = \hat{\mathbf{y}}$, viz., S_3. $\mathbf{j}_s$ is then found to be

$$j_{s,z} = -\frac{1}{j\omega}\lambda_x\lambda_y \sin(\lambda_x x)(-1)^n \left[\frac{\cos(\gamma z)}{\mu\gamma \sin(\gamma l_z)} - \frac{\cos(\gamma_0 z)}{\mu_0\gamma_0 \sin(\gamma_0 l_z)}\right] \tag{6.33}$$

$$j_{s,x} = \frac{1}{j\omega}\lambda_y \cos(\lambda_x x)(-1)^n \left[\frac{\sin(\gamma z)}{\mu \sin(\gamma l_z)} - \frac{\sin(\gamma_0 z)}{\mu_0 \sin(\gamma_0 l_z)}\right], \tag{6.34}$$

while the second set of modes leads to

$$j_{s,z} = -\frac{1}{j\omega}\sin(\lambda_x x)(-1)^n \left[\frac{k^2 - \lambda_x^2}{\mu\gamma}\frac{\cos(\gamma z)}{\sin(\gamma l_z)} - \frac{k_0^2 - \lambda_x^2}{\mu_o\gamma_0}\frac{\cos(\gamma_0 z)}{\sin(\gamma_0 l_z)}\right] \tag{6.35}$$

$$j_{s,x} = -\frac{1}{j\omega}\lambda_x \cos(\lambda_x x)(-1)^n \left[\frac{\sin(\gamma z)}{\mu \sin(\gamma l_z)} - \frac{\sin(\gamma_0 z)}{\mu_0 \sin(\gamma_0 l_z)}\right]. \tag{6.36}$$

A closer look at these induced surface current densities quickly shows that they do not fit the mould of our entire domain basis functions. The x-dependence is present with $\cos(\lambda_x x)$ and $\sin(\lambda_x x)$ for $\mathbf{j}_s$ along x and z, respectively, but the z-dependence still hinges on the material properties through the factor γ and γ_0 in the argument of the (co)sine. In order to obtain the full expressions for the entire domain basis functions, we need to rewrite the z-dependent functions. Thereto, we expand $\sin(\gamma z)$ and $\cos(\gamma z)$ (and analogously for γ_0) into Fourier series as

$$\sin(\gamma z) = \sum_{p=1}^{\infty} \alpha_p \sin(\lambda_z z) \tag{6.37}$$

$$\cos(\gamma z) = \sum_{p=0}^{\infty} \beta_p \cos(\lambda_z z), \tag{6.38}$$

with $\lambda_z = p\pi/l_z$. The coefficients α_p and β_p of these series can easily be found by multiplying both sides of (6.37) and (6.38) with $\sin(\lambda_z)$ and $\cos(\lambda_z)$, respectively for a fixed value of p and integrating over z from 0 to l_z. This isolates a single coefficient through the orthogonality of the trigonometric functions and after some calculations, this yields

$$\alpha_p = \frac{2p\pi}{l_z^2}(-1)^p \frac{1}{k^2 - k_{mnp}^2} \sin(\gamma l_z) \tag{6.39}$$

$$\beta_p = \frac{\varepsilon_p \gamma}{l_z}(-1)^p \frac{1}{k^2 - k_{mnp}^2} \sin(\gamma l_z). \tag{6.40}$$

By substituting (6.37)–(6.38) in the expressions for the induced surface current densities (6.33)–(6.36) on S_3, we cast them in the desirable form of the entire domain basis functions. Note that there is one major difference with the situation on S_5 and S_4: one single entire domain basis function of e_x or e_y on S_5 now excites an infinite series of entire domain basis functions of the surface current density on S_3 along both the z- and x-axis. In other words, there is no longer a one-to-one interaction as was the case for the coinciding and parallel planes. For e_x, this yields

$$j_{s,z} = \sum_{p=0}^{\infty} C_p^0 \cos(\lambda_z z) \sin(\lambda_x x) \tag{6.41}$$

$$j_{s,x} = \sum_{p=1}^{\infty} C_p^1 \sin(\lambda_z z) \cos(\lambda_x x), \tag{6.42}$$

with the coefficients given by

$$C_p^0 = -\frac{1}{j\omega}\frac{\varepsilon_p \lambda_x \lambda_y}{l_z}(-1)^n(-1)^p \left[\frac{1}{\mu\left(k^2 - k_{mnp}^2\right)} - \frac{1}{\mu_0\left(k_0^2 - k_{mnp}^2\right)}\right] \tag{6.43}$$

$$C_p^1 = \frac{1}{j\omega}\frac{2\pi p \lambda_y}{l_z^2}(-1)^n(-1)^p \left[\frac{1}{\mu\left(k^2 - k_{mnp}^2\right)} - \frac{1}{\mu_0\left(k_0^2 - k_{mnp}^2\right)}\right]. \tag{6.44}$$

The dependence of these coefficients on p is denoted explicitly to emphasize the difference with the corresponding coefficients A^0, A^1, B^0, and B^1 on faces S_5 and S_4.

The same approach of invoking the Fourier series, gives the following expressions for the surface current densities (6.35)–(6.36) in terms of the basis functions:

$$j_{s,z} = \sum_{p=0}^{\infty} \tilde{C}_p^0 \cos(\lambda_z z)\sin(\lambda_x x) \tag{6.45}$$

$$j_{s,x} = \sum_{p=1}^{\infty} \tilde{C}_p^1 \sin(\lambda_z z)\cos(\lambda_x x), \tag{6.46}$$

where the coefficients are obtained in a analogous way and found to be

$$\tilde{C}_p^0 = -\frac{1}{j\omega}\frac{\varepsilon_p}{l_z}(-1)^n(-1)^p \left[\frac{k^2 - \lambda_x^2}{\mu\left(k^2 - k_{mnp}^2\right)} - \frac{k_0^2 - \lambda_x^2}{\mu_0\left(k_0^2 - k_{mnp}^2\right)}\right] \tag{6.47}$$

$$\tilde{C}_p^1 = -\frac{1}{j\omega}\frac{2\pi p \lambda_x}{l_z^2}(-1)^n(-1)^p \left[\frac{1}{\mu\left(k^2 - k_{mnp}^2\right)} - \frac{1}{\mu_0\left(k_0^2 - k_{mnp}^2\right)}\right]. \tag{6.48}$$

S_5 to S_2

On the second xz-oriented face of the cuboid, i.e., S_2 at $y = 0$ (with $\hat{\mathbf{n}} = -\hat{\mathbf{y}}$), the expressions for the surface current density are completely analogous to the one on S_3. Denoting the coefficients for the first set as D_p^0 and D_p^1, the same calculation steps yields

$$D_p^0 = \frac{1}{j\omega}\frac{\varepsilon_p \lambda_x \lambda_y}{l_z}(-1)^p \left[\frac{1}{\mu\left(k^2 - k_{mnp}^2\right)} - \frac{1}{\mu_0\left(k_0^2 - k_{mnp}^2\right)}\right] \tag{6.49}$$

$$D_p^1 = -\frac{1}{j\omega}\frac{2\pi p \lambda_y}{l_z^2}(-1)^p \left[\frac{1}{\mu\left(k^2 - k_{mnp}^2\right)} - \frac{1}{\mu_0\left(k_0^2 - k_{mnp}^2\right)}\right]. \tag{6.50}$$

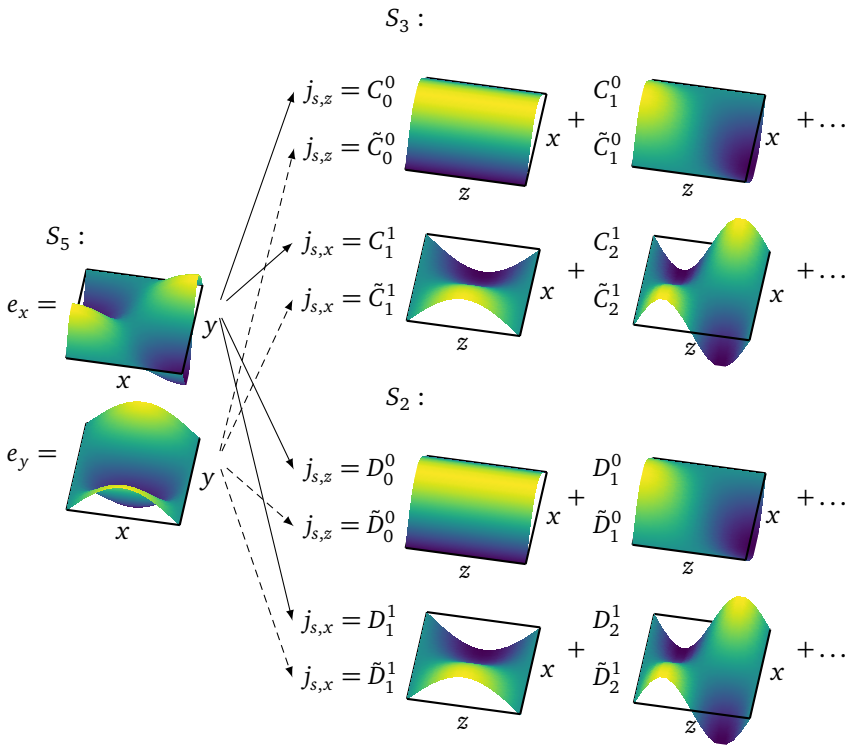

Figure 6.3: Schematic overview of the induced surface current density of set 1 and set 2 on faces S_2 and S_3. In the illustration m and n are set to 1 and 2, respectively.

Comparison with C_p^0 and C_p^1 easily shows that D_p^0 and D_p^1 just differ by a factor $-(-1)^n$ for their counterparts on S_3. As the same applies to the second set, $\tilde{D}_p^0$ and $\tilde{D}_p^1$ are swiftly found to be

$$\tilde{D}_p^0 = \frac{1}{j\omega}\frac{\varepsilon_p}{l_z}(-1)^p \left[\frac{k^2-\lambda_x^2}{\mu\left(k^2-k_{mnp}^2\right)} - \frac{k_0^2-\lambda_x^2}{\mu_0\left(k_0^2-k_{mnp}^2\right)}\right] \tag{6.51}$$

$$\tilde{D}_p^1 = \frac{1}{j\omega}\frac{2\pi p\lambda_x}{l_z^2}(-1)^p \left[\frac{1}{\mu\left(k^2-k_{mnp}^2\right)} - \frac{1}{\mu_0\left(k_0^2-k_{mnp}^2\right)}\right]. \tag{6.52}$$

The relation between the coefficients on faces S_3 and S_2 for both sets of electric fields on S_5 are represented in Fig. 6.3. Once more, we see clear similarities with the expressions obtained in Section 5.4.1. For surface current densities on perpendicular faces, the relation for the expansion coefficients described in (5.53) feature

a similar infinite sum as shown on faces S_3 and S_2 in Fig. 6.3 while the coefficients themselves take analogous forms if $\mu = \mu_0$.

S_5 to S_1

Addressing the penultimate cuboid face S_1 positioned at $x = l_x$ with its outward pointing normal $\hat{\mathbf{x}}$, we compute the surface current densities similarly to the ones on S_3, producing the following expressions for the first set

$$j_{s,y} = -\frac{1}{j\omega}\lambda_y \cos\left(\lambda_y y\right)(-1)^m \left[\frac{\sin(\gamma z)}{\mu \sin(\gamma l_z)} - \frac{\sin(\gamma_0 z)}{\mu_0 \sin(\gamma_0 l_z)}\right] \tag{6.53}$$

$$j_{s,z} = -\frac{1}{j\omega}\sin\left(\lambda_y y\right)(-1)^n \left[\frac{k^2-\lambda_y^2}{\mu\gamma}\frac{\cos(\gamma z)}{\sin(\gamma l_z)} - \frac{k_0^2-\lambda_y^2}{\mu_o\gamma_0}\frac{\cos(\gamma_0 z)}{\sin(\gamma_0 l_z)}\right], \tag{6.54}$$

while the excited $\mathbf{j}_s$ for the second set is

$$j_{s,y} = \frac{1}{j\omega}\lambda_x \cos\left(\lambda_y y\right)(-1)^m \left[\frac{\sin(\gamma z)}{\mu \sin(\gamma l_z)} - \frac{\sin(\gamma_0 z)}{\mu_0 \sin(\gamma_0 l_z)}\right] \tag{6.55}$$

$$j_{s,z} = -\frac{1}{j\omega}\lambda_x\lambda_y \sin\left(\lambda_y y\right)(-1)^m \left[\frac{\cos(\gamma z)}{\mu\gamma \sin(\gamma l_z)} - \frac{\cos(\gamma_0 z)}{\mu_0\gamma_0 \sin(\gamma_0 l_z)}\right]. \tag{6.56}$$

Once again, the entire domain basis functions our not directly present in the obtained expressions but by employing the Fourier series (6.37)–(6.38), the surface current density is cast into its desired shape:

$$j_{s,y} = \sum_{p=1}^{\infty} E_p^0 \cos\left(\lambda_y y\right)\sin(\lambda_z z) \tag{6.57}$$

$$j_{s,z} = \sum_{p=0}^{\infty} E_p^1 \sin\left(\lambda_y y\right)\cos(\lambda_z z)\,. \tag{6.58}$$

The coefficients themselves are defined as

$$E_p^0 = -\frac{1}{j\omega}\frac{2\pi p\lambda_y}{l_z^2}(-1)^m(-1)^p \left[\frac{1}{\mu\left(k^2-k_{mnp}^2\right)} - \frac{1}{\mu_0\left(k_0^2-k_{mnp}^2\right)}\right] \tag{6.59}$$

$$E_p^1 = -\frac{1}{j\omega}\frac{\varepsilon_p}{l_z}(-1)^n(-1)^p \left[\frac{k^2-\lambda_y^2}{\mu\left(k^2-k_{mnp}^2\right)} - \frac{k_0^2-\lambda_y^2}{\mu_0\left(k_0^2-k_{mnp}^2\right)}\right]. \tag{6.60}$$

Following the same scheme for the second set, we find

$$j_{s,y} = \sum_{p=1}^{\infty} \tilde{E}_p^0 \cos\left(\lambda_y y\right)\sin(\lambda_z z) \tag{6.61}$$

$$j_{s,z} = \sum_{p=0}^{\infty} \tilde{E}_p^1 \sin\left(\lambda_y y\right)\cos(\lambda_z z)\,, \tag{6.62}$$

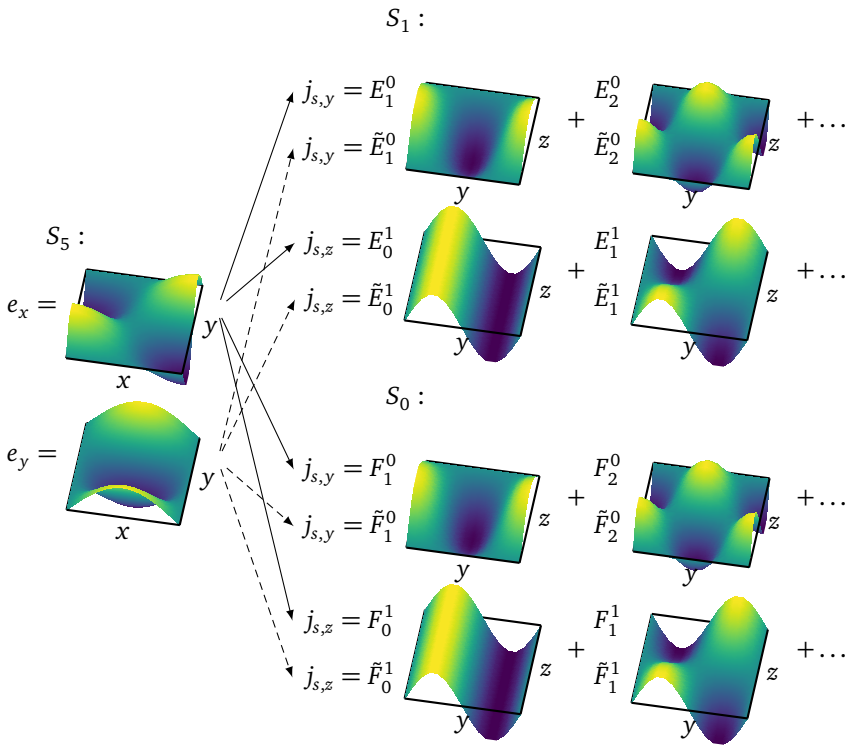

Figure 6.4: Schematic overview of the induced surface current density of set 1 and set 2 on faces S_0 and S_1. In the illustration m and n are set to 1 and 2, respectively.

with $\tilde{E}_p^0$ and $\tilde{E}_p^0$ expressed as

$$\tilde{E}_p^0 = \frac{1}{j\omega}\frac{2\pi p\lambda_x}{l_z^2}(-1)^m(-1)^p\left[\frac{1}{\mu\left(k^2-k_{mnp}^2\right)}-\frac{1}{\mu_0\left(k_0^2-k_{mnp}^2\right)}\right] \tag{6.63}$$

$$\tilde{E}_p^1 = -\frac{1}{j\omega}\frac{\varepsilon_p\lambda_x\lambda_y}{l_z}(-1)^m(-1)^p\left[\frac{1}{\mu\left(k^2-k_{mnp}^2\right)}-\frac{1}{\mu_0\left(k_0^2-k_{mnp}^2\right)}\right]. \tag{6.64}$$

Comparing the coefficients on this face with the ones on S_3, we clearly see some striking parallels. E_p^0 and E_p^1 equal $\tilde{C}_p^1$ and $\tilde{C}_p^0$, respectively, provided that the substitutions $\lambda_x \leftrightarrow \lambda_y$ and $m \leftrightarrow n$ are introduced. The same relations hold for $\tilde{E}_p^0$ and $\tilde{E}_p^1$ on the one hand, and for C_p^1 and C_p^0 on the other hand.

S_5 **to** S_0

Just as it was the case for the faces S_3 and S_2, the coefficients for S_0 are easily deduced as they only differ by a factor $-(-1)^m$ from their counterparts on S_1. Hence, the coefficients governing the surface current density on this final face are

$$F^0 = \frac{1}{j\omega}\frac{2\pi p\lambda_y}{l_z^2}(-1)^p\left[\frac{1}{\mu\left(k^2-k_{mnp}^2\right)}-\frac{1}{\mu_0\left(k_0^2-k_{mnp}^2\right)}\right] \tag{6.65}$$

$$F^1 = \frac{1}{j\omega}\frac{\varepsilon_p}{l_z}(-1)^p\left[\frac{k^2-\lambda_y^2}{\mu\left(k^2-k_{mnp}^2\right)}-\frac{k_0^2-\lambda_y^2}{\mu_0\left(k_0^2-k_{mnp}^2\right)}\right], \tag{6.66}$$

for the first set, while the ones for the second are expressed as

$$\tilde{F}_p^0 = -\frac{1}{j\omega}\frac{2\pi p\lambda_x}{l_z^2}(-1)^p\left[\frac{1}{\mu\left(k^2-k_{mnp}^2\right)}-\frac{1}{\mu_0\left(k_0^2-k_{mnp}^2\right)}\right] \tag{6.67}$$

$$\tilde{F}_p^1 = \frac{1}{j\omega}\frac{\varepsilon_p\lambda_x\lambda_y}{l_z}(-1)^p\left[\frac{1}{\mu\left(k^2-k_{mnp}^2\right)}-\frac{1}{\mu_0\left(k_0^2-k_{mnp}^2\right)}\right]. \tag{6.68}$$

The various coefficients on these last two faces are also shown schematically in Fig. 6.4.

6.4 Conclusions

An extension of the 3-D differential surface admittance operator for cuboids was presented in this chapter. By expressing the operator directly as the difference between two Poincaré-Steklov operators, the restriction on nonmagnetic materials was lifted. We then calculated both operators by means of the superposition principle where the entire cuboid was tackled as the combination of six rectangular waveguides with one of its open ends metallized. By expanding the electric field and surface current density in entire domain basis functions, we derived explicit expressions for the differential surface admittance operator in one of the six cases in the superposition. Given that the other scenarios result in completely analogous expressions, the differential surface admittance operator for combined magnetic and dielectric contrast has been fully defined for cuboids.

References

[1] C. Paul, *Introduction to Electromagnetic Compatibility*, ser. Wiley Series in Microwave and Optical Engineering. Wiley, 2006.

7 Conclusion

"Still round the corner there may wait
A new road or a secret gate,
And though we pass them by today,
Tomorrow we may come this way"

J.R.R. Tolkien

7.1 Conclusions

In this dissertation, we have presented a novel method to accurately model arbitrary homogeneous materials in a three-dimensional (3-D) boundary integral equation (BIE) context. The advocated differential surface admittance operator (based on eigenfunctions) has proven, in particular, to efficiently model good conductors over a broad frequency range, from direct current (DC) to the strong skin effect regime. The method has been demonstrated and applied to scattering and antenna problems for cylinders and to interconnect structures composed of cuboids. Through a diverse number of experiments and comparisons with academic state-of-the-art methods and commercial industry-standard solvers, we have verified that the inclusion of the differential surface admittance operator into a BIE method provides accurate and consistent results in various applications. Hence, its appositeness and validity in modeling phenomena related to good conductors, such as the skin and proximity effect, was demonstrated.

In Chapter 3, the concept of the differential surface admittance operator in 3-D was introduced based on the equivalence principle and the Poincaré-Steklov operator. An expression for the differential operator based on the eigenfunctions of the volume has been introduced. This construction method avoids the (numerical) integration of the Green's function in the homogeneous material, which can be

a computationally heavy burden. The operator has been employed to scattering problems and antenna configurations involving cylinders in Chapter 4. To construct an efficient surface mesh, conserving the curved nature of the mantle of the cylinder, a special set of basis functions, i.e., curved rooftops, was developed first. The integrals required for singularity extraction on these curved patches were presented as well. By calculating the eigenfunctions of the cylinder and discretizing the differential surface admittance operator, all the while profiting from the special basis functions, a full BIE solution was obtained. Afterwards, we studied the broadband properties of the discretized operator's elements and commented on their convergence behavior. Additionally, the new method was compared to an established BIE-Method of Moments (MoM) solver for scattering problems at various materials and to a freeware antenna modeller for assessing characteristics of different antennas with varying conductivity values.

Throughout Chapter 5, the modeling of 3-D interconnects was the central goal. Accordingly, we presented two boundary element methods (BEMs) that incorporate the differential surface admittance operator and the electric field integral equation (EFIE). The first formulation enabled broadband calculation of the resistance and inductance of interconnect structures by constructing a circuit interpretation of the equations that was subsequently solved with a traditional circuit solver. The second interpretation was based on the augmented EFIE and provides a set of matrix equations that, solved jointly, provide a full-wave characterization. Two different techniques to construct the differential surface admittance operator for cuboids were discussed as well. On the one hand, the continuous operator was directly discretized with local basis functions. On the other hand, an intermediate discretization with entire domain basis functions resulted in an alternative formulation that, through closed sums of infinite series, gives a differential surface admittance matrix with improved accuracy and convergence properties. Afterwards, both BEMs and differential operator formulations were tested extensively by comparison with ample reference results. Lastly, various applications examples were studied, comparing with commercial solvers, academic state-of-the-art methods and measurements. In Chapter 6, the differential surface admittance operator for cuboids was revisited once more. By tackling it directly as the difference between two Poincaré-Steklov operators, each calculated through the superposition of six perfect electric conductor (PEC) waveguides with one metallized end, materials with both a dielectric and a magnetic contrast can be included.

As a final remark, we summarize the advantages and drawbacks of the 3-D differential surface admittance operator as presented in this work. Its main advantage is the fact that the skin effect can be captured accurately without having to rely on the laborious integrals of the Green's function in the conductive medium or without having to resort to approximations. This results in a broadband accurate characterization of any nonmagnetic homogeneous material. The calculation method based on the entire domain basis function derived for the cuboid in Chapter 5 increases the efficiency considerably by its use of analytical sums of infinite series, thus reducing the number of required eigenmodes for accurate results. This

number also provide a convenient control mechanism: for increased accuracy one can easily include more eigenmodes. Moreover, there is no need for a complete recalculation as the entries for the additional eigenfunctions can just be added to the initial differential surface admittance matrix. The major drawback of this operator is the fact that the eigenmodes are only easily calculated for a handful of canonical shapes. Given the generally modest to large number of eigenmodes needed to achieve satisfactory precision, shapes for which the eigenfunctions can only be calculated numerically will in all likelihood lead to unacceptably long computation times. Nonetheless, the two shapes demonstrated in this work, i.e., cylinders and cuboids, make up a very large fraction of the encountered building blocks in circuits and antenna systems.

7.2 Future work

The techniques and methods proposed and developed in this work encompass the foundations of the 3-D differential surface admittance operator. However, they do not present its end stage; on the contrary, many extensions/improvements could be developed to extend its range of applications and improve its performance. Below we pitch some ideas to accomplish these goals.

7.2.1 The differential surface admittance operator

The theory presented in Chapter 6 for the magnetic differential surface admittance operator for cuboids is untested at the moment. An adaptation of the implementation of the operator expounded in Section 5.4, will effectively implement this extended operator and will open up the way for experiments such as the assessment of the shielding effectiveness of mu-metal enclosures. The same extensions could be realized for cylinders. Not only would this lead to an expansion of the set of calculable materials, this could also improve the convergence properties of the differential surface admittance matrix as some of the infinite series may contains closed sums. It remains to be seen, of course, if this is actually the case for the Bessel functions. Similarly, the differential surface admittance operator could be applied to emerging materials and technologies such as indium tin oxide (ITO) or printed antennas where techniques such as the surface impedance approach are less appropriate.

In two dimensions, the differential surface admittance operator has been constructed for various shapes, i.e., rectangles, circles, tubes and triangles. It would be very interesting to extend the arsenal of the 3-D operator as well. Spheres can model solder bumps, tubes represent drilled and plated vias and triangular prisms would enable the study of arbitrary angled bends (without resorting to approximations) and over-/underetched structures.

The current implementation of the differential operator could be improved upon considerably as well. The triple and double sums in the expressions for the cuboids

and cylinders lends themselves extremely well to multithreading and/or parallelization. So far, this property has not been exploited in the simulations. Moreover, the entire program in its actual state is written in an interpreted programming language. By porting some parts or the entire code to a compiled language, the efficiency of the program could be improved.

7.2.2 The boundary integral equation

The problems studied in this work are relatively speaking quite small in terms of number of unknowns. If the developed code is to be employed to model entire boards or complex integrated circuit (IC) interconnects, the number of unknowns will increase considerably. Due to the block diagonal structure of the differential surface admittance operator, i.e., each block represents the interior problem of a single building block and there is no coupling between different parts, the scaling will affect the MoM matrices the hardest. More efficient and scalable BEMs will have to be used, such as the multilevel fast multipole method (MLFMM). Another complication that can come up is the conditioning of the system matrix. For low frequencies and/or dense meshes, the conditioning number of the EFIE is known to explode, degrading the speed and accuracy of iterative and direct solvers. Possible solutions lie in the rescaling of the matrix equations/unknowns as presented before for the augmented EFIE or the use of (Calderón) preconditioners.

Larger problems or more intricate structures will also entail additional connections between different building blocks. So far, these connections have been realized as small PEC wires. For general applications, however, a more rigorous approach to these junctions might be required. At the same time, the need will arise to combine the cylinders and cuboids to model structures, such as there are, vias with a feed structure. In more realistic simulations, the influence of the substrate cannot be ignored either. As such, the inclusion of the Green's function for layered media will extend the applicability of the presented techniques.

Just like it is the case with the differential surface admittance operator, the actual implementation of the MoM matrices is not optimized for speed but for accuracy and testing flexibility. Optimizing/porting the calculation of the numerical integration of the Green's function could, for example, increase the efficiency considerably, just as exploiting certain symmetries or approximations could reduce the computational burden even further.

A

Singularity Integrals

A.1 Integrals for two curved rectangles

In Section 4.2.2, the singularity extraction procedure for curved rooftops is described. As the basis functions both span two patches, the required integrals can be split into a sum of four contributions, each being a double surface integral over two curved rectangles. Two such patches are shown in Fig. A.1 with the points in each curved rectangle described by its own set of coordinates (ϕ, z) and (ϕ', z'), respectively, with the boundaries given by the coordinates of two diagonally opposite vertices. Note that in cases where singularity extraction is applied, both patches usually either overlap or have a common edge/vertex. Since the expressions obtained below are general, these cases are all covered appropriately.

Before turning our attention to the actual integrals, we define a set of auxiliary

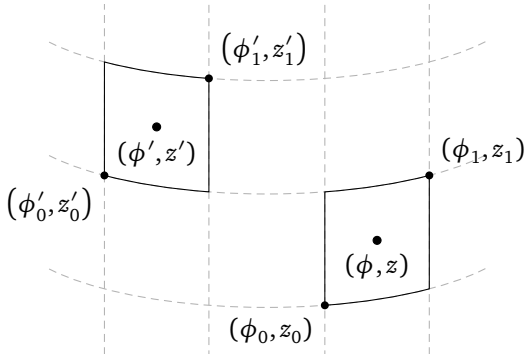

Figure A.1: Illustration of two curved rectangles on the surface of a cylinder.

integrals that are employed in the final expressions.

The first set represents integration of the reciprocal approximate distance measure over a single curved rectangle with $r = \sqrt{p^2 + q^2}$:

$$\alpha(p,q) = \iint \frac{\mathrm{d}q\,\mathrm{d}p}{r} = p\ln(q+r) + q\ln(p+r) \tag{A.1}$$

$$\beta(p,q) = \iint \frac{p\,\mathrm{d}q\,\mathrm{d}p}{r} = \frac{1}{2}\left[p^2\ln(q+r) + qr\right] \tag{A.2}$$

$$\gamma(p,q) = \iint \frac{p^2\,\mathrm{d}q\,\mathrm{d}p}{r} = \frac{1}{6}\left[2p^3\ln(q+r) + pqr - q^3\ln(p+r)\right] \tag{A.3}$$

$$\delta(p,q) = \iint \frac{p^3\,\mathrm{d}q\,\mathrm{d}p}{r} = \frac{1}{12}\left[3p^4\ln(q+r) + qr(p^2 - 2q^2)\right] \tag{A.4}$$

The second set is applied to integration over the second patch with r equaling $r = \sqrt{v^2 + w^2}$ in the expressions below

$$a(v,w) = \iint \alpha(v,w)\,\mathrm{d}w\,\mathrm{d}v = \frac{1}{12}\left[6v^2w\ln(w+r) - 3vw(v+w) + 6w^2v\ln(v+r) - 2(v^2+w^2)r\right] \tag{A.5}$$

$$b(v,w) = \iint v\,\alpha(v,w)\,\mathrm{d}w\,\mathrm{d}v = \frac{1}{144}\left[48v^3w\ln(w+r) - 2v^2w(9w+8v) + 3w^2(12v^2+w^2)\ln(v+r) - 3vr(w^2+6v^2)\right] \tag{A.6}$$

$$c(v,w) = \iint v^2\,\alpha(v,w)\,\mathrm{d}w\,\mathrm{d}v = \frac{1}{720}\left[180v^4w\ln(w+r) - 15v^3w(3v+4w) + 120v^3w^2\ln(v+r) + 4r(2w^4 - 18v^4 - w^2v^2)\right] \tag{A.7}$$

$$d(v,w) = \iint \beta(v,w)\,\mathrm{d}w\,\mathrm{d}v = \frac{1}{72}\left[12v^3w\ln(w+r) - 4v^3w + 3w^4\ln(v+r) + 3vr(3w^2 - 2v^2)\right] \tag{A.8}$$

$$e(v,w) = \iint v\,\beta(v,w)\,\mathrm{d}w\,\mathrm{d}v = \frac{1}{480}\left[60v^4w\ln(w+r) - 15v^4w + 4r(9v^2w^2 + 2w^4 - 8v^4)\right] \tag{A.9}$$

$$f(v,w) = \iint \gamma(v,w)\,\mathrm{d}w\,\mathrm{d}v = \frac{1}{480}\left[40v^4w\ln(w+r) + 5vw(w^3 - 2v^3) - 20vw^4\ln(v+r) + 4r(-6v^4 + 3v^2w^2 + 4w^4)\right] \tag{A.10}$$

$$g(v,w) = \iint v\,\gamma(v,w)\,\mathrm{d}w\,\mathrm{d}v = \frac{1}{4800}\big[320v^5 w\ln(w+r) + v^2 w(-64v^3+25w^3) \\ -10w^4(10v^2+3w^2)\ln(v+r) \\ +10vr(-20v^4+8v^2w^2+3w^4)\big] \tag{A.11}$$

$$h(v,w) = \iint v^2\,\gamma(v,w)\,\mathrm{d}w\,\mathrm{d}v = \frac{1}{30240}\big[1680v^6 w\ln(w+r) \\ -420v^3w^4\ln(v+r) + 35v^3w(-8v^3+3w^3) \\ +4r(-270v^6+93v^4w^2+16v^2w^4-32w^6)\big] \tag{A.12}$$

$$i(v,w) = \iint \delta(v,w)\,\mathrm{d}w\,\mathrm{d}v = \frac{1}{1200}\big[60v^5 w\ln(w+r) - 12v^5 w \\ -15w^6\ln(v+r) + 5vr(-8v^4+2v^2w^2-5w^4)\big] \tag{A.13}$$

$$j(v,w) = \iint v\,\delta(v,w)\,\mathrm{d}w\,\mathrm{d}v = \frac{1}{5040}\big[210v^6 w\ln(w+r) - 35v^6 w \\ +2r(-72v^6+15v^4w^2-34v^2w^4-16w^6)\big] \tag{A.14}$$

The simplest singular integral evaluates the reciprocal of

$$\tilde{R} = \sqrt{\rho^2(\phi-\phi')^2 + (z-z')^2}, \tag{A.15}$$

with ρ the radius of the cylinder, over two curved rectangles and originates from the contribution of the scalar potential to the MoM system matrix:

$$I_0 = \int_{\phi_0}^{\phi_1}\int_{z_0}^{z_1}\int_{\phi_0'}^{\phi_1'}\int_{z_0'}^{z_1'} \frac{1}{\tilde{R}}\rho^2\,\mathrm{d}z'\,\mathrm{d}\phi'\,\mathrm{d}z\,\mathrm{d}\phi. \tag{A.16}$$

Performing the substitutions $p = \rho(\phi-\phi')$ and $q = (z-z')$, the double inner integral is transformed into (A.1), thus leading to

$$I_0 = \sum_{k,l=0}^{1}(-1)^{k+l}\int_{\phi_0}^{\phi_1}\int_{z_0}^{z_1}\alpha\big(\rho(\phi-\phi_k'),(z-z_l')\big)\rho\,\mathrm{d}z\,\mathrm{d}\phi. \tag{A.17}$$

The second set of substitutions $v = \rho\left(\phi-\phi_k'\right)$ and $w = \left(z-z_l'\right)$ shows that the last pair of integrals can be written as (A.5), yielding the following expression

$$I_0 = \sum_{i,j,k,l=0}^{1}(-1)^{i+j+k+l}a\left(\rho\Phi_{ik}, Z_{jl}\right), \tag{A.18}$$

with the shorthand notations $\Phi_{ik} = \phi_i - \phi'_k$ and $Z_{jl} = z_j - z'_l$.

In interactions involving z-directed rooftops (see (4.2)) factors of the form $(z - z_a)\left(z' - z'_a\right)$ appear in the numerator of the integrand with the z_a and z'_a constants equal to either of the boundary values of z/z' on their respective curved rectangle. These constants originate from the definitions of the rooftops, cf. $z_j^{\pm}$ in (4.2). The integral to be calculated thus is

$$I_z = \int_{\phi_0}^{\phi_1}\int_{z_0}^{z_1}\int_{\phi'_0}^{\phi'_1}\int_{z'_0}^{z'_1} \frac{(z - z_a)\left(z' - z'_a\right)}{\tilde{R}} \rho^2 \,\mathrm{d}z' \,\mathrm{d}\phi' \,\mathrm{d}z \,\mathrm{d}\phi. \tag{A.19}$$

Introducing the same substitutions as before, enables us to rewrite this expression, with the aid of (A.1)–(A.2), as

$$I_z = \int_{\phi_0}^{\phi_1}\int_{z_0}^{z_1}\int_{\phi-\phi'_0}^{\phi-\phi'_1}\int_{z-z'_0}^{z-z'_1} \frac{(z - z_a)\left(z - z'_a\right) - q\,(z - z_a)}{\tilde{R}} \rho \,\mathrm{d}q \,\mathrm{d}p \,\mathrm{d}z \,\mathrm{d}\phi. \tag{A.20}$$

$$= \sum_{k,l=0}^{1} (-1)^{k+l} \int_{\phi_0}^{\phi_1}\int_{z_0}^{z_1} \begin{array}{l} (z - z_a)\left(z - z'_a\right) \alpha\left((z - z'_l), \rho(\phi - \phi'_k)\right) \\ -(z - z_a)\,\beta\left((z - z'_l), \rho(\phi - \phi'_k)\right) \rho \end{array} \mathrm{d}z \,\mathrm{d}\phi \quad . \tag{A.21}$$

The last two integrals are transformed by means of the second set of substitutions and through (A.5)–(A.9) this yields

$$\begin{aligned} I_z = \sum_{i,j,k,l=0}^{1} (-1)^{i+j+k+l} \big[& \left(z'_l - z_a\right)\left(z'_l - z'_a\right) a\left(Z_{jl}, \rho\Phi_{ik}\right) \\ & + \left(2z'_l - z_a - z'_a\right) b\left(Z_{jl}, \rho\Phi_{ik}\right) + c\left(Z_{jl}, \rho\Phi_{ik}\right) \\ & - \left(z'_l - z_a\right) d\left(Z_{jl}, \rho\Phi_{ik}\right) - e\left(Z_{jl}, \rho\Phi_{ik}\right) \big]. \end{aligned} \tag{A.22}$$

For the ϕ-oriented rooftops (see (4.3)), $(\phi - \phi_a)\left(\phi' - \phi'_a\right)$ is the relevant factor, given the zeroth order approximation of $\cos(\phi - \phi')$ as described in Section 4.2.2. This leads to the integral

$$I_\phi = \int_{\phi_0}^{\phi_1}\int_{z_0}^{z_1}\int_{\phi'_0}^{\phi'_1}\int_{z'_0}^{z'_1} \frac{(\phi - \phi_a)\left(\phi' - \phi'_a\right)}{\tilde{R}} \rho^2 \,\mathrm{d}z' \,\mathrm{d}\phi' \,\mathrm{d}z \,\mathrm{d}\phi. \tag{A.23}$$

With the same substitutions as performed in the previous derivation, but taking

the appropriate powers of ρ into account, the end result is

$$I_\phi = \frac{1}{\rho^2}\sum_{i,j,k,l=0}^{1}(-1)^{i+j+k+l}\Big[\rho^2\left(\phi'_k-\phi_a\right)\left(\phi'_k-\phi'_a\right)a\left(\rho\Phi_{ik},Z_{jl}\right) \\ +\rho\left(2\phi'_k-\phi_a-\phi'_a\right)b\left(\rho\Phi_{ik},Z_{jl}\right)+c\left(\rho\Phi_{ik},Z_{jl}\right) \\ -\rho\left(\phi'_k-\phi_a\right)d\left(\rho\Phi_{ik},Z_{jl}\right)-e\left(\rho\Phi_{ik},Z_{jl}\right)\Big]. \tag{A.24}$$

For the second order approximation of the cosine, the relevant integral is of the form

$$I_{\phi,2} = \int_{\phi_0}^{\phi_1}\int_{z_0}^{z_1}\int_{\phi'_0}^{\phi'_1}\int_{z'_0}^{z'_1}\frac{(\phi-\phi_a)\left(\phi'-\phi'_a\right)(\phi-\phi')^2}{\tilde{R}}\rho^2\,\mathrm{d}z'\,\mathrm{d}\phi'\,\mathrm{d}z\,\mathrm{d}\phi. \tag{A.25}$$

Utilizing the change of variables p and q and (A.3)–(A.4), the intermediate result is

$$I_{\phi,2} = \frac{1}{\rho^3}\sum_{k,l=0}^{1}(-1)^{k+l}\int_{\phi_0}^{\phi_1}\int_{z_0}^{z_1}\rho\,(\phi-\phi_a)\left(\phi-\phi'_a\right)\gamma\left(\rho(\phi-\phi'_k),(z-z'_l)\right) \\ -(\phi-\phi_a)\,\delta\left(\rho(\phi-\phi'_k),(z-z'_l)\right)\rho\,\mathrm{d}z\,\mathrm{d}\phi \tag{A.26}$$

Through (A.10)–(A.14), the complete expression becomes

$$I_{\phi,2} = \frac{1}{\rho^4}\sum_{i,j,k,l=0}^{1}(-1)^{i+j+k+l}\Big[\rho^2\left(\phi'_k-\phi_a\right)\left(\phi'_k-\phi'_a\right)f\left(\rho\Phi_{ik},Z_{jl}\right) \\ +\rho\left(2\phi'_k-\phi_a-\phi'_a\right)g\left(\rho\Phi_{ik},Z_{jl}\right)+h\left(\rho\Phi_{ik},Z_{jl}\right) \\ -\rho\left(\phi'_k-\phi_a\right)i\left(\rho\Phi_{ik},Z_{jl}\right)-j\left(\rho\Phi_{ik},Z_{jl}\right)\Big]. \tag{A.27}$$

A.2 Integrals for two rectangles in parallel planes

In Section 5.2.2, we expounded the approach employed for singular integrals in case of a rectangular mesh. In this section, singularity extraction for rectangles in parallel planes is tackled while the next section deals with rectangles in perpendicular planes. As the basis functions both span two patches, the required integrals can be split into a sum of four contributions, each being a double surface integral over two rectangles. Two such patches are shown in Fig. A.2 with the points in each rectangles described by its own set of coordinates $(x,y,0)$ and (x',y',a), respectively, with the boundaries given by the coordinates of two diagonally opposite vertices. Remark that we have opted for two patches in parallel xy-planes.

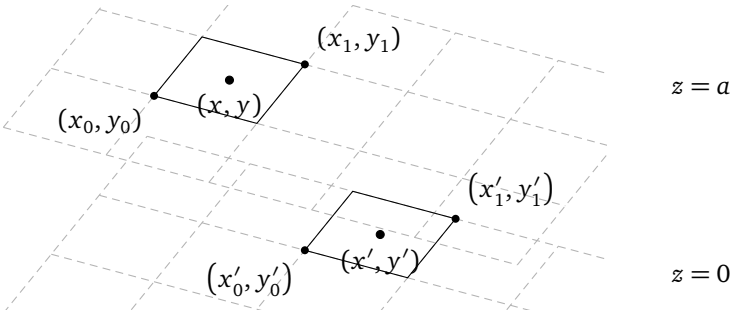

Figure A.2: Illustration of two rectangles in parallel planes spaced a apart.

For other orientations, the same results can be used with the roles of the various coordinates reversed. Note that in cases where singularity extraction is applied, both patches usually either overlap or have a common edge/vertex. Since the expressions obtained below are general, these cases are all covered appropriately.

Before turning our attention to the actual integrals, we define a set of auxiliary integrals that are employed in the final expressions.

The first set represents integration of the reciprocal distance measure over a single rectangle with $r = \sqrt{p^2 + q^2 + a^2}$:

$$\alpha(p,q) = \iint \frac{\mathrm{d}q\,\mathrm{d}p}{r} = p\ln(q+r) + q\ln(p+r) - q + a\arctan\left(\frac{q}{a}\right) - a\arctan\left(\frac{pq}{ar}\right) \tag{A.28}$$

$$\beta(p,q) = \iint \frac{p\,\mathrm{d}q\,\mathrm{d}p}{r} = \frac{1}{4}\left[2\left(p^2+a^2\right)\ln(q+r) + 2qr - a^2\right] \tag{A.29}$$

The second set is applied to integration over the second patch with r equaling $r = \sqrt{v^2 + w^2 + a^2}$ in the expressions below

$$\begin{aligned} a(v,w) &= \iint \alpha(v,w)\,\mathrm{d}w\,\mathrm{d}v \\ &= \frac{1}{12}\Big[6\left(v^2+a^2\right)w\ln(w+r) - 3vw(v+w) \\ &\quad +6\left(w^2+a^2\right)v\ln(v+r) - 2(v^2+w^2-2a^2)r \\ &\quad -6va^2\ln(w^2+a^2) + 12vwh\arctan\left(\frac{w}{a}\right) - 12vwa\arctan\left(\frac{vw}{ar}\right) \\ &\quad -12va^2\operatorname{arctanh}\left(\frac{v}{r}\right) - 12wa^2\operatorname{arctanh}\left(\frac{w}{r}\right)\Big] \end{aligned} \tag{A.30}$$

$$
\begin{aligned}
b(v,w) &= \iint v\alpha(v,w)\,\mathrm{d}w\,\mathrm{d}v \qquad \text{(A.31)}\\
&= \frac{1}{144}\Big[48v^3 w\ln(w+r)+2vw\left(-8v^2-27vw+24a^2\right)\\
&+3\left(w^4+12v^2w^2+6w^2a^2+12a^2v^2-3a^4\right)\ln(v+r)\\
&+3vr\left(-6v^2-w^2+3a^2\right)-36v^2a^2\ln\left(w^2+a^2\right)\\
&-24wa\left(3v^2+a^2\right)\arctan\left(\frac{vw}{ar}\right)-72v^2a^2\operatorname{arctanh}\left(\frac{v}{r}\right)\\
&-48wa^3\arctan\left(\frac{v}{a}\right)+72v^2wa\arctan\left(\frac{w}{a}\right)\Big]\\
c(v,w) &= \iint v^2\,\alpha(v,w)\,\mathrm{d}w\,\mathrm{d}v \qquad \text{(A.32)}\\
&= \frac{1}{720}\Big[180\left(v^4-a^4\right)w\ln(w+r)+120\left(w^2+a^2\right)v^3\ln(v+r)\\
&-120v^3a^2\ln\left(w^2+a^2\right)-15v^2w\left(3v^2+12vw-6a^2\right)\\
&+4r\left(-18v^4+2w^4-w^2v^2+4a^2v^2+9a^2w^2-8a^4\right)\\
&-240v^3wa\arctan\left(\frac{vw}{ar}\right)+240v^3wa\arctan\left(\frac{w}{a}\right)\\
&+240wa^4\operatorname{arctanh}\left(\frac{w}{r}\right)-240v^3a^2\operatorname{arctanh}\left(\frac{v}{r}\right)\Big]\\
d(v,w) &= \iint \beta(v,w)\,\mathrm{d}w\,\mathrm{d}v \qquad \text{(A.33)}\\
&= \frac{1}{72}\Big[12vw\left(v^2+3a^2\right)\ln(w+r)-4vw\left(v^2+6a^2\right)\\
&+3\left(w^4+6w^2a^2-3a^4\right)\ln(v+r)-3vr\left(2v^2-3w^2+5a^2\right)\\
&-24wa^3\arctan\left(\frac{vw}{ar}\right)+24wa^3\arctan\left(\frac{v}{a}\right)\Big]\\
e(v,w) &= \iint v\,\beta(v,w)\,\mathrm{d}w\,\mathrm{d}v \qquad \text{(A.34)}\\
&= \frac{1}{480}\Big[60\left(v^2+a^2\right)^2 w\ln(w+r)-15v^2w\left(v^2+2a^2\right)\\
&-60w^4r+100w^2r^3-32r^5\Big]
\end{aligned}
$$

Note that these auxiliary functions reduce to (A.5)–(A.10) for $a \to 0$.

The simplest singular integral evaluates the reciprocal of

$$R = \sqrt{(x-x')^2+(y-y')^2+a^2}, \qquad \text{(A.35)}$$

with a the distance between both planes, over two rectangles and originates from

the contribution of the scalar potential to the MoM system matrix:

$$I_0 = \int_{x_0}^{x_1}\int_{y_0}^{y_1}\int_{x_0'}^{x_1'}\int_{y_0'}^{y_1'} \frac{1}{R}\,\mathrm{d}y'\,\mathrm{d}x'\,\mathrm{d}y\,\mathrm{d}x. \tag{A.36}$$

Performing the substitutions $p = (x - x')$ and $q = (y - y')$, the double inner integral is transformed into (A.28), thus leading to

$$I_0 = \sum_{k,l=0}^{1} (-1)^{k+l} \int_{x_0}^{x_1}\int_{y_0}^{y_1} \alpha\left((x - x_k'), (y - y_l')\right)\,\mathrm{d}y\,\mathrm{d}x. \tag{A.37}$$

The second set of substitutions $v = \left(x - x_k'\right)$ and $w = \left(y - y_l'\right)$ shows that the last pair of integral can be written as (A.30), yielding the following expression

$$I_0 = \sum_{i,j,k,l=0}^{1} (-1)^{i+j+k+l} a\left(X_{ik}, Y_{jl}\right), \tag{A.38}$$

with the shorthand notations $X_{ik} = x_i - x_k'$ and $Y_{jl} = y_j - y_l'$.

In interactions involving x-directed rooftops factors of the form $(x - x_a)\left(x' - x_a'\right)$ appear in the numerator of the integrand with the x_a and x_a' constants equal to either of the boundary values of x/x' on their respective rectangle. These constants originate from the definitions of the rooftops, cf. $\mathbf{r}_j^{\pm}$ in (2.45). By exchanging the roles of x and y the relevant results for y-oriented rooftops are obtained. The integral to be calculated is thus

$$I_x = \int_{x_0}^{x_1}\int_{y_0}^{y_1}\int_{x_0'}^{x_1'}\int_{y_0'}^{y_1'} \frac{(x - x_a)\left(x' - x_a'\right)}{R}\,\mathrm{d}y'\,\mathrm{d}x'\,\mathrm{d}y\,\mathrm{d}x. \tag{A.39}$$

Introducing the same substitutions as before, enables us to rewrite this expression, with the aid of (A.28)–(A.29), as

$$I_x = \int_{x_0}^{x_1}\int_{y_0}^{y_1}\int_{x-x_0'}^{x-x_1'}\int_{y-y_0'}^{y-y_1'} \frac{(x - x_a)\left(x - x_a'\right) - q\,(x - x_a)}{R}\,\mathrm{d}q\,\mathrm{d}p\,\mathrm{d}y\,\mathrm{d}x. \tag{A.40}$$

$$= \sum_{k,l=0}^{1} (-1)^{k+l} \int_{x_0}^{x_1}\int_{y_0}^{y_1} \begin{array}{l} (x - x_a)\left(x - x_a'\right)\alpha\left((x - x_k'), (y - y_l')\right) \\ -(x - x_a)\,\beta\left((x - x_k'), (y - y_l')\right)\,\mathrm{d}y\,\mathrm{d}x. \end{array} \tag{A.41}$$

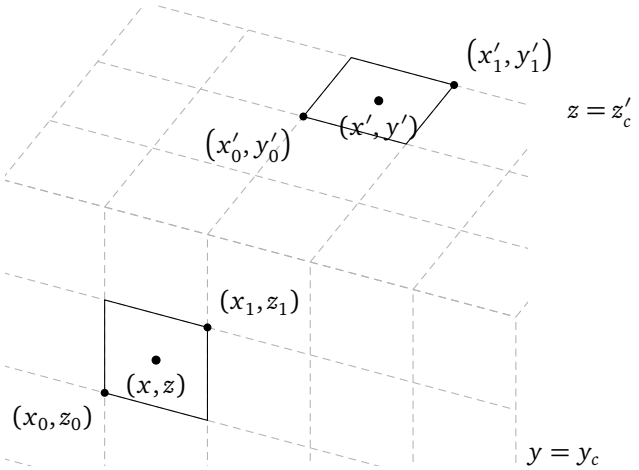

Figure A.3: Illustration of two rectangles in perpendicular planes.

The last two integrals are transformed by means of the second set of substitutions and through (A.30)–(A.34) this yields

$$I_x = \sum_{i,j,k,l=0}^{1} (-1)^{i+j+k+l} \Big[\big(x_l' - x_a\big)\big(x_l' - x_a'\big)\, a\big(X_{ik}, Y_{jl}\big) + \big(2x_l' - x_a - x_a'\big)\, b\big(X_{ik}, Y_{jl}\big) + c\big(X_{ik}, Y_{jl}\big) - \big(x_l' - x_a\big)\, d\big(X_{ik}, Y_{jl}\big) - e\big(X_{ik}, Y_{jl}\big) \Big]. \tag{A.42}$$

A.3 Integrals for two rectangles in perpendicular planes

In the previous section, we explored the singular integrals for two rectangles in parallel planes. Here we will take a closer look at two rectangles in perpendicular planes. To this end, we examine the situations shown in Fig. A.3. One rectangle, with coordinates (x', y'), lies in an xy-plane (with $z = z_c'$), while to other one is situated in an xz-plane (with $y = y_c$) and has coordinates (x, z). For other configurations/orientations, the results can be found by making the appropriate substitutions/permutations of the coordinates. Note that in cases where singularity extraction is applied, both patches usually either have a common edge/vertex. Since the expressions obtained below are general, these cases are all covered appropriately.

Before turning our attention to the actual integrals, we define a set of auxiliary integrals that are employed in the final expressions.

The first set represents integration of the reciprocal distance measure over a single rectangle with $r = \sqrt{p^2+q^2+a^2}$:

$$\alpha(p,q,a) = \iint \frac{\mathrm{d}q\,\mathrm{d}p}{r} = p\ln(q+r) + q\ln(p+r) - q - a\arctan\left(\frac{pq}{ar}\right) \tag{A.43}$$

$$\beta(p,q,a) = \iint \frac{p\,\mathrm{d}q\,\mathrm{d}p}{r} = \frac{1}{2}\left[\left(p^2+a^2\right)\ln(q+r) + qr\right] \tag{A.44}$$

The second set is applied to integration over the second patch with r equaling $r = \sqrt{v^2+w^2+b^2}$ in the expressions below (note the change of the order of variables in the integrand):

$$\begin{aligned} a(v,b,w) &= \iint \alpha(v,b,w)\,\mathrm{d}w\,\mathrm{d}v \\ &= \frac{1}{12}\left[12vwb\ln(v+r) + 2b\left(3v^2-b^2\right)\ln(w+r) - 18vwb - 4wbr\right. \\ &+2w\left(3v^2+w^2\right)\ln(b+r) - 6v\left(w^2-b^2\right)\arctan\left(\frac{w}{b}\right) - 4w^3\,\mathrm{arctanh}\left(\frac{b}{r}\right) \\ &\left.-2v^3\arctan\left(\frac{bw}{vr}\right) - 6vw^2\arctan\left(\frac{bv}{wr}\right) - 6vb^2\arctan\left(\frac{vw}{br}\right)\right] \end{aligned} \tag{A.45}$$

$$\begin{aligned} b(v,b,w) &= \iint v\alpha(v,b,w)\,\mathrm{d}w\,\mathrm{d}v \\ &= \frac{1}{24}\left[2wb\left(6v^2+w^2+b^2\right)\ln(v+r) + 8v^3b\ln(w+r) - 18v^2wb - vwbr\right. \\ &+8v^3w\ln(b+r) - 6v^2\left(w^2-b^2\right)\arctan\left(\frac{w}{b}\right) - 3v^4\arctan\left(\frac{bw}{vr}\right) \\ &\left.-w^2\left(6v^2+w^2\right)\arctan\left(\frac{bv}{wr}\right) - b^2\left(6v^2+b^2\right)\arctan\left(\frac{vw}{br}\right)\right] \end{aligned} \tag{A.46}$$

$$\begin{aligned} c(v,b,w) &= \iint v^2\,\alpha(v,b,w)\,\mathrm{d}w\,\mathrm{d}v \\ &= \frac{1}{180}\left[60v^3wb\ln(v+r) + 3b\left(15v^4+b^4\right)\ln(w+r)\right. \\ &+9w\left(5v^4-w^4\right)\ln(b+r) + wbr\left(-2v^2+7w^2+7b^2\right) - 90v^3wb \\ &+12w^5\,\mathrm{arctanh}\left(\frac{b}{r}\right) - 18v^5\arctan\left(\frac{bw}{vr}\right) - 30v^3w^2\arctan\left(\frac{vb}{wr}\right) \\ &\left.-30v^3\left(w^2-b^2\right)\arctan\left(\frac{w}{b}\right) - 30v^3b^2\arctan\left(\frac{vw}{br}\right)\right] \end{aligned} \tag{A.47}$$

$$
\begin{aligned}
d(v,b,w) &= \iint \beta(v,b,w)\,\mathrm{d}w\,\mathrm{d}v \qquad (A.48)\\
&= \frac{1}{36}\Big[6wb\left(w^2+b^2\right)\ln(v+r)+6vb\left(v^2+b^2\right)\ln(w+r)\\
&\quad +6vw\left(v^2+w^2\right)\ln(b+r)+9vwbr-3v^4\arctan\left(\frac{bw}{vr}\right)\\
&\quad -3w^4\arctan\left(\frac{bv}{wr}\right)-3b^4\arctan\left(\frac{vw}{br}\right)\Big]\\
e(v,b,w) &= \iint v\,\beta(v,b,w)\,\mathrm{d}w\,\mathrm{d}v\\
&= \frac{1}{120}\Big[b\left(15v^4+10v^2b^2+3b^4\right)\ln(w+r)-8v^5\arctan\left(\frac{bw}{vr}\right)\\
&\quad +w\left(15v^4+10v^2w^2+3w^4\right)\ln(b+r)+wbr\left(18v^2+7w^2+7b^2\right)\Big] \qquad (A.49)
\end{aligned}
$$

The most straightforward singular integral evaluates the reciprocal of

$$R=\sqrt{(x-x')^2+(y_c-y')^2+\left(z_c-z_c'\right)^2}, \qquad (A.50)$$

over two rectangles and originates from the contribution of the scalar potential to the MoM system matrix:

$$I_0=\int_{x_0}^{x_1}\int_{z_0}^{z_1}\int_{x_0'}^{x_1'}\int_{y_0'}^{y_1'}\frac{1}{R}\,\mathrm{d}y'\,\mathrm{d}x'\,\mathrm{d}z\,\mathrm{d}x. \qquad (A.51)$$

Performing the substitutions $p=(x-x')$ and $q=(y-y')$ and $a=z-z_c$, the double inner integral is transformed into (A.43), thus leading to

$$I_0=\sum_{k,l=0}^{1}(-1)^{k+l}\int_{x_0}^{x_1}\int_{z_0}^{z_1}\alpha\left((x-x_k'),(y-y_l'),z-z_c'\right)\mathrm{d}y\,\mathrm{d}x. \qquad (A.52)$$

The second set of substitutions $v=\left(x-x_k'\right)$, $w=\left(z-z_c'\right)$ and $b=y_c-y_l'$ shows that the last pair of integral can be written as (A.45), yielding the following expression

$$I_0=\sum_{i,j,k,l=0}^{1}(-1)^{i+j+k+l}a\left(X_{ik},Y_l,Z_j\right), \qquad (A.53)$$

with the shorthand notations $X_{ik}=x_i-x_k'$, $Y_l=y_c-y_l'$ and $Z_j=z_j-z_c'$.

The only rooftop combination possible on both patches of which the inner product does not vanish, are the ones oriented along their common coordinate, viz., x in

this example. The denominator is thus, once again, $(x-x_a)\left(x'-x'_a\right)$, with the x_a and x'_a constants equal to either of the boundary values of x/x' on their respective rectangle, originating from the definition of the rooftops in question. The integral we wish to compute is

$$I_x = \int_{x_0}^{x_1}\int_{z_0}^{z_1}\int_{x'_0}^{x'_1}\int_{y'_0}^{y'_1} \frac{(x-x_a)\left(x'-x'_a\right)}{R}\,\mathrm{d}y'\,\mathrm{d}x'\,\mathrm{d}z\,\mathrm{d}x. \tag{A.54}$$

Employing the familiar substitutions, we can reformulate this, through (A.43)–(A.44), as

$$I_x = \int_{x_0}^{x_1}\int_{z_0}^{z_1}\int_{x-x'_0}^{x-x'_1}\int_{y-y'_0}^{y-y'_1} \frac{(x-x_a)\left(x-x'_a\right)-q\,(x-x_a)}{R}\,\mathrm{d}q\,\mathrm{d}p\,\mathrm{d}z\,\mathrm{d}x. \tag{A.55}$$

$$= \sum_{k,l=0}^{1}(-1)^{k+l}\int_{x_0}^{x_1}\int_{z_0}^{z_1} \begin{array}{l}(x-x_a)\left(x-x'_a\right)\alpha\left((x-x'_k),(y-y'_l),(z-z'_c)\right).\\ -(x-x_a)\,\beta\left((x-x'_k),(y-y'_l),(z-z'_c)\right)\end{array}\mathrm{d}z\,\mathrm{d}x \tag{A.56}$$

The last two integrals are transformed by means of the second set of substitutions and through (A.45)–(A.49) this yields

$$\begin{aligned} I_x = \sum_{i,j,k,l=0}^{1}(-1)^{i+j+k+l}\Big[&\left(x'_l-x_a\right)\left(x'_l-x'_a\right)a\left(X_{ik},Y_l,Z_j\right)\\ &+\left(2x'_l-x_a-x'_a\right)b\left(X_{ik},Y_l,Z_j\right)+c\left(X_{ik},Y_l,Z_j\right)\\ &-\left(x'_l-x_a\right)d\left(X_{ik},Y_l,Z_j\right)-e\left(X_{ik},Y_l,Z_j\right)\Big]. \end{aligned} \tag{A.57}$$

B

Far Field Expressions

B.1 Introduction

An important characteristic of an electromagnetic structure is its far field behavior. This can be described by the *far field vector*, typically denoted as $\mathbf{F}(\phi,\theta)$ and/or the (monostatic/bistatic) radar cross-sections. In this appendix, the expression for the electric field at large distances is derived as well as formulas for the radar cross-sections.

B.2 Scattered electric field

In Section 2.2.1, more specifically (2.41), the scattered field is expressed as a function of $\mathbf{j}_s$. A more general formulation (i.e., also valid in a non-BIE context), which does not assume the currents to be confined to a surface, is given by

$$\mathbf{e}_{\text{sc}} = -j\omega\mu \int_{\mathcal{V}} G(|\mathbf{r}-\mathbf{r}'|)\mathbf{j}(\mathbf{r}')\,\mathrm{d}\mathbf{r}' + \frac{1}{j\omega\epsilon}\nabla \int_{\mathcal{V}} G(|\mathbf{r}-\mathbf{r}'|)\nabla'\cdot\mathbf{j}(\mathbf{r}')\,\mathrm{d}\mathbf{r}'. \tag{B.1}$$

When sources actually do exist only on the surface, this expression just reduces to (2.41).

The second integral in (B.1) can be transformed to a more convenient form using

the appropriate vector identities and Gauss' theorems:

$$\begin{aligned}\int_{\mathcal{V}} G(|\mathbf{r}-\mathbf{r}'|)\nabla'\cdot\mathbf{j}(\mathbf{r}')\,\mathrm{d}\mathbf{r}' &= \int_{\mathcal{V}} \nabla'\cdot\Big(G(|\mathbf{r}-\mathbf{r}'|)\,\mathbf{j}(\mathbf{r}')\Big)\,\mathrm{d}\mathbf{r}' - \int_{\mathcal{V}} \nabla' G(|\mathbf{r}-\mathbf{r}'|)\cdot\mathbf{j}(\mathbf{r}')\,\mathrm{d}\mathbf{r}' \\ &= \int_{\mathcal{S}} G(|\mathbf{r}-\mathbf{r}'|)\,\mathbf{j}(\mathbf{r}')\cdot\hat{\mathbf{n}}\,\mathrm{d}\mathbf{r}' - \int_{\mathcal{V}} \nabla' G(|\mathbf{r}-\mathbf{r}'|)\cdot\mathbf{j}(\mathbf{r}')\,\mathrm{d}\mathbf{r}' \\ &= -\int_{\mathcal{V}} \nabla' G(|\mathbf{r}-\mathbf{r}'|)\cdot\mathbf{j}(\mathbf{r}')\,\mathrm{d}\mathbf{r}',\end{aligned}$$

where the last step exploits the fact that $\mathcal{S}$ is a spherical surface located at infinity and since this surface does not contain any sources, the first integral vanishes. Furthermore, one easily realizes that, in a homogeneous infinite space, $\nabla' G(|\mathbf{r}-\mathbf{r}'|) = -\nabla G(|\mathbf{r}-\mathbf{r}'|)$, resulting in the following version of (B.1):

$$\mathbf{e}^{sc}(\mathbf{r}) = -j\omega\mu \int_{\mathcal{V}} G(|\mathbf{r}-\mathbf{r}'|)\,\mathbf{j}(\mathbf{r}')\,\mathrm{d}\mathbf{r}' + \frac{1}{j\omega\epsilon}\nabla \int_{\mathcal{V}} \nabla G(|\mathbf{r}-\mathbf{r}'|)\cdot\mathbf{j}(\mathbf{r}')\,\mathrm{d}\mathbf{r}'. \tag{B.2}$$

This equation can be written compactly by employing the Green's tensor

$$\overline{\overline{G}}(r) = \Big(k^2\overline{\overline{I}} + \nabla\nabla\Big)\cdot G(r) = \begin{pmatrix} k^2 + \frac{\partial^2}{\partial x^2} & \frac{\partial^2}{\partial x\partial y} & \frac{\partial^2}{\partial x\partial z} \\ \frac{\partial^2}{\partial x\partial y} & k^2 + \frac{\partial^2}{\partial y^2} & \frac{\partial^2}{\partial y\partial z} \\ \frac{\partial^2}{\partial x\partial z} & \frac{\partial^2}{\partial y\partial z} & k^2 + \frac{\partial^2}{\partial z^2} \end{pmatrix} G(r), \tag{B.3}$$

resulting in the compact following form for (B.2):

$$\mathbf{e}^{sc}(\mathbf{r}) = \frac{1}{j\omega\epsilon}\int_{\mathcal{V}} \overline{\overline{G}}(|\mathbf{r}-\mathbf{r}'|)\cdot\mathbf{j}(\mathbf{r}')\,\mathrm{d}\mathbf{r}' = \frac{1}{j\omega\epsilon}\Big(k^2\overline{\overline{I}} + \nabla\nabla\Big)\cdot\int_{\mathcal{V}} G(|\mathbf{r}-\mathbf{r}'|)\,\mathbf{j}(\mathbf{r}')\,\mathrm{d}\mathbf{r}'. \tag{B.4}$$

B.3 Green's function in the far field

For large distances, the Euclidean distance can be approximated in order to ease calculations. Generally speaking, the Euclidean distance between two points is given by

$$|\mathbf{r}-\mathbf{r}'| = \sqrt{r^2 + r'^2 - 2\mathbf{r}\cdot\mathbf{r}'}, \tag{B.5}$$

with r and r' the norm of $\mathbf{r}$ and $\mathbf{r}'$, respectively. In the far field, the observation point $\mathbf{r}$ is located at such a distance from the scatterer, that for all points $\mathbf{r}'$ of the structure $r \gg r'$. Therefore, we can approximate the Euclidean distance by calculating its first order Taylor expansion around $\mathbf{r}' = 0$:

$$|\mathbf{r}-\mathbf{r}'| = r\sqrt{1 - 2\mathbf{r}'\cdot\hat{\mathbf{r}}/r + (r'/r)^2} \approx r - \mathbf{r}'\cdot\hat{\mathbf{r}}, \tag{B.6}$$

with $\hat{\mathbf{r}}$ the unit vector in the radial direction of $\mathbf{r}$. When this approximation is plugged into the free space Green's function (2.28), the zeroth order approximation of (B.6) can be used for the denominator as the amplitude is much less affected by small variations such as $\mathbf{r}' \cdot \hat{\mathbf{r}}$ than the phase term of the exponential in the numerator. Hence, the following expression for the Green's function is used in the far field:

$$G_{\text{far}}\left(|\mathbf{r}-\mathbf{r}'|\right) = \frac{e^{-jkr}}{4\pi r} e^{+jk\mathbf{r}'\cdot\hat{\mathbf{r}}}. \tag{B.7}$$

In order to simplify the complete Green's tensor, an appropriate approximation of the Green's function's gradient has to be constructed as well. Making use of $\nabla|\mathbf{r}-\mathbf{r}'| = (\mathbf{r}-\mathbf{r}')/|\mathbf{r}-\mathbf{r}'|$ and the chain rule, one gets:

$$\begin{aligned}\nabla G(|\mathbf{r}-\mathbf{r}'|) &= \frac{e^{-jk|\mathbf{r}-\mathbf{r}'|}}{4\pi|\mathbf{r}-\mathbf{r}'|}\left(-jk - \frac{1}{|\mathbf{r}-\mathbf{r}'|}\right)\nabla|\mathbf{r}-\mathbf{r}'| \\ &= \frac{e^{-jk|\mathbf{r}-\mathbf{r}'|}}{4\pi|\mathbf{r}-\mathbf{r}'|}\left(-jk - \frac{1}{|\mathbf{r}-\mathbf{r}'|}\right)\frac{\mathbf{r}-\mathbf{r}'}{|\mathbf{r}-\mathbf{r}'|}.\end{aligned} \tag{B.8}$$

In the far field, the Euclidean distance will be given by (B.6). For the denominators, this can be further simplified to r. As such, the expression can be simplified by only retaining the term(s) with the lowest power of $|\mathbf{r}-\mathbf{r}'|$ in the denominator. Furthermore, the gradient of the Euclidean distance, can be approximated by $\hat{\mathbf{r}}$ as $\mathbf{r}'/r = (r'/r)\hat{\mathbf{r}'}$ will have a negligible influence due to its small norm. In the end, we thus get

$$\nabla G_{\text{far}}\left(|\mathbf{r}-\mathbf{r}'|\right) = -jk\hat{\mathbf{r}}\frac{e^{-jkr}}{4\pi r}e^{+jk\mathbf{r}'\cdot\hat{\mathbf{r}}} = -jk\hat{\mathbf{r}}\,G_{\text{far}}(|\mathbf{r}-\mathbf{r}'|). \tag{B.9}$$

This expression indicates that the nabla operator (∇) can be replaced by $-jk\hat{\mathbf{r}}$ in the far field, as such transforming (B.3) into

$$\overline{\overline{G}}_{\text{far}}(r) = k^2\left(\overline{\overline{I}} - \hat{\mathbf{r}}\hat{\mathbf{r}}\right)\cdot G_{\text{far}}(r). \tag{B.10}$$

B.4 Radar cross-section

With the above expression for the Green's dyadic, (B.4) can be simplified to a form for the electric field in the far field region of space:

$$\mathbf{E}^{sc}_{\text{far}}(\mathbf{r}) = \frac{1}{j\omega\epsilon}\int_{\mathcal{V}} \overline{\overline{G}}_{\text{far}}(|\mathbf{r}-\mathbf{r}'|)\cdot\mathbf{j}(\mathbf{r}')\,\mathrm{d}\mathbf{r}' = j\omega\mu\left(\hat{\mathbf{r}}\hat{\mathbf{r}} - \overline{\overline{I}}\right)\cdot\int_{\mathcal{V}} G_{\text{far}}(|\mathbf{r}-\mathbf{r}'|)\mathbf{j}(\mathbf{r}')\,\mathrm{d}\mathbf{r}'. \tag{B.11}$$

From this expression the far field vector $\mathbf{F}$ can be easily derived by employing the following relationship between the electric field and the far field vector:

$$\lim_{kr\to\infty}\mathbf{E}^{sc}(\mathbf{r}) = \mathbf{F}(\phi,\theta)\frac{e^{-jkr}}{r}, \tag{B.12}$$

in order to get the final result

$$\mathbf{F}(\phi,\theta) = \frac{j\omega\mu}{4\pi}\left(\hat{\mathbf{r}}\hat{\mathbf{r}} - \bar{\bar{I}}\right)\cdot\int_{\mathcal{V}} \mathbf{j}(\mathbf{r}')e^{+jk\mathbf{r}'\cdot\hat{\mathbf{r}}}\,\mathrm{d}\mathbf{r}', \tag{B.13}$$

where the integration will typically be reduced to the boundary $\mathcal{S} = \partial\mathcal{V}$ as the current in a MoM situation is restricted to a surface (or multiple surfaces).

From the far field vector, the various radar cross-sections can be quickly derived. The radar cross-section (RCS) $\sigma^s(\hat{\boldsymbol{\imath}})$ is defined as the total scattered power divided by the total incident power, i.e.,

$$\sigma^s(\hat{\boldsymbol{\imath}}) = \frac{1}{|E_0|^2}\int_{\Omega} |\mathbf{F}(\phi,\theta)|^2\,\mathrm{d}\Omega, \tag{B.14}$$

with $\hat{\boldsymbol{\imath}}$ the propagation direction of the impinging plane wave and E_0 its polarization vector.

The bistatic radar cross-section $\sigma\left(\hat{\mathbf{r}}|\hat{\boldsymbol{\imath}}\right)$ is defined as 4π times the power scattered in an elementary solid angle in the direction $\hat{\mathbf{r}}$, divided by the incident power of the plane wave with propagation direction $\hat{\boldsymbol{\imath}}$:

$$\sigma\left(\hat{\mathbf{r}}|\hat{\boldsymbol{\imath}}\right) = 4\pi\frac{|\mathbf{F}(\phi,\theta)|^2}{|E_0|^2}. \tag{B.15}$$

C

Limits of Summable Series

C.1 Closed analytical expressions for fundamental sums

The various series in Section 5.4.2 can all be decomposed into the fundamental sums featured here. Their analytical expressions are calculated utilizing a contour integration method as outlined in the appendix of [1]:

$$\phi(x) = \sum_{k=1}^{\infty} \frac{1}{(k^2 - x^2)} = \frac{1}{2x^2}\left[1 - \pi x \cot(\pi x)\right] \tag{C.1}$$

$$\chi(x) = \sum_{k=1}^{\infty} \frac{1}{(k^2 - x^2)^2} = \frac{1}{4x^4}\left[-2 + \pi x \cot(\pi x) + (\pi x)^2 \csc^2(\pi x)\right] \tag{C.2}$$

$$\rho(x) = \sum_{k=1}^{\infty} \frac{(-1)^k}{(k^2 - x^2)} = \frac{1}{2x^2}\left[1 - \pi x \csc(\pi x)\right] \tag{C.3}$$

$$\varsigma(x) = \sum_{k=1}^{\infty} \frac{(-1)^k}{(k^2 - x^2)^2} = \frac{1}{4x^4}\left[-2 + \pi x \csc(\pi x)(1 + \pi x \cot(\pi x))\right] \tag{C.4}$$

These functions are singular for integer values of x which corresponds to the situation where the wavenumber of a mode is exactly equal to either k or k_0 (see (3.51)–(3.52)). However, for $x \to 0$ they have a finite limit:

$$\phi(0) = \frac{\pi^2}{6} \qquad \chi(0) = \frac{\pi^4}{90} \tag{C.5}$$

$$\rho(0) = -\frac{\pi^2}{12} \qquad \varsigma(0) = -\frac{7\pi^4}{720}. \tag{C.6}$$

C.2 Auxiliary functions

We define the following auxiliary functions:

$$\Omega_0(a,b) = \frac{1}{2}\sum_{k=0}^{\infty} \frac{\varepsilon_k}{(k^2-a^2)(k^2-b^2)} \tag{C.7}$$

$$\Omega_2(a,b) = \sum_{k=1}^{\infty} \frac{k^2}{(k^2-a^2)(k^2-b^2)} \tag{C.8}$$

$$\Psi_0(a,b) = \frac{1}{2}\sum_{k=0}^{\infty} \frac{(-1)^k\varepsilon_k}{(k^2-a^2)(k^2-b^2)} \tag{C.9}$$

$$\Psi_2(a,b) = \sum_{k=1}^{\infty} \frac{(-1)^k k^2}{(k^2-a^2)(k^2-b^2)}, \tag{C.10}$$

with ε_i the Neumann factor, which equals 1 for $i = 0$ and evaluates as 2 otherwise.

Employing the closed expression for the sums as defined above, these functions simplify to

$$\Omega_0(a,b) = \frac{1}{2a^2b^2} + \frac{\phi(a)-\phi(b)}{a^2-b^2} = -\frac{\pi}{2(a^2-b^2)}\left[\frac{\cot(\pi a)}{a} - \frac{\cot(\pi b)}{b}\right] \tag{C.11}$$

$$\Omega_2(a,b) = \frac{a^2\phi(a)-b^2\phi(b)}{a^2-b^2} = -\frac{\pi}{2(a^2-b^2)}\left[a\cot(\pi a) - b\cot(\pi b)\right] \tag{C.12}$$

$$\Psi_0(a,b) = \frac{1}{2a^2b^2} + \frac{\rho(a)-\rho(b)}{a^2-b^2} = -\frac{\pi}{2(a^2-b^2)}\left[\frac{\csc(\pi a)}{a} - \frac{\csc(\pi b)}{b}\right] \tag{C.13}$$

$$\Psi_2(a,b) = \frac{a^2\rho(a)-b^2\rho(b)}{a^2-b^2} = -\frac{\pi}{2(a^2-b^2)}\left[a\csc(\pi a) - b\csc(\pi b)\right] \tag{C.14}$$

These closed analytical expression are singular for $a = b$. Note that this situation theoretically implies $k = k_0$, a trivial scenario in which the material is indistinguishable from the background medium. Nevertheless, for low frequencies and low dielectric contrast, this instance can still occur due to the finite machine precision. This limiting case therefore requires different analytical expressions, as follows:

$$\Omega_0(a,a) = \frac{1}{2a^4} + \chi(a) = \frac{\pi}{4a^3}\left[\cot(\pi a) + \pi a\csc^2(\pi a)\right] \tag{C.15}$$

$$\Omega_2(a,a) = a^2\chi(a) + \phi(a) = \frac{\pi}{4a}\left[-\cot(\pi a) + \pi a\csc^2(\pi a)\right] \tag{C.16}$$

$$\Psi_0(a,a) = \frac{1}{2a^4} + \varsigma(a) = \frac{\pi}{4a^3}\csc(\pi a)\left[\pi a\cot(\pi a) + 1\right] \tag{C.17}$$

$$\Psi_2(a,a) = a^2\varsigma(a) + \rho(a) = \frac{\pi}{4a}\csc(\pi a)\left[\pi a\cot(\pi a) - 1\right] \tag{C.18}$$

References

[1] R. Collin, *Field Theory of Guided Waves*. IEEE Press, 1991.